Ordered Mesoporous Silica:

Control of Morphology and Exploration

with Single Molecules

von

Barbara Platschek

aus Fulda

Mai 2007

Erklärung

Diese Dissertation wurde im Sinne von § 13 Abs. 3 bzw. 4 der

Promotionsordnung vom 29. Januar 1998 von Herrn Prof. Dr. Thomas Bein

betreut.

Ehrenwörtliche Versicherung

Diese Dissertation wurde selbstständig, ohne unerlaubte Hilfe erarbeitet.

München, am 31.05.2007

Barbara Platschek

(Unterschrift des Autors)

Dissertation eingereicht am 31.05.2007

1. Gutachter: Prof. Dr. Thomas Bein

2. Gutachter: Prof. Dr. Christoph Bräuchle

Mündliche Prüfung am 02.07.2007

<u>Danksagung</u>

Abstract

This thesis is focused on the formation of highly ordered mesoporous structures with adjustable orientation within the ordered, vertical channels of anodic alumina membranes (AAMs) under the conditions of the 'evaporation-induced self-assembly' (EISA) method. It is shown that three of the most often used structure directing agents (CTAB, Pluronic123 and Brij56) can be employed for the synthesis of ordered silica mesophases embedded in AAM-channels. When using the ionic surfactant CTAB, the hexagonal mesostructures were solely oriented along the AAM-channels (columnar orientation). With the non-ionic surfactants the occurrence of two different orientations (circular or columnar) can be tuned via changing the surfactant concentration and the humidity in the adjacent gas phase. The existence of a previously postulated circular lamellar phase could be proven. *In situ* scattering experiments show that when ionic CTAB was used as structure directing agent, the columnar hexagonal structure was observed to form directly from the beginning. In the samples synthesized with the non-ionic surfactants, the circular hexagonal structure was found to form first and to directly transform into the columnar hexagonal, or a mixture of the columnar hexagonal and the curved lamellar phase. By correlation of the structure formation with the weight loss during the drying process of the samples it was demonstrated that the structure formation starts after the solvent evaporation. Therefore the absence of an evaporation induced solvent gradient within the AAM channels is postulated, and a homogeneous nucleation and phase formation irrespective of the height within the AAM channels is proposed. The synthesis of pure columnar mesostructures in confined space was achieved by salt addition and temperature control, even when non-ionic surfactants were used, thus leading to salt-induced phase transformations (SIPT) that have not been previously reported.

In a collaborative project, single dye molecules were used as nanoscale probes to map out the structure of mesoporous silica channel systems that are prepared as thin films *via* cooperative

self-assembly of surfactant molecules with polymerizable silicate species. The dye molecules act as beacons while they diffuse through different structural phases of the host. While measurement of ensemble diffusion provides information about the overall behaviour of the guest in a porous host, tracking of individual molecules provides insight into both the heterogeneity and the mechanistic details of molecular diffusion as well as into the structure of the host. The structure of the trajectories, the diffusivities and the orientation of single molecules are distinctive for molecules travelling in different mesophases. Transitions between the different types of surroundings can be observed for the same individual dye molecule. These experiments reveal unprecedented details of the structure of the host, its domains and the accessibility as well as the connectivity of the channel system.

Table of Contents

II. Experimental Methods

III. Results and Discussion

IV. Conclusion

V. Appendix

I. Introduction

1. Periodic Mesoporous Materials – General introduction

According to IUPAC, materials with diameters in the range of 2-50 nm are classified as mesoporous and are distinguished from macroporous or microporous materials that have larger or smaller pore diameters, respectively.[1] Amongst them, inorganic periodic mesoporous materials have attracted considerable attention as building units for designing nanoscale architectures by applying bottom-up strategies since their discovery in 1992[2]. These materials are chemically, mechanically, and thermally stable due to the inorganic framework[3] and exhibit not only high specific surface areas and but monomodal pore size distributions and regular pore arrangements. Highly ordered powder materials have been produced in basic or acidic media[2,4], and worm-like phases have been prepared under neutral conditions[5], always exhibiting uniform pore size and Bragg-peaks at small angles in the corresponding diffraction patterns.

The method for the production of periodic mesoporous material is based on the use of surfactant molecules as structure directing agents (SDAs). Surfactants (surface active agents) are molecules with hydrophobic and hydrophilic areas. Three of the most often used templates CTAB, Brij 56 and Pluronic P123 were used in this work. CTAB and Brij 56 both have a hydrocarbon chain as the hydrophobic tail. CTAB has a quarternary ammonium ion as headgroup and bromide as counterion, the hydrophilic headgroup in Brij 56 is a polyethylene oxide chain (Figure 1a, b). Non-ionic Pluronic P123 is a tri-block copolymer with two hydrophilic polyethylene oxide blocks and one hydrophobic polypropylene oxide block (Figure 1c). In solution, surfactants self-organize into micelles and eventually into liquid crystal phases, depending on stoichiometry.[6,7]

a) CTA+

b) Brij 56 (n ≈ 10)
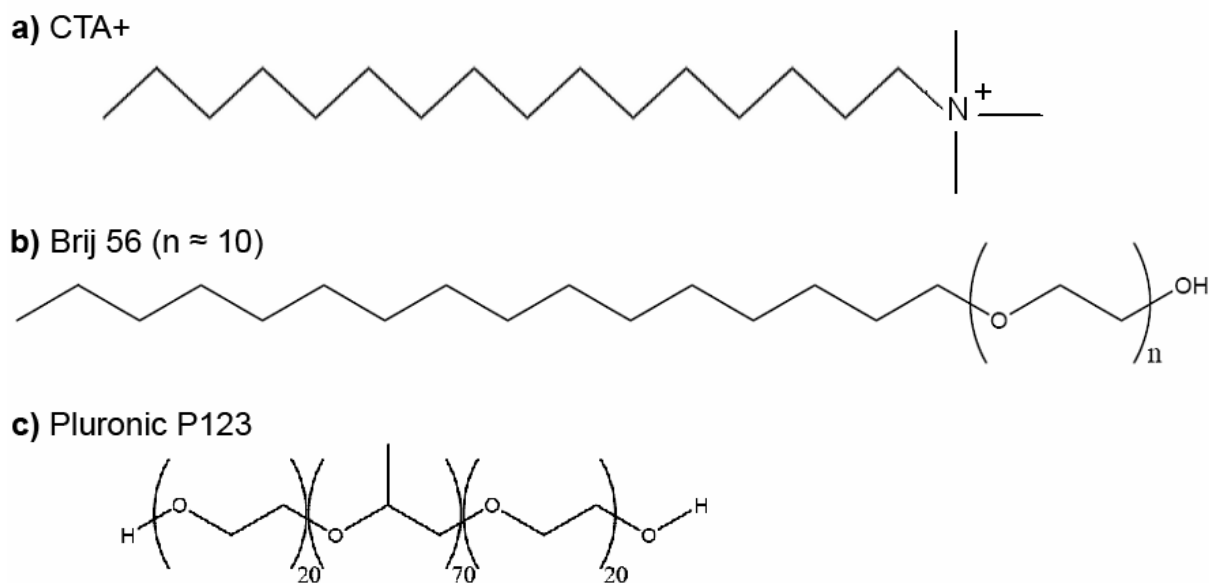
c) Pluronic P123

Figure 1: a) Cationic cetylhexyltrimethylammonium
b) Non-ionic di-block copolymer surfactant Brij 56
c) Non-ionic tri-block copolymer Pluronic P123

For the synthesis of periodic mesoporous silica, silica precursors are added to an appropriate solution of surfactant. Silica condensation enhanced by basic or acidic catalysis takes place at the surfactant/water interface and finally leads to the formation of a silica/organic composite material.[8,9] Mechanistically, two main routes have been discussed for the formation of these composite materials. On the one hand, true liquid-crystal templating is proposed for surfactant concentrations high enough to form the liquid crystal phases before the addition of inorganic precursor molecules.[10] On the other hand, cooperative self-assembly of SDA and inorganic precursor molecules is invoked when the surfactant concentration is too low to form a liquid crystal phase by itself.[11] Removal of the template by calcination, plasma treatment[12], or extraction[13,14] produces the porous inorganic material. The remarkable ability to tune structural order, pore size, and pore topology has resulted in periodic materials with different cubic[9,15-17], hexagonal[2,9] and lamellar[9] structures (Figure 2). Lamellar structures are formed from sheet-like arranged micelles. Cubic bicontinuous (Ia3d) and two-dimensional hexagonal (P6m) structures are composed of cylindrically shaped micelles. Cubic

discontinuous (Pm3n) and 3-dimensional hexagonal structured materials have been synthesized from periodically arranged spherical micelles.
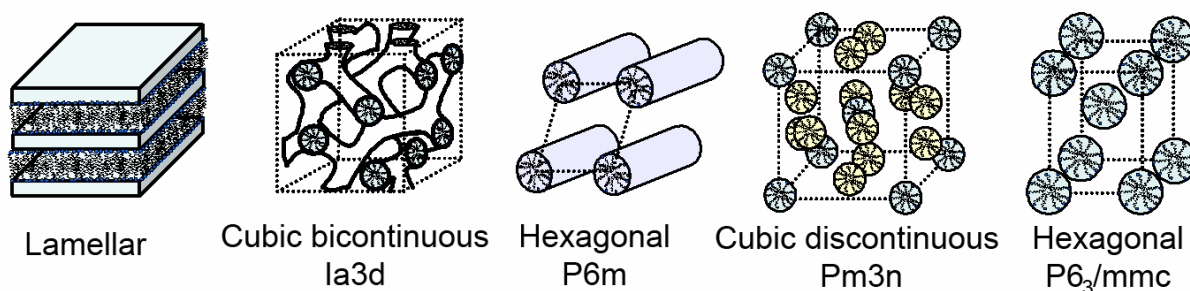
Figure 2: Schematic illustration of different lamellar, hexagonal, and cubic structures formed with sheet-like, cylindrical, or spherical micelles. Different colored micelles in the sketch of the cubic Pm3n structure are used to clarify the structure. The blue micelles are arranged in a cubic body-centered manner, two yellow micelles are positioned on each plane of the cube.

Even though silica material has been widely studied, other framework compositions could be realized as well, e.g., with the oxides of titanium, aluminum, zirconium, or tin, or multimetal oxides, respectively.[18,19] Even non-oxide materials such as metal sulfides[20], selenides[21] or phosphates[22], or pure mesoporous metal[23] were produced. Inorganic mesoporous material was used as template for the synthesis of porous carbon replica (exo-templating)[24] or nanoporous polymer-carbon composites[25]. Organically functionalized periodic mesoporous materials have been synthesized *via* post-synthesis grafting, co-condensation, or as organic-inorganic hybrid materials, based on their high potential for applications in heterogeneous catalysis.[26]

Mesopore systems have been used as optical waveguides[27], as hosts for numerous molecular and cluster-based catalysts[28], for selective sequestration of contaminants[29], chromatography[30], and for novel drug delivery systems[31,32]. Periodic mesoporous organosilica coatings were reported to have low dielectric constants, suggesting potential utility as low-*k* layers in microelectronics.[33] Living cells were immobilized in biocompatible silica mesostructures and used as a model eukaryotic sensor.[34]

Many of the envisioned applications, such as separation membranes, sensors or optoelectronic devices would benefit from growing mesoporous materials as films at surfaces or interfaces. Thin mesostructured silica films have been prepared on a variety of substrates by coating of conventional synthesis solutions,[35,36] or *via* the evaporation-induced self-assembly method (EISA[37]). The EISA approach employs homogeneous coating-solutions with volatile solvent (e.g. ethanol) and surfactant concentrations below the critical micelle concentration (see Figure 3). Silica precursors are obtained by acid-catalyzed hydrolysis of tetraethoxy-silane (TEOS). The synthesis-solutions are spin- or dip-coated or cast on various substrates. Rapid solvent evaporation drives the self-assembly process towards the critical micelle concentration and the formation of the liquid-crystal mesophase. Simultaneously, the silica-condensation is induced by increasing the concentration of acid. The dynamic, liquid crystalline character of the as-deposited films is indicated by self-healing tendencies or the possibility of phase transformations prior to solidification by, e.g., thermal treatment of the as-synthesized films.[37,38] Different phases were found to form even after completion of the EISA process depending on the humidity present; thus the presence of a modulable steady state was postulated.[39] An 'EISA adapted diagram of textures' was established for mesoporous silica films prepared with CTAB as structure directing agent.[40] In the work presented here, mesoporous silica material is produced following the EISA approach but using porous anodic alumina membranes as substrate.

Evaporation-induced self-assembly
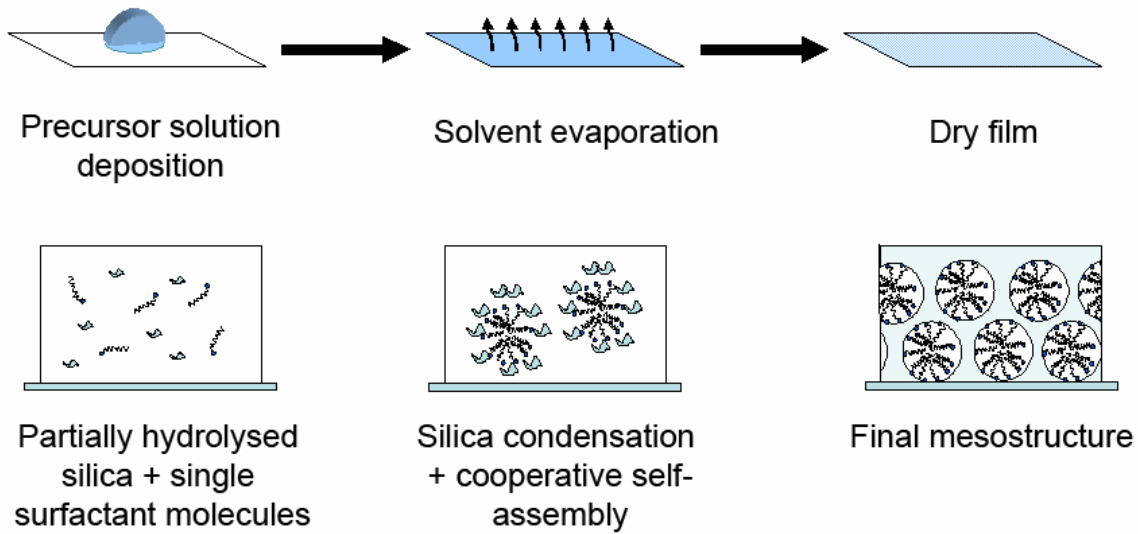
Figure 3: Scheme of the EISA process. The synthesis procedure is shown on the top, the bottom line illustrates the cooperative self-assembly and silica condensation towards the final mesophase film.

2. Anodic alumina membranes

Anodic treatment of aluminum was used since the beginning of the last century to obtain protective and decorative films on the metal surface. In general, two types of anodic films are distinguished, the dense barrier-type and the porous-type alumina. The porous anodic alumina films exhibit monomodal, vertically aligned pores with diameters between 10-500 nm. The synthesis principle for anodic alumina films is the electrochemical oxidation of the metal, while the aluminum directly acts as anode (anodization of aluminum). Various electrolytes are used for the preparation of alumina; the counter-electrode reaction is the formation of hydrogen at the cathode. Since the electronic conductivity of aluminum oxide is low, ionic current is the predominant mode for the transport of charges. Film growth takes place at the metal/oxide and the oxide/electrolyte interfaces by the transport of Al^{3+} and O^{2-} ions, respectively.

The main difference between the synthesis of barrier-type and porous-type alumina films is that dense alumina is prepared in near-neutral electrolytes while porosity occurs for synthesis

in acid electrolytes. The reason for this is that under acidic conditions the cation transport number is zero and the mobile aluminum ions are directly ejected into solution, resulting in an interplay between film growth and dissolution. Thus, the electrolyte eventually penetrates the oxide film and produces tiny cracks. The "self-healing" of the cracks in the alumina films is interrupted since there is no transport of cations. Moreover, the electric field strength is locally increased at cracks enhancing further dissolution. As a consequence pores are starting to grow and eventually organize in a quasi hexagonal manner (Figure 4).[41]

The resulting material consists of the aluminum substrate having a thin barrier layer of dense alumina followed by the thicker porous alumina film. The barrier layer between the porous alumina and the metal substrate shows no planarity but hemispherical curvatures according to the pores formed.[42] Different pretreatments of the aluminum substrate, e.g., imprinting or electron beam lithography have been successfully employed to create locations of preferred pore growth. A two-step anodization process was developed to produce self-ordered alumina structures.[43] This method describes the dissolution of the first porous alumina film leaving the pre-curved barrier film as substrate for second anodization. Controlling the self-order of the pores in the anodic alumina and obtaining large domains with highly structured material is a subject of current interest.[44]
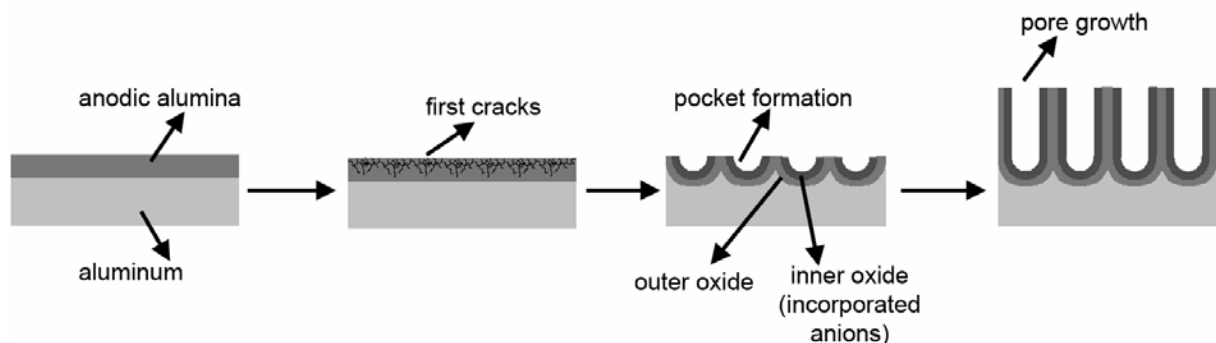
Figure 4: Schematic illustration of channel formation during synthesis of porous anodic alumina.

Anions of the electrolyte as well as OH$^-$ ions from the water are reported to be included into the alumina material during the anodization.[41,45] Thus, the pore walls consist of an inner

layer of pure aluminum oxide surrounded by anion-contaminated alumina (Figure 4).[44] Both layers were found to be amorphous.[41,46] Investigation of the formation of porous alumina on silicon substrate using multiple internal reflection infrared absorption spectroscopy revealed the correlation of alumina formation and detection of two bands at 1460 cm^{-1} and 1570 cm^{-1}, respectively.[47] These peaks were assumed to origininate from dehydrated boehmite, taking into account the incorporation of hydroxide ions into the alumina framework during synthesis. The same absorption bands were reported for commercially available AAMs[48] (as those used for this thesis). They were also observed for anodic alumina films after hydration in boiling water and were assigned to pseudoboehmite.[49] Infrared bands in that region were found for boehmite nanocrystals and calculated to correspond to ring-stretching vibrations of AlO(OH) dimers.[50]

Due to their vertically aligned channels with controllable diameters, porous anodic alumina films are of considerable interest, for example for the inclusion of nanotubes or nanowires with potential for applications in magnetic, electronic, or optoelectronic miniature devices.[51] One dimensional nanostructures consisting of metals[52], semi-conductors,[53] polymers,[54] or carbon nanotubes[55] were prepared by electrochemical deposition[52], thermal decomposition of metal salts[53,56], sol-gel deposition[57,58], polymerization reaction,[54] or chemical vapor deposition.[55] Highly ordered arrays of nanodots or nanorings can be synthesized, templated by the pores of anodic alumina membranes (Figure 5).[59, 60]
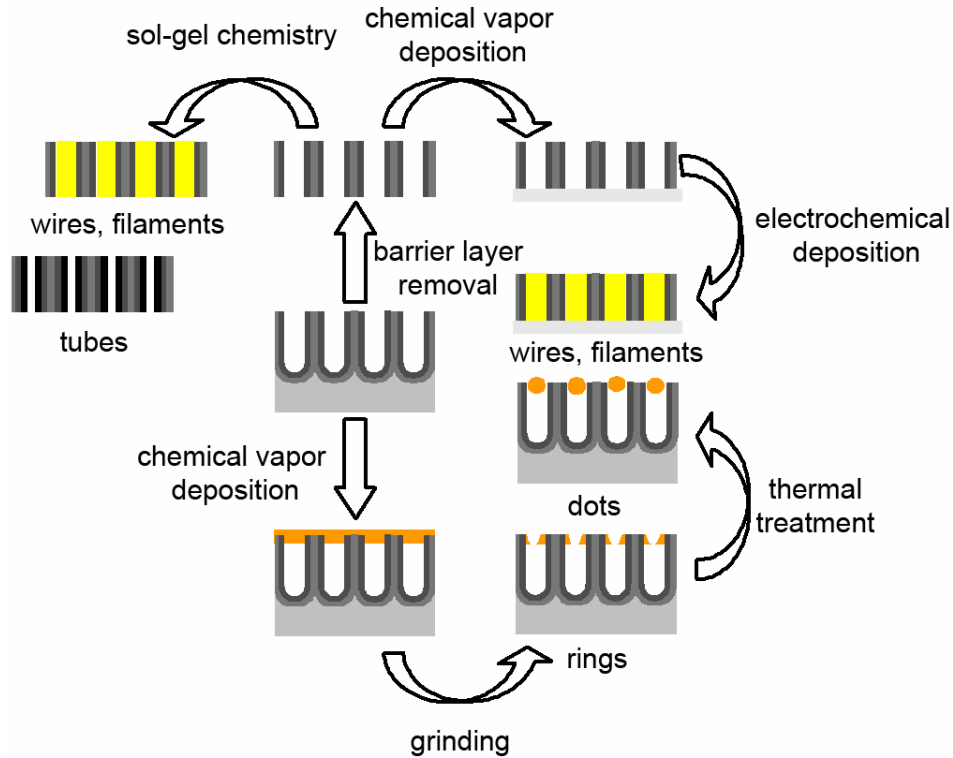
Figure 5: Some examples for porous alumina templated nanostructure synthesis. The barrier oxide layer may be removed; electrodes are deposited for electrochemical deposition of metals. Nanotubes or -filaments are synthesized with wet chemical methods. Layers are deposited via chemical vapor deposition. Subsequent grinding results in nano-ring structures that transform into nanodot-arrays when thermally treated.

Recently, high-temperature superconductor nanowires were produced inside the channels of porous anodic alumina by a sol-gel approach.[61] Nickel nanotubes with uniform tube diameters and wall thickness were prepared by a triblock copolymer-assisted hard-template method where Pluronic P123 was added to the electrolyte solution.[62] During synthesis the surfactant micelles are adsorbed on the alumina channel walls and they facilitate the formation of nickel at the alumina – micelle interface. Post-synthesis incorporation and alignment of carbon nanotubes within alumina channels using a styrene-butadiene-styrene block copolymer as carrier was reported.[63] Multisegment nanostructures which are nanowires or nanotubes consisting of segments with different material can be synthesized with various metals,[64] metal and polymer,[65] or metal and carbon nanotubes.[66] Single-walled carbon nanotubes with palladium nanowire back contacts and palladium cluster

contacts on the other end were synthesized non-lithographically and electrically addressed inside the channels of porous anodic alumina.[67]

Biocompatible lipid nanotubes with potential as hosts for the encapsulation of mesoscale guest molecules and defined inner and outer diameters were synthesized combining vesicle extrusion and loading of the synthesis suspension into alumina channels to prevent fusion of the extruded vesicles.[68] Layer-by-layer adsorption within a porous anodic alumina matrix produces nanotubes with alternating layers of Human Serum Albumin and phospholipids.[69] Tubular lipid bilayers containing the G-protein-coupled receptor rhodopsin were formed inside anodic alumina channels while the protein function and lipid bilayer properties were maintained, enabling structural studies on a membrane protein at functional conditions.[70] Crystallographically aligned hydroxyapatite nanorods were also prepared inside a porous alumina membrane, thus mimicking the texture of natural bone where oriented hydroxyapatite rods are embedded in a collagen matrix.[71] Porous alumina films were found to induce oriented crystal growth in several other cases. For example, layered double hydroxides or boehmite sheets grown onto porous alumina substrates were fully oriented with their c-axis parallel to the membrane surface resulting in super-hydrophobicity.[72,73] Aluminophosphate molecular sieves were observed to align with their c-axis vertical to a porous anodic alumina support.[74,75]

Free-standing porous anodic alumina membranes are used as bio-filters[76] or as column for high performance liquid chromatography.[77] Phenol and toluene had different retention times depending on the column length (number of membranes used) and the composition of the mobile phase (ethanol and heptane) even in unmodified anodic alumina membranes, due to interactions with their surface OH-groups. A composite membrane of porous anodic alumina filled with magnesium hydroxide nanotubes was reported to be efficient for removing nickel

ions from wastewater by simple filtration.[78] The nickel containing membranes were heated to obtain the magnesium oxide – aluminum oxide – nickel oxide composite and showed continuously good performance for the adsorption of nickel ions from wastewater. A composite membrane for selective separation of bio-molecules was prepared by the formation of molecularly imprinted polymer nanotubes within anodic alumina channels *via* surface-initiated atom transfer radical polymerization.[79] Furthermore, development of a micro-scale catalytic combustor based on a palladium modified porous anodic alumina catalyst was reported.[80]

Porous anodic alumina exhibits interesting optical properties[81] and may be employed as 2D photonic crystal.[82] Recently, lasing from optically pumped fluorescent dye forming a thin layer on porous anodic alumina was reported.[83] The emission wavelength was tunable by varying the filling factor of the dye layer within the alumina channels. Strongly enhanced luminescence was observed for lanthanide-doped titania xerogels when confined inside porous anodic alumina.[84-86] Moreover, porous anodic alumina membranes show high potential for applications in the field of sensing, e.g., bio-molecular reactions. Ordered arrays of DNA nanopatterns with controlled intervals between the patterns have been produced by chemical binding of functionalized DNA on gold nanowires.[87] These nanowires were grown only in selected alumina channels resulting in hexagonal gold patterns with very large intervals, enabling the observation of fluorescence-dye labeled DNA selectively binding to the immobilized DNA within the resolution limit of a standard optical fluorescence microscope. Preparation of a label-free DNA biosensor was reported based on interferometric and localized surface plasmon resonance properties of gold-capped porous alumina nanostructures.[88]

Highly ordered porous films with controlled channel diameter and inter-channel distances are often needed for many of the applications mentioned above. Preparation of those membranes in most cases – especially when the use of other material besides alumina is desired – requires the use of cost- and time-intensive lithographic or masking methods.[89,90] Furthermore, synthesis of ordered anodic alumina with channel diameters of 10 nm or below is challenging. Employing periodic mesoporous materials within the channels of porous anodic alumina potentially closes that gap, thus enabling fast and efficient production of various hierarchical composite materials having regular, aligned pores with diameters in the range of about 20-2 nm and high order through self-assembly. Moreover, accessibility of oriented aluminophosphate templated by porous anodic alumina membranes provides thorough tunability of desired pore sizes down to the micropore range.[74,75]

3. Motivation and goals

This thesis is focused on controlling the structure and orientation of periodic mesoporous silica synthesized within the channels of anodic alumina membranes (AAMs), and on the investigation of diffusion and orientational dynamics of single dye molecules trapped inside the pores of mesostructured material. The work contributes to projects funded by the Deutsche Forschungsgemeinschaft exploring the potential of mesoporous host-guest systems for the development of nanoscopic electrical devices or as novel drug-delivery systems[91] The diffusion studies were done in cooperation with Johanna Kirstein and Christophe Jung from the research group of Prof. Bräuchle at LMU who performed the respective single molecule fluorescence microscopy studies.

The regularity and monomodal pore size distribution of periodic mesoporous silica make it an optimal host for the templated growth of conductive or semi-conductive nanowires separated by the isolating matrix.[92-94] The potential use of these systems in nanoscale electrical devices

requires control over the morphology and orientation of nanowires and therefore requires control over the structure and orientation of the mesoporous host material.[95-97] While mesoporous domains are randomly rotated against each other in powder material, they exhibit a preferred orientation with respect to the substrate surface when synthesized as films on flat supports. However, for most systems, on the substrate plane the domains are randomly rotated against each other (Figure 6).[98]
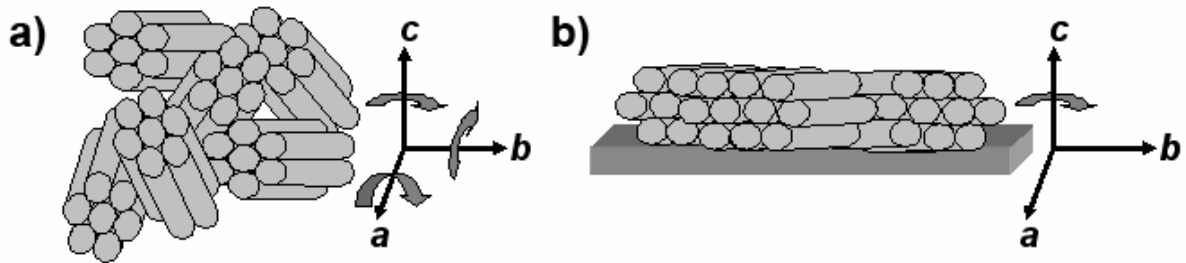
Figure 6: a) Mono-oriented domains randomly rotated against each other in three dimensions
b) Mono-oriented domains randomly rotated against each other in the a/b-plane

There have been great efforts during the last years to influence the domain size and orientation of mesoporous films.[97,99-101] Recently, the synthesis of films with vertically aligned pores that are optimal as potential templates for nanowire growth was reported.[102] In that report, films with vertical pore-alignment in the centre were described that feature parallel alignment of pores on the film-substrate and film-air interfaces. The authors focused their attention on preventing the parallel mesopore-alignment at the interfaces by substrate modification and ageing the films under controlled atmosphere for several days.

In the work presented here, a different approach was followed. Mesoporous material was synthesized within the confined environment of a strongly curved substrate, namely the nanosized channels of anodic alumina membranes. The idea is that the spatial constraints will limit the possibility of domain orientation and force the mesopores to align evenly along the

AAM-channels (Figure 7). Interestingly, different structures and orientations were found to form in such a confined environment (see below). This work is aiming at controlling these phases and preparing phase-pure systems with the desired orientation inside the channels of AAMs.
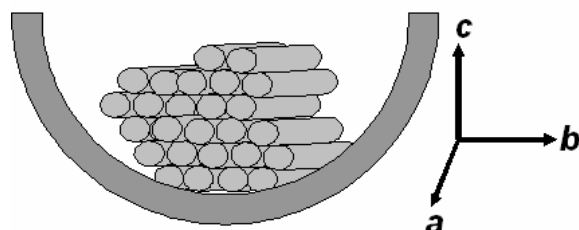
Figure 7: Alignment of pores along the a-axis due to the spatial constraints in the b/c-plane.

Mesostructures with controlled orientation are not only of interest for the synthesis of oriented nanowires but also as host system for diffusion and orientation studies on single molecules. These systems are of interest because the mesopore orientation is known on a macroscopic scale that is perpendicular to the centimeter-sized AAM surface. Observed dynamics of molecules trapped inside the pores can be directly correlated with the known orientation of the structure. Moreover, the dimension of the mesostructured material is limited to the nanometer scale in one direction, resembling mesoporous nanoparticles which are of potential interest as drug-delivery agents (Figure 8). The study of diffusion within nanoparticle systems is difficult due to the short pathways in such a sample. Thus, oriented nanoscale fibers can serve as model systems for gaining insights into diffusion dynamics within particles of confined dimensions. However, the alumina membranes are not transparent to light. The silica fibers need to be extracted from the membrane and transferred to a transparent substrate (glass) to be able to perform fluorescence microscopy. In addition, a complementary technique for following the trajectories of individual molecules is fluorescence microscopy on single dye molecules within mesostructured thin films on glass substrates.[103] Thin films directly prepared on glass are not entirely oriented but have the advantage of being transparent to light and comparatively easy to handle. This feasible approach was developed

prior to studies on mesostructured fibers from composite membranes, and it is the experimental set-up for most of the results presented in this thesis.
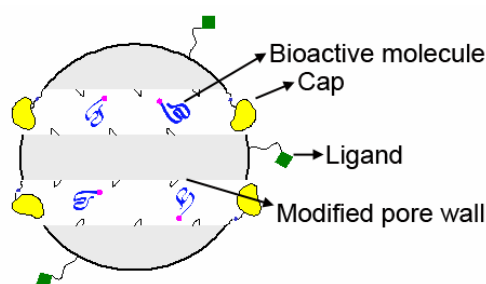
Figure 8: Model of potential drug-delivery system based on mesoporous nanoparticles. The pore wall might be modified and bioactive molecules are incorporated into the pores. The pore-openings are closed with caps that are removed at the desired location to achieve controlled release of the molecules. The particle surface may be modified with ligands for selective binding.

Molecular movement in confined spaces is important in many areas of technology and the life sciences, with examples ranging from the molecular sieving action of microporous catalysts and membrane separations to active transport through ion channels. The ensemble diffusion behavior of small molecules within mesopore structures has been examined with pulsed field gradient NMR spectroscopy[104] and neutron scattering[105]. Fluorescence correlation spectroscopy has been applied widely to study the diffusion of dye molecules in liquids[106], porous media[107] and biological systems[108]. While the method was recently applied to diffusion in ordered mesoporous hosts[109], it is an indirect technique because it requires a plausible model of the diffusion processes underlying signal fluctuations in order to extract the molecular diffusion coefficient. Individual trajectories cannot be obtained by this technique and heterogeneities may be hard to extract. On the other hand, higher temporal resolution can be achieved than with wide-field microscopy and single particle tracking (SPT). SPT has been used to observe random movement of single dye molecules in many systems, ranging from defects in crystalline hosts[110], catalytic conversions[111], sol-gel glasses[112,113], to surface receptors in nerve synapses[114] and even tagged single viral particles[115]. While measurement of ensemble diffusion provides information about the overall behavior of the guest in a porous host, tracking of individual molecules provides

insight into both the heterogeneity and the mechanistic details of molecular diffusion as well as into the structure of the host. Correlation of the molecular dynamics with structural features such as different phases, domain size, and connectivity at domain-domain interfaces is an important aim of these studies.

4. Synthesis of mesostructured material within the channels of AAMs – Literature review

Recently, the synthesis of mesoporous materials within the regular, larger channels of anodic alumina membranes (AAMs) has been explored, aimed at attaining greater control over the morphology of the mesoporous system.[116] In general, two different synthesis routes are followed to fill the AAM matrix. The first approach is based on the sol-gel synthesis of mesostructured powders and involves the immersion of the porous membranes within a synthesis solution throughout the gelation process.[117-121] Typical solutions for such process contain relatively low amounts of solvent and high surfactant concentrations. The gelation process is often induced by hydrothermal treatment and takes from several hours up to days. The second approach follows the EISA process[36] conventionally used in thin film synthesis. It involves soaking the alumina substrate with small amounts of precursor solutions and subsequent solvent evaporation-induced gelation and structure formation.[122-126] Synthesis solutions used for this approach contain comparatively high amounts of volatile solvent and low surfactant concentrations. This is done in order to obtain cooperative micelle formation and self-assembly of the condensing silica species. The rate of the synthesis in this case is limited by the rate of solvent evaporation, which usually takes a few minutes. An overview of the different approaches reported in the literature for the synthesis of mesostructured material inside AAM-channels is given in Table 1. A summary of the mesophases observed according to the different syntheses and the morphology of the mesostructured material is given in Table 2.

Table 1: Summary of reported procedures for synthesis of mesophases within AAM channels.

Literature	TEOS /mol[a]	Surfactant /mmol	Acid /mmol	Ethanol /g	Method
117	0.01	F127, 0.05	HNO_3 0.1	1.5	• Sol-gel: 12 h immersion (RT[b]), 2h air (RT[b]), 1h 60 °C • Modification of AAM
122	0.01	P123, 0.096	HCl 0.01	4.05	• EISA (dip-coating) • Small AAM-channels
123	0.01	CTAB, 0.75	0.04 HCl	2.7	EISA (casting)
118	0.01	P123, 0.17	0.2 HCl	5.0	• Sol-gel: immersion (20 h at RT[b], 20 h at 60 °C)
120	0.01	P123, 0.17	0.2 HCl	5.0	• Sol-gel: immersion (25 minutes 40 °C, 12 h at 60 °C under various conditions)
121	0.01	P123, 0.17	0.2 HCl	5.0	• Sol-gel: immersion (25 minutes 40 °C, 12 h at 60 °C under various conditions)
119	0.01	P123, 0.12 – 0.23	0.09 HCl	1.7	• Sol-gel: 2-4 h immersion (RT[b]), 12 h ageing at RT[b]
124	0.01	CTACl, P123, F127 No detailed recipe given			EISA (sequential casting)
126	0.01	Brij 56, 1.35	0.035 HCl	4	EISA (dip-coating)
125	0.01	F127, 0.06	0.65 HCl	4.9	EISA (sequential casting), composites of porous silica/titania or silica/zirconia material

[a] all amounts were re-calculated corresponding to 0.01 mol silica precursor for comparison
[b] room temperature (RT)

Table 2: Overview of reported mesophases for synthesis procedures summarized in Table 1.

Literature	Structure, Morphology
117	• Circular hexagonal • Tubes in unmodified, rods in modified AAMs
122	• Circular phases[a] • Rods
123	• Disordered columnar hexagonal • Rods
118	• Columnar hexagonal • Rods
120	• Circular hexagonal or columnar hexagonal depending on water vapor present during ageing • Tubes (aged outside AAMs), Rods (aged inside AAMs)
121	• Circular hexagonal or Mixture of columnar hexagonal and lamellar phase depending on water vapor present during ageing • Rods (aged inside AAMs)
119	• Mixture of circular hexagonal and columnar hexagonal phase, with increasing surfactant content formation of lamellar phase • Rods
124	• Circular hexagonal phase with P123 and CTAC, cubic phase with F127 (not further calssified) • Rods
126	• Mixture of circular hexagonal and cubic Ia3d phases (according to powder XRD) • Rods
127	• Cubic Im3m structure with F127 acoording to powder XRD (higher order in silica material acoording to TEM) • Rods
[a] Due to synthesis in very small AAM-channels, unusual circular phases were observed, leading to the formation of chains from spherical micelles at channels with diameters smaller than 30 nm.	

4.1. Sol-gel processes

In a first approach using a sol-gel method the tri-block copolymer Pluronic F-127 ($PEO_{100}PPO_{65}PEO_{100}$) was used as structure directing agent.[117] The anodic alumina membranes were used either as-purchased or after hydrophobization of the alumina surface with octyltrichlorosilane. They were immersed in a surfactant and TEOS-containing synthesis sol for 12 hours. After complete infiltration, the AAMs were taken out, the residual sol was

scratched away from the membrane surface and the silica condensation was performed by exposing the composite membranes to air for 2 hours, followed by ageing at 60 °C for one hour and template removal at 450 °C for 3 hours. In unmodified AAMs, the silica material was observed to form nanotubes, while nanofibers were formed when hydrophobized membranes were used as substrate. The tubes or fibers were found to have a 2D-hexagonal mesostructure with circular orientation. Similar (free standing) unusual mesophase structures are known from CTAB-templated fibers prepared by solvothermal methods and were named "circulites" or circular crystals.[127,128] Silica-titania core-shell nanofibers were produced by immersing the silica nanotube-containing alumina membrane in tetrabutyltitanate for 12 hours and then inducing the sol-gel process by ageing in moist atmosphere for 48 hours (Figure 9).
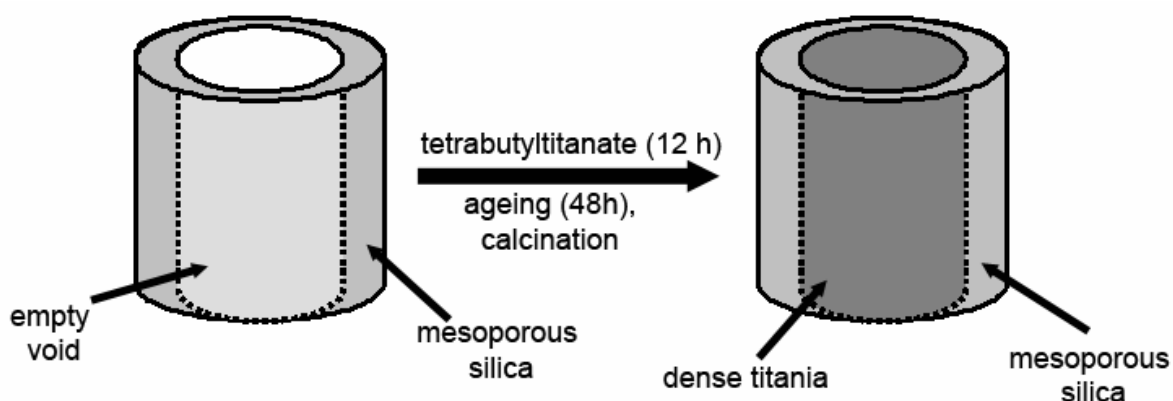
Figure 9: Preparation of silica-titania core-shell material

When the surfactant concentration was increased, a mixture of circularly oriented mesopores and mesopores that were aligned along the long axes of the AAM-channels (columnar orientation) was observed in TEM images. A pure columnar orientation of mesoporous silica nanofibers was reported using Pluronic P123 ($PEO_{20}PPO_{70}PEO_{20}$) as template and a sol-gel approach.[118] The porous alumina membrane was placed inside the synthesis sol for 20 hours followed by additional ageing within the sol at 60 °C for 20 hours. Contrary, silica fibers comprising a phase mixture of circular and columnar orientations were produced with the same recipe but different immersion time of the AAM in the synthesis sol (2-4 hours) and

ageing outside the sol for 12 hours at ambient condition.[119] Palladium replicas of the circular silica mesostructure were obtained, leading to the discussion of a helical extension of the pore system instead of the formation of a closed donut-shaped circular phase. A concentric, tubular lamellar phase was postulated to form at higher surfactant concentrations. This phase is difficult to be confirmed since only TEM images were presented, viewing the structure from the side and exposing the same stripe-pattern as the columnar hexagonal orientation. An overview over the structures and orientations discussed within the channels of porous alumina membranes is given in Figure 10.
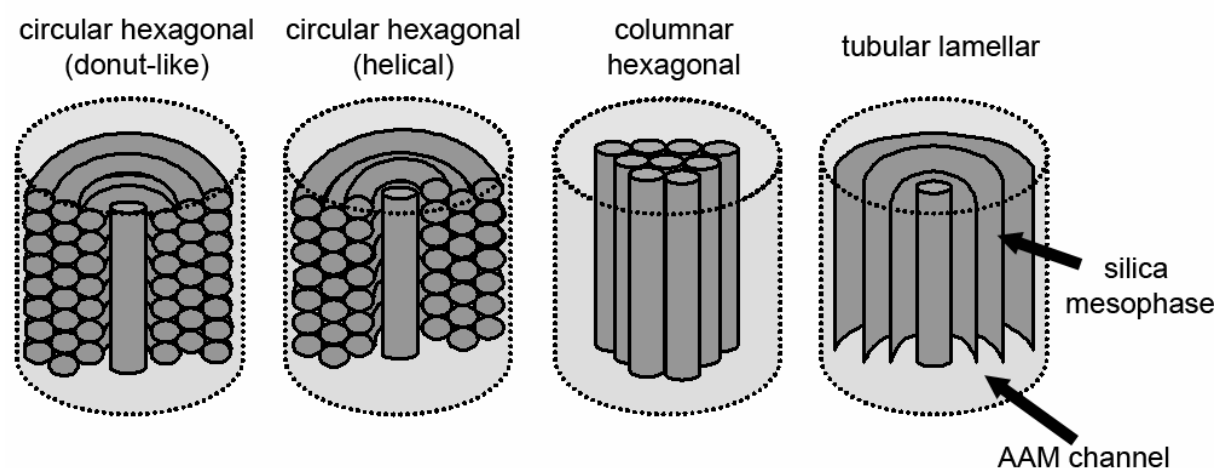
Figure 10: Overview over observed mesostructures within AAM channels. The hexagonal phase is observed with two different orientations, either circular (helical or donut-like) or columnar.

In a more systematic investigation of the synthesis conditions on the final silica mesostructure, AAMs were immersed within a synthesis sol containing Pluronic P123 at the same surfactant **:** silica ratio as in the studies discussed above.[120] After 30 minutes immersion time, one membrane was removed from the sol and aged at 60 °C for 12 hours. A second and third membrane were kept in the sol and aged at 60 °C for 12 hours with and without the presence of water vapor, respectively. While formation of silica nanotubes was observed for the sample aged outside the sol, dense silica fibers were formed when the membrane was kept within the sol throughout the synthesis. It was suggested that during ageing within the sol material is constantly incorporated into the alumina channels, while

ageing outside the sol limits the amount of included material. During gelation the volume of the sol is decreasing and the material is deposited only at the channel walls forming tubular arrays of mesostructured silica. Ageing within the sol in the presence of water vapor resulted in silica rods with circular hexagonal arrangement of mesopores, while ageing without water vapor lead to the formation of silica rods with columnar hexagonal mesostructure. In a later publication, the silica fibers were reported to consist of a tubular lamellar structure surrounding a columnar hexagonal phase.[121] It was suggested that the water vapor influences the speed of silica-hydrolysis and therefore has impact on the formed structure.

4.2. Synthesis *via* EISA

One can also take advantage of the efficient EISA method for the preparation of AAM-mesoporous composite materials, by applying coating solutions typically used for the deposition of mesoporous silica films. In one of the first studies, various porous alumina membranes with distinct channel diameters from 18 nm to 80 nm were employed as substrates and dip-coated with a synthesis solution containing Pluronic123 which was used as structure directing agent.[122] The composite membranes were aged at 25 °C and 65-70 % relative humidity for 24 hours and then calcined at 500 °C. Different mesostructures were found depending on the confinement conditions imposed by the different diameters of the alumina nanochannels, ranging from single chains of spherical mesopores to concentric or helical mesopores. The observed structures were simulated by self-consistent field theory. Although the formation of mesostructures inside membranes with different channel diameters is an interesting subject, to date not many studies have addressed this subject. This is probably due to the limited availability of different channel diameters; commercially available membranes are limited at around 200 nm channel diameter and the synthesis of porous alumina membranes having small channel diameters and highly ordered patterns requires precise control of processing parameters.[43,44,122] Silver replicas of the above structures were obtained

by electrochemically filling the mesopores of the calcined samples. Surprisingly, even replicas from concentric circular mesopores (donut-like) were obtained by this method. These stacked circular structures were reported to break into individual rings upon sonication. Thus, a loose connection between the mesopores through a micropore system similar as observed in bulk SBA-15 was discussed.

Similar behavior was observed when oriented carbon replicas were obtained in hexagonal silica fibers having circular and columnar mixed orientations; the silica fibers were synthesized within a commercially available porous alumina support with 200 nm channel diameters using Pluronic P123 as template and the EISA method.[129] The carbon nanostructures were obtained *via* supercritical fluid deposition into iron-containing mesoporous silica of a xylene precursor dissolved in carbon dioxide. The catalytic iron centers were introduced by adding ferric nitrate to the EISA precursor synthesis solution followed by calcination and reduction with H_2. The successful inclusion of metal and semiconductor nanowires into silica mesophases synthesized within AAM channels by a wet chemical impregnation approach was reported in another publication.[130] Besides impregnation of metal precursors into calcined samples followed by reduction in H_2, treatment of the uncalcined mesophases with a metal precursor-containing ethanol/water solution was described, resulting in simultaneous extraction of the template, and one-step deposition and reduction of the metal precursor within the silica mesopores during impregnation.

Cationic CTAB was also used as a surfactant template for the synthesis of mesostructured silica – alumina composite membranes.[123] A typical EISA solution was dropped onto a commercially available AAM and sucked into the alumina channels by careful aspiration, followed by drying under ambient conditions. The resulting silica material showed some level

of columnar mesopore alignment in the vicinity of the alumina walls while little order was observed in the remaining volume of the silica fibers.

It was suggested that adsorption of CTAB at the alumina induces the growth of mesostructured material at the channel walls leading to decreased concentration of surfactant and silica deeper inside the alumina channels. Thus, the nanocomposite is supposed to form only near the front surface of the membrane. This is contrary to the observations discussed above that the mesostructured material tends to shrink in radial direction rather than along the alumina channels (Figure 11). Adsorption-desorption isotherms of the composite membranes were obtained after calcination at 400 °C showing type-IV isotherms typical for mesoporous materials. The composite membranes showed promising behavior as molecular separator, even when uncalcined. Comparatively small molecules such as rhodamine B and vitamin B 12 could pass through the mesopores, while larger molecules such as myoglobin or bovine serum albumin could not.

4.3. Pore filling

For further applications as molecular separators it is desirable to produce composite membranes in which the mesoporous material completely fills the AAM channels. Especially in calcined samples, shrinkage of the mesostructure is often observed, thus leaving a gap between silica fibers and the alumina channel walls. Sequential loading techniques were employed to overcome this problem, resulting not only in multiple mesoporous silica phases[124] but also in composites of heterogeneous mesoporous oxides[125] (Figure 11). In a first approach, ionic CTAC and Pluronic P123 were used as structure directing agents to obtain mesostructured composite membranes via the EISA approach. These materials were calcined leaving mesophases which only partially fill the AAM channels but mimic their respective shape. This behavior was attributed to completely filled channels at an early stage

of the synthesis followed by shrinkage of the structure most probably during template removal. The composite membranes were used as substrates in a second synthesis where Pluronic F127 as surfactant leads to cubic mesostructures. Complete filling of the AAM channels with the hexagonal – cubic composite material was observed in TEM images. In a second approach, Pluronic F127 was used as template but mesostructured titania or zirconia was synthesized and calcined during the first step. In a second step the voids between mesoporous oxide and the alumina channel walls were filled with mesostructured silica and calcined again. Complete filling of the AAM channels was probed by air permeability measurements. The measured values were reported to be in good agreement with literature values for permeation through mesoporous silica powder having 3 nm pore size.
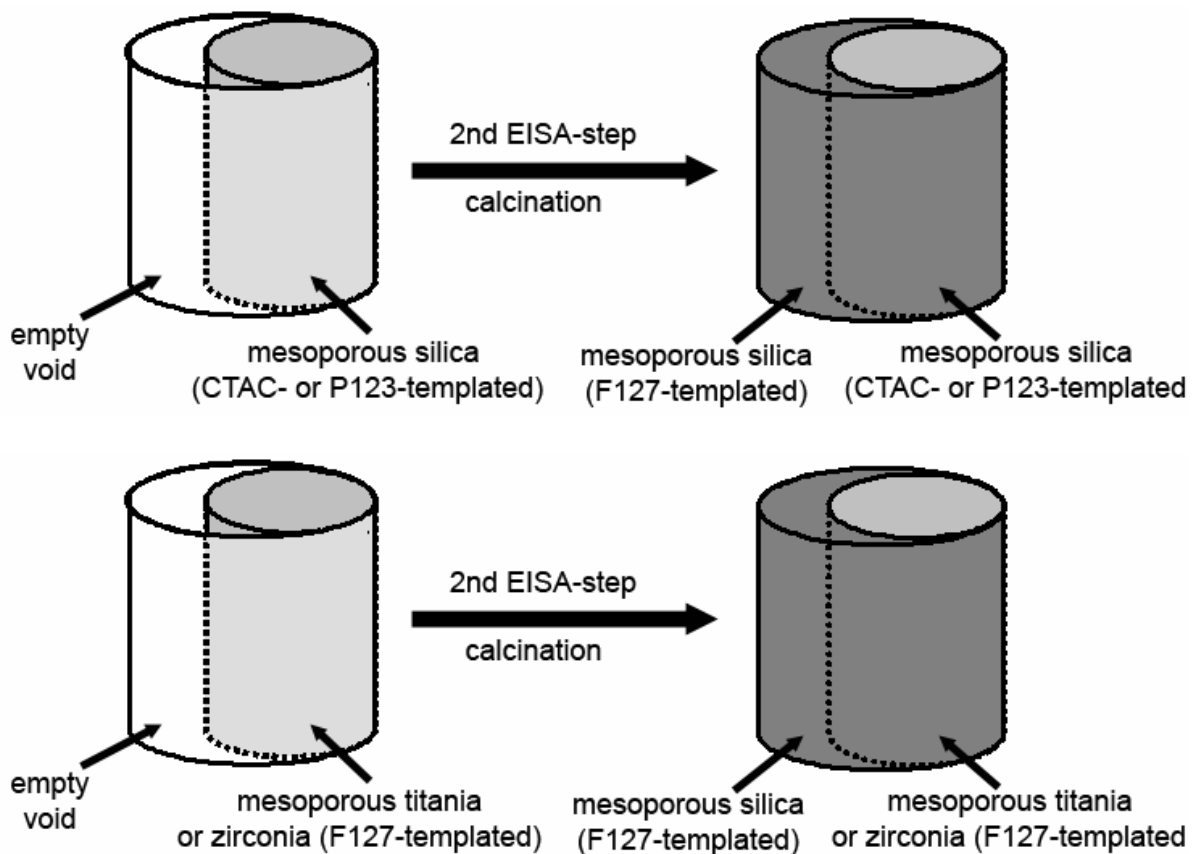
Figure 11: Preparation of multiple silica mesophases or heterogeneous mesoporous oxide composites via sequential EISA processing.

4.4. Applications

In a detailed permeation study, chromatographic experiments were carried out using a non-calcined CTAB-templated composite membrane as column.[131] A mixture of toluene and phenol was separated in a chromatography experiment, where the composite membrane was used as column and the mobile phase was n-hexane at a constant flow rate of 0.2 mL/minute (Figure 12). The retention time of phenol was found to be larger than that of toluene, which was attributed to stronger interactions of phenol with the silica-surfactant composite due to dipole interactions with the ionic interface at the silica pore wall.
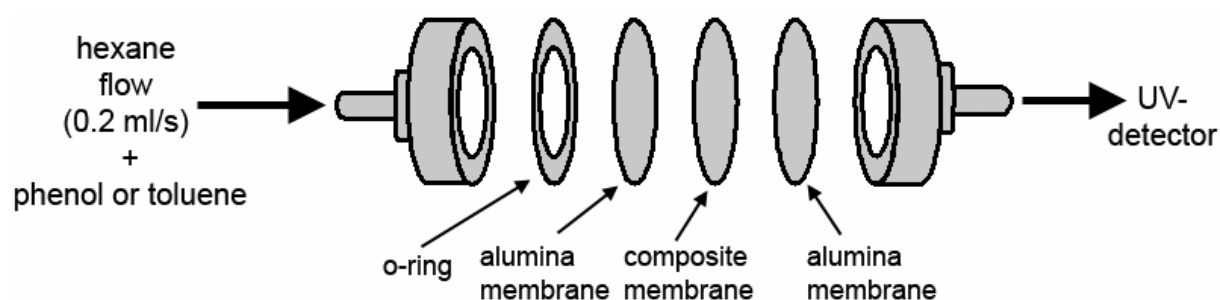
Figure 12: Scheme of the chromatography experiment (after [132]). Two porous alumina membranes were used to stabilize the composite membrane. The composite membrane was used template-containing.

Additional permeation flux measurements were done using a U-tube, the feed half-cell containing the solute (phenol, benzene sulfonate, or benzene disulfonate) in water or an ethanol-water mixture, the permeation half-cell containing only solvent. Transport through the membrane was measured by monitoring the UV absorption as a function of time in the permeation half-cell. If water was used as solvent, the transport through the membrane was fast for phenol and less pronounced for the sulfonate-molecules in agreement with the molecular charge. If an ethanol-water mixture is used as solvent and the ethanol content is successively increased, the permeation of phenol is decreasing while the permeation of the charged sulfonates is increased. Incorporation of solute molecules into the composite membrane was investigated by immersing the membrane in an aqueous feed solution and

following the decreasing light absorbance of the solution with time. Respective elution experiments were carried out with the same method. While phenol was not captured by the membrane, both sulfonates were incorporated into the pores of the silica-surfactant composite. It is concluded that the charged aromatic molecules are adsorbed within the composite membrane, thus showing less pronounced transport through the membrane, while phenol shows high permeation flux. Nevertheless, phenol interacts more strongly with the silica-surfactant composite than toluene showing larger retention time in a high pressure liquid chromatography experiment. Moreover, the interactions with the composite membrane are strongly influenced by the choice of solvent.

A mechanism for the incorporation of charged dye molecules into non-calcined CTAB-templated composite membranes was proposed in another publication by the same authors (Figure 13).[132] The dyes were extracted from aqueous solutions containing various types and concentrations of inorganic salts. The extraction of cationic rhodamine G6 was facilitated by inorganic salt addition. The strongest effect was observed for sodium perchlorate followed by sodium nitrate and bromide, the smallest effect was observed for sodium chloride, which is consistent with the Hofmeisters series of salts.[133] The Hofmeisters series of salts reflects the dehydration energy of anions, chloride having the highest energy and perchlorate having the lowest. Thus, the authors propose an ion-pair extraction process for the cationic dye molecule, involving counter ion matching and incorporation into the hydrophobic part of the micelles. In contrast, the effect of dye incorporation into the membrane is inhibited by the addition of inorganic salt for anionic sulforhodamine B according to the Hofmeisters series. The authors conclude that the anionic dye molecule is extracted from aqueous solution via a different mechanism by replacing the bromide counter ion of CTAB at the silica-surfactant interface. In a related study, the local environment of neutral and anionic coumarin dyes incorporated in

non-calcined CTAB-templated composite membranes was investigated by time-resolved fluorescence spectroscopy.[134]
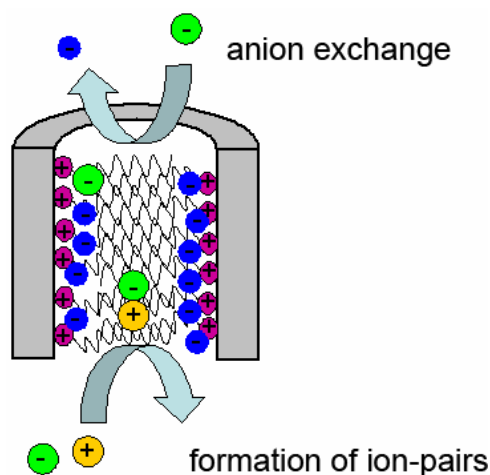
Figure 13: Illustration of the proposed mechanism (after [133]) for incorporation of dye molecules into a silica mesophase containing cationic template. One possibility is the incorporation into hydrophobic areas after ion-pair matching. Another possibility is exchange with the template counter ions.

Furthermore, permeation measurements of tris(2,2'-bipyridyl)ruthenium through a composite membrane after the one-step extraction of the ionic surfactant and simultaneous modification of the silica with alkylsilanes[135] were carried out.[136] The transport of the ruthenium complex through the membrane was recorded by time-dependent absorption spectroscopy of a feed and a permeate solution. Diffusion coefficients estimated from observed lag-times were compared for silanes with different alkyl chain lengths and for various solvents. The lag-time is the time before the transport of the ruthenium complex into the permeate solution shows linear behavior. Diffusion coefficients for silanes having short alkyl chains (methyl- and butyl-groups) were several orders of magnitude smaller than in the respective bulk solutions, when ethanol was used as solvent. Diffusion in mesopores that were modified with long alkyl chains (dedecyl-groups) was about two orders of magnitude smaller as in bulk ethanol solution. This behavior is attributed to stronger hydrogen-bonding interactions between the solvent molecules in the cavity of the mesopores slowing down the molecular diffusion. If the

alkyl chains are very long, the authors assume that less solvent molecules are present in the mesopore channels and diffusion can again be faster.

Gas permeation measurements were performed on composite membranes composed of anodic alumina and Brij 56-templated mesoporous silica prepared by dip-coating of an EISA precursor solution.[126] The synthesis procedure was previously reported for thin film preparation, resulting in a bicontinuous cubic phase. However, silica fibers with circular hexagonal and cubic structures were observed in transmission electron microscopy. Powder X-ray diffraction patterns were obtained from as-synthesized membranes showing peaks that were attributed to a surface layer formed on the planar membrane surface and assigned to a mixture of lamellar and Ia3d cubic phases. After ethanol extraction of the surfactant, no peaks were observed in powder diffraction anymore, but some of the circular hexagonal and cubic mesoporous material was still observed by TEM imaging. The gas permeation measurements were performed with the extracted composite material. The transport of nitrogen, helium, and propane through the membranes was investigated and compared with the permeation properties of commercially available separation membranes having 200 nm, 20 nm, 10 nm, and 5 nm nominal pore size. Those membranes are generally composed of a large pore alumina support and a thin layer of material exhibiting the smaller pore sizes.

The permeance and permselectivity of the membranes were compared; the permselectivity being represented by the ratio of helium to nitrogen permeance or propane to nitrogen permeance, respectively. It was found that the effective pore size of the composite membranes depends on the number of dip-coating cycles, after four cycles reaching consistency with the expected pore size for the Brij 56-templated mesoporous material according to TEM and powder X-ray diffraction experiments. The permselectivity for a four-time dip-coated membrane was much higher as for commercially available membranes with 5 nm pore size,

according to the narrow pore size distribution and absence of pinhole defects in the mesoporous material.

From the studies discussed above it is clear that such anodic alumina – mesoporous material composite membranes are of great interest for potential applications as molecular separators[123,131,132,136,126] or as host material for the inclusion of conducting or semi-conducting nanostructures.[119,122,129,130] However, subtle changes in stoichiometry and reaction conditions can lead to striking changes in mesopore order and morphology. A greater understanding of the mechanism and the ability to tune these intriguing structures at will is highly desirable. In the following chapters of this thesis, data from *ex situ* and *in situ* 2D SAXS and GISAXS studies will be presented that provide quantitative information about the composition of even mixed phases and their temporal evolution during the EISA process. The diffraction experiments will be combined with transmission electron microscopy that permits the investigation of spatial variations of the structures formed in confined spaces.

References

[1]   IUPAC, Manual of Symbols and Terminology, Appendix 2, Colloid and Surface Chemistry, *Pure Appl. Chem.* **1972**, *31*, 578.

[2]   C. T. Kresge, M. E. Leonowicz, W. J. Roth, J. C. Vartulli, J. S. Beck, *Nature* **1992**, *359*, 710.

[3]   C. Li et al., *Chem. Mater.* **2007**, *19*, 173.

[4]   Pinnavaia et al., *Science* **1995**, *267*, 865-867.

[5]   Zhao et al., *Science* **1998**, *279*, 548-552.

[6]   N. R. B. Coleman, G. S. Attard, *Micr. Mes. Mat.* **2001**, *44-45*, 73.

[7]   N. K. Raman, M. T. Anderson, C. J. Brinker, *Chem. Mater.* **1996**, *8*, 1682.

[8]   Q. Huo et al., *Chem. Mater.* **1994**, *6*, 1176.

[9]   D. Zhao, Q. Huo, J. Feng, B. F. Chmelka, G. D. Stucky, *J. Am. Chem. Soc.* **1998**, *120*, 6024.

[10]   G. S. Attard, J. C. Glyde, C. G. Göltner, *Nature* **1995**, *378*, 366.

[11]   A. Monnier et al., *Science* **1993**, *261*, 1299.

[12]   F. Schüth, *Ber. Bunsen-Ges. Phys. Chem.* **1995**, *99*, 1306.

[13]   S. Hitz, R. Prins, *J. Catal.* **1997**, *168*, 194.

[14]   S. Kawi, M. W. Lai, *Chem. Commun.* **1998**, *13*, 1407.

[15]   J. S. Beck at al., *J. Am. Chem. Soc.* **1992**, *114*, 10834.

[16]   Y. Sakamoto, T.-W. Kim, R. Ryoo, O. Terasaki, *Angew. Chem. Int. Ed.* **2004**, *43*, 5231.

[17]   C. Gao et al., *Chem. Mater.* **2006**, *18*, 3904.

[18]   P. Yang, D. Zhao, D. I. Margolese, B. F. Chmelka, G. D. Stucky, *Chem. Mater.* **1999**, *11*, 2813.

[19]   D. Grosse et al., *Nature Mat.* **2004**, *3*, 787.

[20]   M. J. MacLachlan, N. Coombs, G. A. Ozin, *Nature* **1999**, *397*, 681.

[21]   P. N. Trikalitis, K. K. Rangan, T. Bakas, M. G. Kanatzidis, *Nature* **2001**, *410*, 671.

[22] U. Ciesla, S. Schacht, G. D. Stucky, K. K. Unger, F. Schüth, *Angew. Chem. Int. Ed.* **1996**, *35*, 541.

[23] D. Sun et al., *Nature* **2006**, *441*, 1126.

[24] F. Schüth, *Angew. Chem. Int. Ed.* **2003**, *42*, 3604.

[25] M. Choi, R. Ryoo, *Nature Mat.* **2003**, *2*, 473.

[26] F. Hoffmann, M. Cornelius, J. Morell, M. Fröba, *Angew. Chem. Int. Ed.* **2006**, *45*, 3216.

[27] Q. Huo et al., *Adv. Mater.* **1997**, *9(12)*, 974.

[28] D. E. De Vos, M. Dams, B. F. Sels, P. A. Jacobs, *Chem. Rev.* **2002**, *102*, 3615.

[29] S. J. L. Billinge, et al., *J. Am. Chem. Soc.* **2005**, *127*, 8492.

[30] V. Rebbin, R. Schmidt, M. Fröba, *Angew. Chem. Int. Ed.* **2006**, pNA (published online).

[31] C.-Y. Lai et al., *J. Am. Chem. Soc.* **2003** *125*, 4451.

[32] I. Roy et al., *PNAS* **2005**, *102*, 279.

[33] B. D. Hatton et al., *Adv. Funct. Mater.* **2005**, *15(5)*, 823.

[34] H. K. Baca et al., *Science* **2006**, *313*, 337.

[35] Y. Lu et al., *Nature* **1997**, *389*, 364.

[36] D. Zhao et al., *Adv. Mater.* **1998**, *10(16)*, 1380.

[37] C. J. Brinker, Y. Lu, A. Sellinger, H. Fan, *Adv. Mater.* **1999**, *11(7)*, 579.

[38] S. Besson, T. Gacoin, C. Ricolleau, C. Jacquiod, J.-P. Boilot, *J. Mater. Chem.* **2003**, *13*, 404.

[39] F. Cagnol et al., *J. Mater. Chem.* **2003**, *13*, 61.

[40] D. Grosso et al., *Adv. Funct. Mater.* **2004**, *14(4)*, 309.

[41] G. E. Thompson, *Thin Solid Films* **1997**, *297*, 192-201.

[42] G. E. Thompson, R. C. Furneaux, G. C. Wood, J. A. Richardson, J. S. Goode, *Nature* **1978**, *272*, 433.

[43] H. Masuda, K. Fukuda, *Science* **1995**, *268*, 1466.

[44]   K. Nielsch, J. Choi, K. Schwirn, R. B. Wehrspohn, U. Gösele, *Nano Letters* **2002**, *2(7)*, 677.

[45]   G. E. Thompson, G. C. Wood, *Nature* **1981**, *209*, 230.

[46]   T. Iijima, S. Kato, R. Ikeda, S. Ohki, G. Kido, M. Tansho, T. Shimizu, *Chem. Lett.* **2005**, *34(9)*, 1286.

[47]   H. Shiraki, Y. Kimura, H. Ishii, S. Ono, K. Itaya, M. Niwano, *Appl. Surf. Sci.* **2004**, *237*, 369.

[48]   K. Ha, H.-J. Ahn, *Liquid Crystals* **2004**, *31(11)*, 1525.

[49]   C. A. Melendres, S. van Gils, H. Terryn, *Electrochem. Commun.* **2001**, *3*, 737.

[50]   S. Rana, S. Ram, *J. Solid State Chem.* **2001**, *157*, 40.

[51]   R. S. Friedman, M. C. McAlpine, D. S. Ricketts, D. Ham, C. M. Lieber, *Nature* **2005**, *434*, 1085.

[52]   C. R. Martin, *Science* **1994**, *266*, 1961.

[53]   W. Lou, M. Chen, X. Wang, Y. Zhang, W. Liu, *Chem. Lett.* **2006**, *35(8)*, 850.Q. M.

[54]   F.-L. Cheng, M.-L. Zhang, H. Wang, *Sensors* **2005**, *5*, 245.

[55]   M. R. Maschmann et al., *Nanotechnology* **2006**, *17*, 3925.

[56]   Zhang, Y. Li, D. S. Xu, Z. N. Gu, *J. Mater. Sci. Lett.* **2001**, *20*, 925.

[57]   H. Q. Cao et al., *Adv. Mater.* **2001**, *13*, 1393.

[58]   X. Xu et al., *Chem. Lett.* **2007**, *36(1)*, 112.

[59]   S. Wang, G. J. Yu, J. L. Gong, D. Z. Zhu, H. H. Xia, *Nanotechnology* **2007**, *18*, 015303.

[60]   S. Wang et al., *Nanotechnology* **2006**, *17*, 1594.

[61]   G. Zhang et al., *Nanotechnology* **2006**, *17*, 4252.

[62]   F. Tao et al., *Adv. Mater.* **2006**, *18*, 2161.

[63]   Y.-T. Liu et al., *Carbon* **2006**, *44*, 587.

[64]   S. Nicewarner-Pena et al., *Science* **2001**, *294*, 137.

[65]   S. Park, J. Lim, S. Chung, C. Mirkin, *Science* **2004**, *303*, 348.

[66] F. S. Ou, M. M. Shaijumon, L. Ci, D. Benicewicz, R. Vajtai, P. M. Ajayan, *Appl. Phys. Lett.* **2006**, *89*, 243122.

[67] M. R. Maschmann et al., *Nano Lett.* **2006**, 6(*12*), 2712.

[68] Y. Guo et al., *Chem. Mater.* **2006**, *18*, 1577.

[69] G. Lu, S. Ai, J. Li, *Langmuir* **2005**, *21*, 1679.

[70] O. Soubias, I. V. Polozov, W. E. Teague, A. A. Yeliseev, K. Gawrisch, *Biochemistry* **2006**, *45*, 15583.

[71] Y. Zhang et al., *Chem. Phys. Lett.* **2003**, *376*, 493.

[72] H. Chen, F. Zhang, S. Fu, X. Duan, *Adv. Mater.* **2006**, *18*, 3089.

[73] K. Tang et al., *J. Mater. Chem.* **2006**, *16*, 1741.

[74] C. N. Wu, K. J. Chao, T. G. Tsai, Y. H. Chiou, H. C. Shih, *Adv. Mater.* **1996**, *8(12)*, 1008.

[75] K. J. Chao et al., *US Patent 6,060,415*, **2000**.

[76] Whatman Anodisc, product information

[77] T. Yamashita et al., *Chem. Commun.* **2007**, 1160.

[78] S. Zhang, F. Cheng, Z. Tao, F. Gao, J. Chen, *J. Alloys Comp.* **2006**, *426*, 281.

[79] H.-J. Wang, *J. Am. Chem. Soc.* **2006**, *128*, 15954.

[80] T. Okamasa, G.-G. Lee, Y. Suzuki, N. Kasagi, S. Matsuda, *J. Micromech. Microeng.* **2006**, *16*, 198.

[81] T. Gao, G. Meng, L. Zhang, *J. Phys.: Condens. Matter* **2003**, *15*, 2071-2079.

[82] J. Choi, Y. Luo, R. B. Wehrspohn, R. Hillebrand, J. Schilling, U. Gösele, *J. Appl. Phys.* **2003**, *94(8)*, 4757.

[83] H. Masuda et al., *Adv. Mater.* **2006**, *18*, 213.

[84] N. V. Gaponenko et al., *Appl. Phys. Lett.* **2000**, *76(8)*, 1006.

[85] N. V. Gaponenko et al., *Mat. Sci. Eng. B* **2001**, *81*, 191.

[86] S. A. Klimin et al., *Phs. Lett. A* **2004**, *323*, 159.

[87]   F. Matsumoto, M. Harada, K. Nishio, H. Masuda, *Adv. Mater.* **2005**, *17*, 1609.

[88]   D.-K. Kim et al., *Anal. Chem.* **2007**, *79*, 1855.

[89]   R. Sanz, *Nano Lett.* **2006**, *6(5)*, 1065

[90]   J. Zou, X. Qi, L. Tan, B. J. H. Stadler, *Appl. Phys. Lett.* **2006**, *89*, 093106.

[91]   Anträge zum SFB 486, Teilprojekte B1 und B8

[92]   Ye, B., Trudeau, M. L. & Antonelli, D. M. *Adv. Mater.* **2001**, *13*, 561.

[93]   A. Fukuoka et al., *J. Am. Chem. Soc.* **2001**, *123*, 3373.

[94]   N. Petkov, N Stock, T. Bein, *J. Phys. Chem. B* **2005**, *109*, 10737.

[95]   M. L. Cohen, *Mater. Sci. Eng. C*, 2001. 15. 1-11.

[96]   Y. Xia, P. Yang, Y. Sun, Y. Wu, B. Mayers, B. Gates, Y. Yin, F. Kim and H. Yan, *Adv. Mater.,* 2003, 15, 353-383.

[97]   R. L. Rice, *Adv. Funct. Mater.* **2007**, *17*, 133.

[98]   M. Klotz, P.-A. Albouy, A. Ayral, C. Menager, D. Grosso, A. Van der Lee, V. Cabuil, F. Babonneau, C. Guizard, *Chem. Mater.* **2000**, *12*, 1721.

[99]   H. Miyata, T. Noma, M. Watanabe, K. Koroda, *Chem. Mater.* **2002**, *14*, 766.

[100] V. R. Koganti, S. E. Rankin, *J. Phys. Chem. B* **2005**, *109*, 3279.

[101] K. Kuraoka, Y. Tanaka, M. Yamashita, T. Yazawa, *Chem. Commun.* **2004**, 1198.

[102] E. M. Freer, L. E. Krupp, W. D. Hinsberg, P. M. Rice, J. L. Hedrick, J. N. Cha, R. D. Miller, H.-C. Kim, *Nano Lett.* **2005**, *5(10)*, 2014.

[103] C. Hellriegel, *Translational, Orientational and Spectral Dynamics of Individual Molecules in nano-Structured Materials Studied with Single-Molecule-Spectroscopy*, Dissertation zur Erlangung des Doktorgrades, LMU München **2005**.

[104] V. Kukla, et al., *Science* **1996**, *272*, 702.

[105] N. E. Benes, H. Jobic, H. Verweij, *Micr. Meso. Mat.* **2001**, *43*, 147.

[106] R. Rigler, Ü. Mets, J. Widengren, P. Kask, *Europ. Biophys. J.* **1993**, *22*, 169.

[107] M. J. Wirth, D. J. Swinton, M. D. Ludes, *J. Phys. Chem. B* **2003**, *107*, 6258.

[108] K. Bacia, S. A. Kim, P. Schwille, *Nature Meth.* **2006**, *3*, 83.

[109] Y. Fu, F. Ye, W. G. Sanders, M. M. Collinson, D. A. Higgins, *J. Phys. Chem. B* **2006**, *110*, 9164.

[110] C. A. Werley, W. E. Moerner, *J. Phys. Chem. B* **2006**.

[111] M. B. J. Roeffaers et al., *Nature* **2006** *439*, 572.

[112] C. Hellriegel et al., *J. Phys. Chem. B* **2004**, *108*, 14699.

[113] K. S. McCain, D. C. Hanley, J.M. Harris, *Analytical Chemistry* **2003**, *75*, 4351.

[114] C. Tardin, L. Cognet, C. Bats, B. Lounis, D. Choquet, *The EMBO Journal* **2003**, *22*, 4656.

[115] G. Seisenberger et al., *Science* **2001**, *294*, 1929.

[116] G. Kickelbick, *small* **2005**, *1*, 168.

[117] Z. Yang, Z. Niu, X. Cao, Z. Yang, Y. Lu, Z. Hu, C. C. Han, *Angew. Chem. Int. Ed.* **2003**, *42*, 4201.

[118] Q. Lu, F. Gao, S. Komarneni, T. E. Mallouk, *J. Am. Chem. Soc.* **2004**, *126*, 8650.

[119] D. Wang, R. Kou, Z. Yang, J. He, Z. Yang, Y. Lu, *Chem. Comm.* **2005,** 166.

[120] B. Yao, D. Fleming, M. A. Morris, S. E. Lawrence, *Chem. Mater.* **2004**, *16*, 4851.

[121] K. Jin, B. Yao, N. Wang, *Chem. Phys. Lett.* **2005**, *409*, 172.

[122] Y. Wu, G. Cheng, K. Katsov, S. W. Sides, J. Wang, J. Tang, G. H. Fredrickson, M. Moskovits and G. D. Stucky, *Nature Mater.* **2004**, *3*, 816.

[123] A. Yamaguchi, F. Uejo, T. Yoda, T. Uchida, Y. Tanamura, T. Yamashita and N. Teramae, *Nature Mater.* **2004**, *3*, 337.

[124] A. Y. Ku, S. T. Taylor, S. M. Loureiro, *J. Am. Chem. Soc.* **2005**, *127*, 6934.

[125] A. Y. Ku, S. T. Taylor, W. J. Heward, L. Denault, S. M. Loureiro, *Micr. Mesop. Mater.* **2006**, *88*, 214.

[126] S. Yoo, D. M. Ford, D. F. Shantz, *Langmuir* **2006**, *22*, 1839.

[127] F. Marlow, I. Leike, C. Weidenthaler, C. W. Lehmann, U. Wilczok, *Adv. Mater.* **2001**, *13(5)*, 307.

[128] F. Kleitz, F. Marlow, G. D. Stucky, F. Schüth, *Chem. Mater.* **2001**, *13*, 3587.

[129] D. J. Cott et al., *J. Am. Chem. Soc.* **2006**, *128*, 3920.

[130] N. Petkov, B. Platschek, M. A. Morris J. D. Holmes, T. Bein, *Chem. Mater.* **2007**, *19*, 1376.

[131] T. Yamashita et al., *Analyt. Sci.* **2006**, *22*, 1495.

[132] A. Yamaguchi et al., *Analyt. Chim. Acta* **2006**, *556*, 157.

[133] F. Hofmeister, *Arch. Exp. Pathol. Pharmakol.* **1888**, *24*, 247.

[134] A. Yamaguchi et al., *J. Phys. Chem. B* **2006**, *110*, 3910.

[135] V. Antochshuk, M. Jaroniec, *Chem. Mater.* **2000**, *12*, 2496.

[136] A. Yamaguchi, T. Yoda, S. Suzuki, K. Morita, N. Teramae, *Analyt. Sci.* **2006**, *22*, 1501.

II. Experimental Methods

1. General synthesis of composite membranes

The method used for the self-assembly of the ordered silica/surfactant nanocomposites in the channels of the anodic alumina membranes (AAMs) is depicted in Figure 1. The AAMs used in this study are commercially available (47 mm, Anodisc^{TM}, Whatman) and show almost hexagonal packing of vertical pores with diameters in the range of 120 –200 nm, extending through the whole membrane thickness (Figure 2a). The synthetic mixtures were introduced into the pores of the AAM by soaking the membranes at room temperature in a flat pool of liquid.
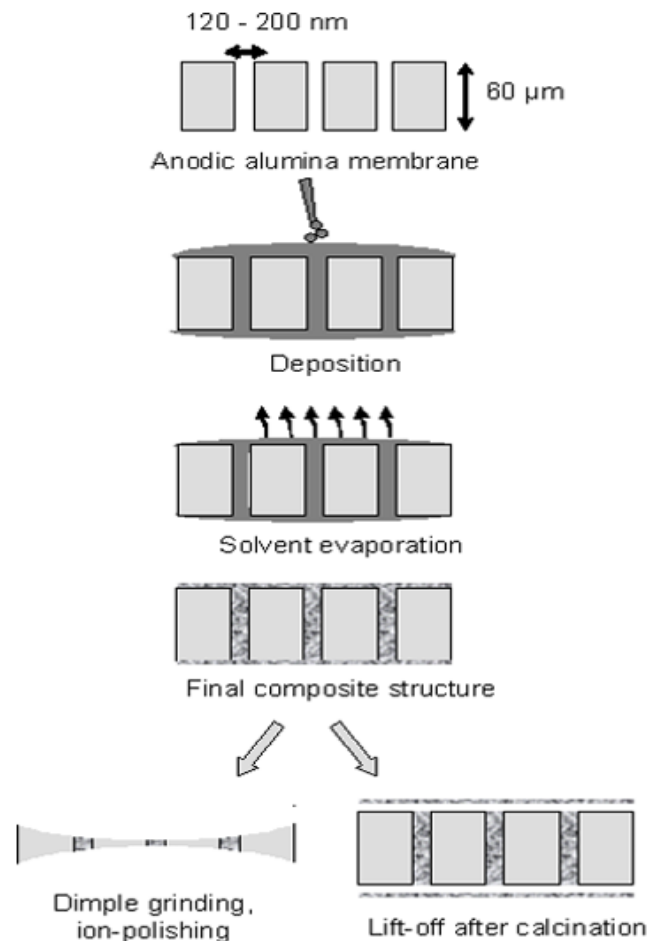
Figure 1: Schematic representation of the synthetic steps to obtain mesostructured silica/surfactant nanocomposites in the AAMs.

The synthetic mixtures contain a silica precursor, the templating surfactant, and water and ethanol as volatile solvents. Detailed recipes are given in Chapter III together with the

discussion of the corresponding samples at the end of the respective sections. Due to the solvent evaporation that progressively increases the concentration of the surfactant and other non-volatile components of the synthetic mixtures; the self-assembly process is driven towards micellization and silica condensation followed by a disorder-to-order transition, providing the final, extended mesophase structure.

Assuming a mean channel diameter of 200 nm, 0.06 mm membrane height, 50% porosity of the AAMs, and an effective membrane diameter of 40 mm (excluding the surrounding Polymer support)[1], the accessible volume of an AAM can be estimated as being 18 µl ($1.8 \cdot 10^9$ nm^3 per AAM channel, $1 \cdot 10^5$ channels on one AAM). Further assuming the pore volume of SBA-15 powder material (0.56 µl/mg[2]), the density of non-porous silica (0.4 µl/mg), and the specific gravity for Pluronic P123 (1.01[3]) the volume of 18 µl corresponds to 29 mg[a] uncalcined mesostructured silica (templated with P123, the pores assumed to be randomly filled with template in uncalcined material). Dry samples were found to be 40-50 mg heavier than the respective empty AAMs, depending on the synthesis conditions (e.g., surfactant used and surfactant:silica ratio). These findings suggest that an additional thin film formed on the planar membrane surface (see Figure 1). In a sample synthesized with Pluronic P123 and having hexagonal structure, the surface film was scratched off, and about 30 mg material was found to have formed inside the AAM channels.[4] Therefore we assume a complete filling of the AAM channels with mesostructured material following the synthesis procedure depicted in Figure 1.

This assumption is supported by scanning electron microscopy (SEM) images of the AAM before and after loading with mesoporous silica templated with Pluronic123, respectively (Figure 2). Pure AAMs showed well aligned, almost regularly arranged nanochannels (Figure

---

[a] {1/(0.4+0.56)}+0.56=1.6 mg/µl, and 29 mg / 18 µl

2a). After the assembly of the mesoporous silica structures, well-shaped nanoscopic filaments are observed protruding from the openings of the AAM-channels by employing CTAB or Pluronic 123 as structure directing agents (Figure 2c and d). Figure 2b depicts the uniformity and continuity of the as-deposited nanostructures, viewed normal to the channel-direction of the membrane, while Figure 2e shows the isolated mesoporous 1D nanofibers obtained by dissolution of the AAM matrix in phosphoric acid. EDX measurements taken along the whole membrane thickness showed similar Al/Si atomic ratios, demonstrating the continuous and homogeneous filling of the membrane with the silica/surfactant nanocomposites.
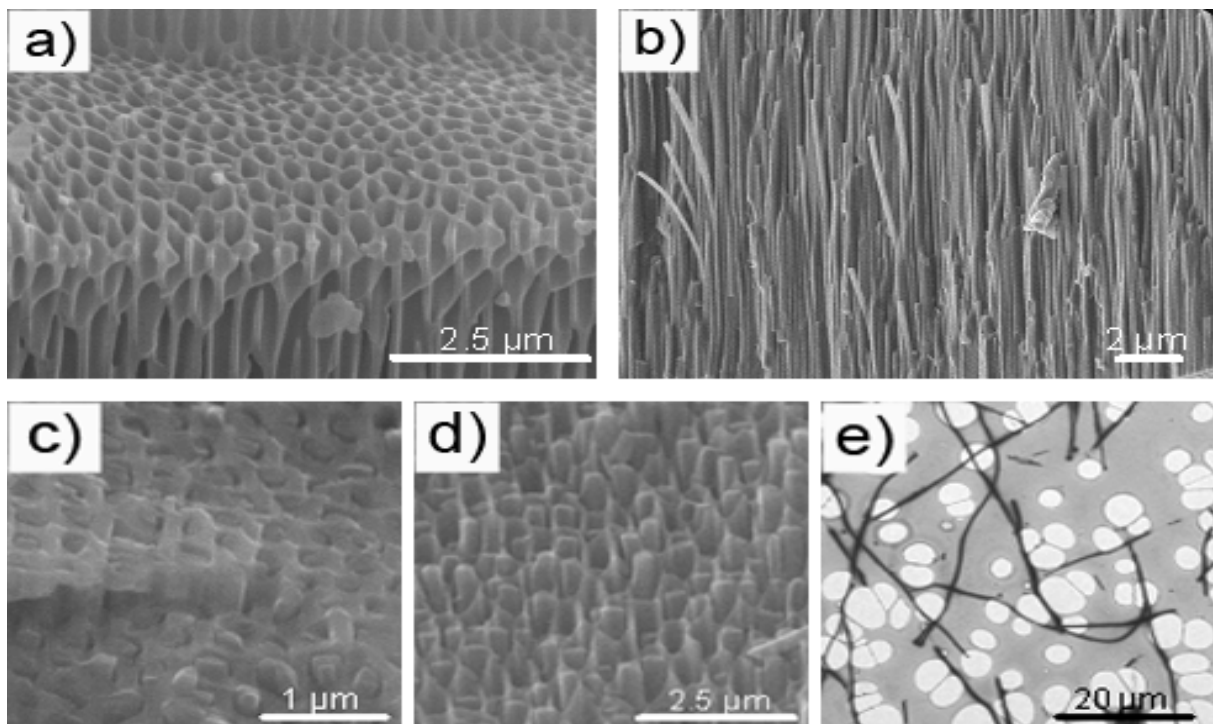
Figure 2: Side-view SEM images showing the morphology of the AAMs a) before and b) (sample with Pluronic123) after inclusion of mesoporous silica. SEM images of silica filaments, encapsulated within pores of AAMs, templated with c) CTAB and d) Pluronic123. f) TEM of isolated silica filaments imaged on a holey carbon grid.

2. Film synthesis

Similar synthetic mixtures are used as for the synthesis of the composite membranes. The detailed recipes are given with the discussion of the results (Chapter III, Section 8.3). The samples were prepared by spin-coating of the EISA precursor solutions on glass slides (Marienfeld, size: 20 × 20 mm, thickness: 170 μm). The glass surface was previously cleaned by ultra-sonication in 0.5% Hellmanex II solution (Hellma) at 50°C, followed by five minutes rinsing with de-ionized water.

3. Characterization

3.1. X-ray Diffraction

Mesostructured silica films prepared on flat substrates were measured in a Bragg-Brentano geometry using an XDS 2000 diffractometer (Scintag).

Mesostructured silica/AAM composite membranes were investigated in transmission by 2D SAXS measurements obtained with a SAXSess Small Angle X-ray Scattering System by Anton Paar. The signal was either recorded on image plates or with a CCD-detector after collecting the pattern for 1h.

3.1.1. Introduction to the method

X-ray diffraction is often used to determine the structure of a sample. It is based on the interaction of monochromatic radiation with matter. A fraction of the incident beam will be absorbed by the material, the rest is incoherently or coherently scattered. X-ray photons can be absorbed when they expel electrons from an atom. Incoherent scattering involves transmission of a fraction of the photon energy onto an electron. X-rays from incoherent scattering processes have different wavelengths than the incident radiation. They are

contributing to the featureless background radiation. The wavelength of coherently scattered radiation remains unchanged; interference phenomena can be observed.

Coherent scattering can be described as incident radiation that induces the electrons of the material to oscillate and thus emit radiation with the same frequency as the incoming X-rays. Figure 3 shows, in a schematic view, how an incident beam hits a line of scattering centers that start emitting spherical waves with the same wavelength; these waves interfere with each other. If the scattering centers are arranged in a periodic manner (point lattice), interference produces a regular pattern of intensity maxima and minima. For clarity, only the maxima of the waves are drawn in Figure 3. Wave maxima with the same distance from the respective scattering center are marked with the same color. The transmitted beam at zero angle is represented by the dotted line drawn through intersections of phase maxima having the same color. Additional positive interference occurs at higher angles marked by the dotted lines through intersections of phase maxima at different distances from their respective scattering centers (maxima with different colors in Figure 3). Again, only the intersections of the wave maxima are marked in the scheme but of course the positive interference occurs everywhere along the dotted lines that represent what are the Laue cones[5] in a three-dimensional illustration. The beam is diffracted at different angles if

i) the wavelength of the incident radiation changes

ii) the distance between the scattering centers (d-spacing) changes, according to the Bragg equation $n\lambda = 2d \sin\theta$.[6]

The position of the diffracted beam is recorded either in scattering angles (2θ /degree) or as a certain length of the scattering vector in reciprocal space (q /nm^{-1}). The scattering angle and the length of the scattering vector are correlated through the equation $q\cdot\lambda = 4\pi\cdot\sin\theta$. Thus the scattering vector is $q = (2\pi/d)\cdot n$.[7]
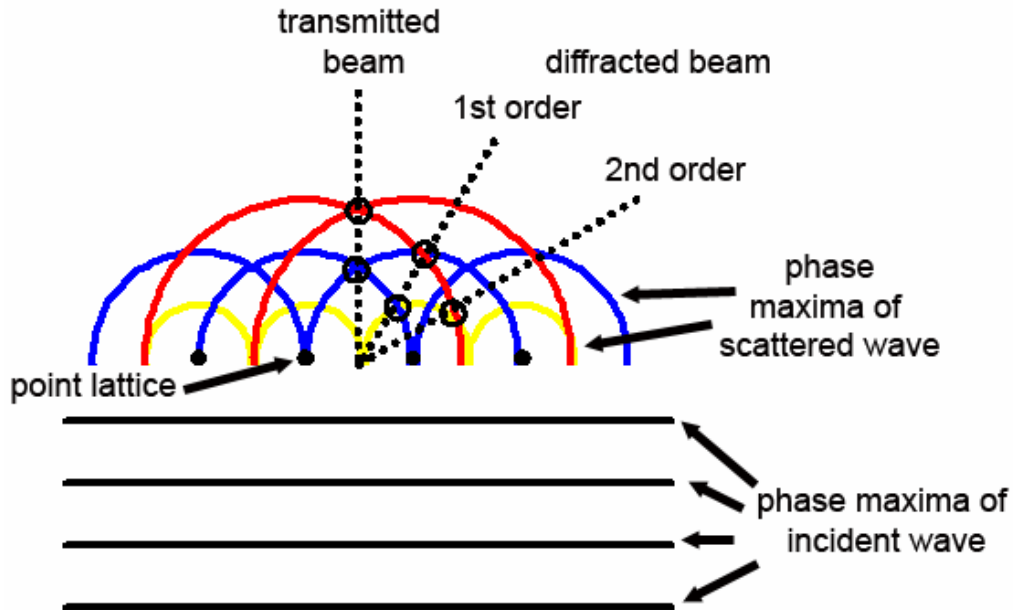
Figure 3: Schematic diagram illustrating the principle of diffraction at a one dimensional point lattice in transmission. The maxima of the waves are drawn as lines. Maxima of the emitted waves that have the same distance from their respective scattering centers are marked with the same color (yellow, blue, or red). Positive interference occurs everywhere along of the black, dotted lines.

The diffraction pattern can be recorded in backward direction (reflection geometry) or in forward direction (transmission geometry as in the 2D SAXS experiments). It is either recorded with one-or two-dimensional resolution, extracting information about either only the d-spacing of the lattice planes of a crystal, or additional information about possible angles between respective sets of lattice planes. The diffraction pattern of a single crystal shows point-shaped reflections perpendicular to the respective lattice planes in real space. Sets of lattice planes with the same d-spacing have the same distance from the origin (the origin is the transmitted beam); the angles between the diffraction spots represent the angles between the different sets of lattice planes (azimuth angle φ). In a powder pattern, the diffraction patterns of many crystallites superimpose, resulting in ring-shaped reflections surrounding the origin at a certain distance representative for the d-spacing of the respective set of lattice planes. Angular information cannot be extracted.

II. Experimental Methods

The mesostructured samples investigated in this thesis are in the form of thin films or composite membranes and have crystal-like order in the direction of one axis but no preferred orientation in the plane perpendicular to that axis. Thus, they can be described as two-dimensional powders. Their diffraction pattern shows ring-shaped intensity maxima when diffraction is recorded from the plane without preferred orientation and the single domains are smaller than the size of the primary beam (axis of crystal-like orientation is parallel to the incident beam). When the diffraction pattern is recorded from the plane including the axis of preferred orientation (axis of crystal-like orientation is perpendicular to the incident beam), point-shaped intensity maxima are observed.[8] The diffraction patterns of such samples are discussed in detail in the following section.

Diffraction patterns from mesostructured samples show periodicity at comparatively small angles due to the large d-spacings of these phases in real space. X-ray scattering at such small angles was originally used to determine the shape or size of particles in solution. This is possible because a scattering or diffraction pattern always includes information of the structure- and the form-factor (S(q) or P(q), respectively) as schematically shown in Figure 4. The scattered intensity at a certain value for q is given as:

$$I(q) = K \cdot P(q) \cdot S(q).$$

K is a constant consisting of the X-ray contrast of the material, the sample volume, and possibly the concentration of the scattering matter, for example if dealing with solutions. For interpreting the structure- and form-factor, K is of no importance since any information can be extracted if I(q) is in arbitrary units.[7]
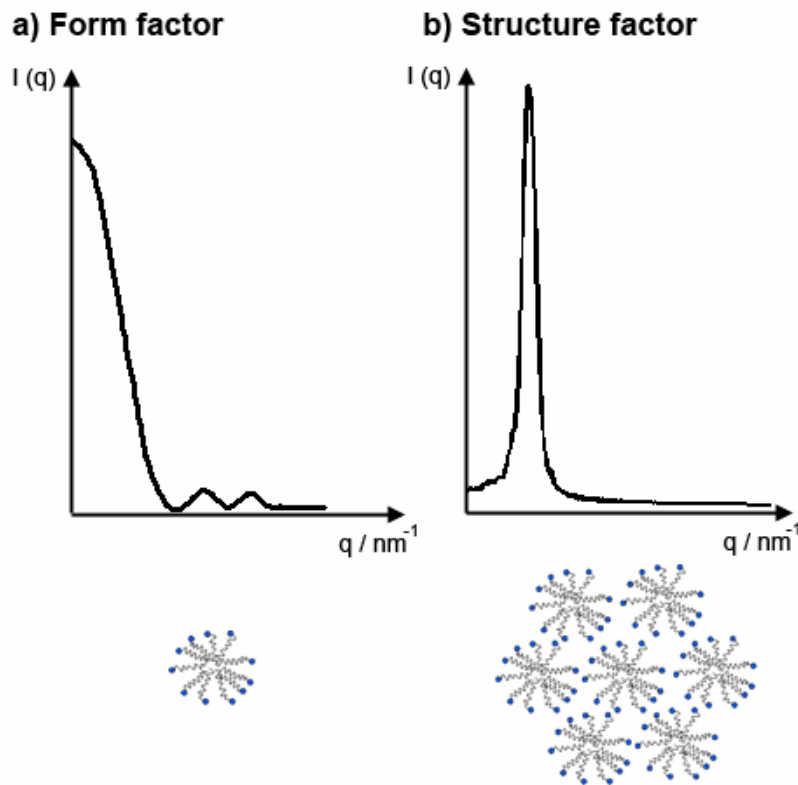
Figure 4: Typical scattering profiles of
   a)   a diluted solution of spherical particles (dominant form factor)
   b)   an ordered array of particles (dominant structure factor).

The structure factor describes the diffraction pattern from particles arranged in a periodic manner (Bragg peaks). If particles are far away from each other, for instance in a dilute solution, the structure factor becomes one and the form factor is dominant for the intensity profile. The form factor can be extracted if the particles under investigation contain

i) more than one scattering center and

ii) an electron density unlike that of the matrix (e.g. the solvent).

The form factor is the Fourier transform of the electron density of the particle. It would be merely a constant if the particle would be a point, but in reality it is oscillating if the particle has spherical, cylindrical, or lamellar shape (see Figure 4a for a spherical particle). The scattering profile of the form factor can be divided in three regimes, the Guinier regime (the Gaussian shaped decay at very small angles), the Fourier regime (the oscillations), and the Porod regime (slope of decay of the oscillations). From the Guinier regime the radius of gyration R_G can be extracted as size parameter. The average particle radius can be calculated

from R_G according to $R = (5/3)^{1/2} R_G$ if the particles are spherical and exhibit homogeneous density. For other particle shapes, other equations can be used to determine the average radius. The overall decay of the scattering profile at larger angles is the Porod regime and follows K_P/q^4. The constant K_P is proportional to the surface per sample volume. An estimate of the particle shape can be obtained by the power law of the form factor at small angles. In a double logarithmic plot, an initial slope of 0, -1, or -2 indicate the presence of spherical, cylindrical, or lamellar particles, respectively. The oscillating part of the scattering profile gives more detailed information about the particle shape. It is investigated by transforming it into an I(r)-plot by Fourier methods, where r is a distance in nm (real space). Those plots are called pair-distance distribution functions (PDDFs) and are histograms of distances that can be found within a particle. Spherical particles result in a symmetrically shaped profile; cylindrical particles have an early maximum with a linear tail. The intercept with the x-axis represents the longest distance that can be found within a particle. Core-shell particles as well as aggregates of particles can be identified by the PDDFs.[7]

However, scattering profiles are often products of the form- and the structure factor. In a recent publication, SAXS data of thin mesostructured films were obtained and SAXS profiles were measured showing the Bragg peaks from the periodically arranged silica-micelle material plus additional minima right after the peaks originating from the form factor of the surfactant micelles.[9] By fitting the scattering data, information about size distributions of the micelles (polydispersity), lattice distortions, and the thickness of the silica wall are obtained.

3.1.2. Description of the experiments

The geometry of the SAXS experiments is shown in Figure 5, depicting a composite membrane having a pure columnar hexagonal mesophase as example. The samples are measured in transmission; only reflections from lattice planes that are parallel to the primary

beam are detected, because $1/\lambda$ is much larger than the distance of the lattice planes. The primary beam is collimated to 0.5 mm x 1.0 mm to obtain two-dimensional diffraction patterns and weakened by a semi-transparent beam stop before detection. The samples were slightly tilted towards the primary beam in order to obtain higher diffracted intensities. A tilting angle of 10° was found to be the optimum. A sample holder was developed to assure reproducible measurement conditions for each sample. A systematic investigation confirming the reproducibility and comparability of the diffraction data was carried out.[10]
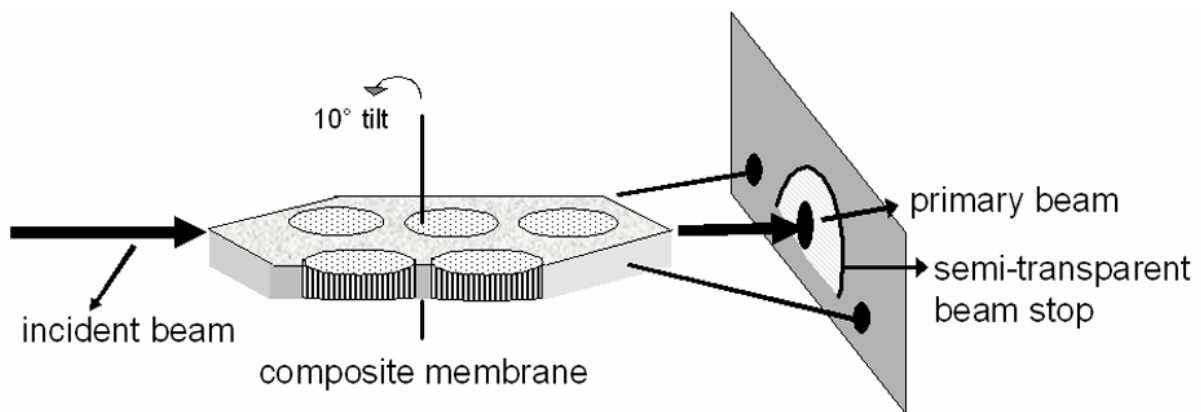
Figure 5: Measuring geometry of the transmission SAXS experiments. The primary beam is weakened by a semi-transparent beam stop. Only the upper half of the diffraction pattern is recorded due to the geometry of the instrument used. The sketch shows a columnar hexagonal mesophase structure as example (hexagonally ordered mesopores fully aligned along the channels of the AAMs).

An overview of the observed structures within the AAM channels and their respective diffraction patterns in the given measuring geometry is depicted in Figure 6. The cylindrical geometry of the circular hexagonal phase, forming either rings or spirals (Figure 6a, b), is also represented in reciprocal space. The intersection of the ring-shaped intensity maxima with the Ewald sphere gives an X-ray diffraction pattern showing two reflections in the horizontal plane of the primary beam (in-plane along q_x, 'ip reflections') and two out-of-plane reflections ('oop reflections'), all resulting from ring-shaped intensity maxima in reciprocal space that correspond to 10-type reflections of a normal hexagonal lattice.[11] The missing two diffraction spots, below the membrane surface, are shadowed by the bottom of the apparatus. The columnar hexagonal structure (Figure 6c) exhibits only two ip reflections corresponding

to 10. In this case the rotational symmetry in reciprocal space results from numerous crystal-like domains rotated against each other around the z-axis, parallel to the pore channels (Figure 6c, compare Page 44).

The lamellar structure depicted in Figure 6d shows ring-shaped intensity maxima in reciprocal space that reflect the ring-shape of the silica-sheets and that result in two in-plane reflections. In summary, the observation of out-of-plane reflections provides evidence for the presence of the circular hexagonal structure only. In contrast, the in-plane reflections can result from the circular hexagonal, the columnar hexagonal, or the lamellar phase, respectively.

All patterns can be described as superpositions of the patterns typical for the columnar or lamellar phase and those with the circular structure. The ip reflections will be preserved in any case whereas both oop reflections should appear with decreased intensity in case of mixed structures. The intensity ratio of the oop-reflections by the ip-reflections (oop:ip ratio) corresponds to the ratio of the volumes adapting the respective structures.

The oop:ip ratio can provide a semiquantitative estimate of the phase distribution within one sample since there may be systematic deviations from the theoretical estimate due to the measurement geometry (in-plane scattered waves may have a longer pathway through the sample than out-of-plane waves which would lead to a systematically lower intensity of the ip-reflections). Thus, reference samples were always synthesized and distinct changes of the oop:ip ratios are discussed in comparison to these reference samples.

Furthermore, the oop:ip ratios vary depending on how the intensity of the reflections is determined. Therefore, determination of the oop:ip ratio was always carried out the same way by using a azimuthal angle integration (SAXSquant software by Anton Paar) followed by

dividing the peak heights of the oop- and ip-reflections after subtraction of the background intensity visible as baseline in the one-dimensional intensity profile after azimuthal integration. Variations of +/- 0.1 of the oop:ip ratio were found to be within the accuracy limit of this method (derived from multiple measurements of one and the same sample).[10]
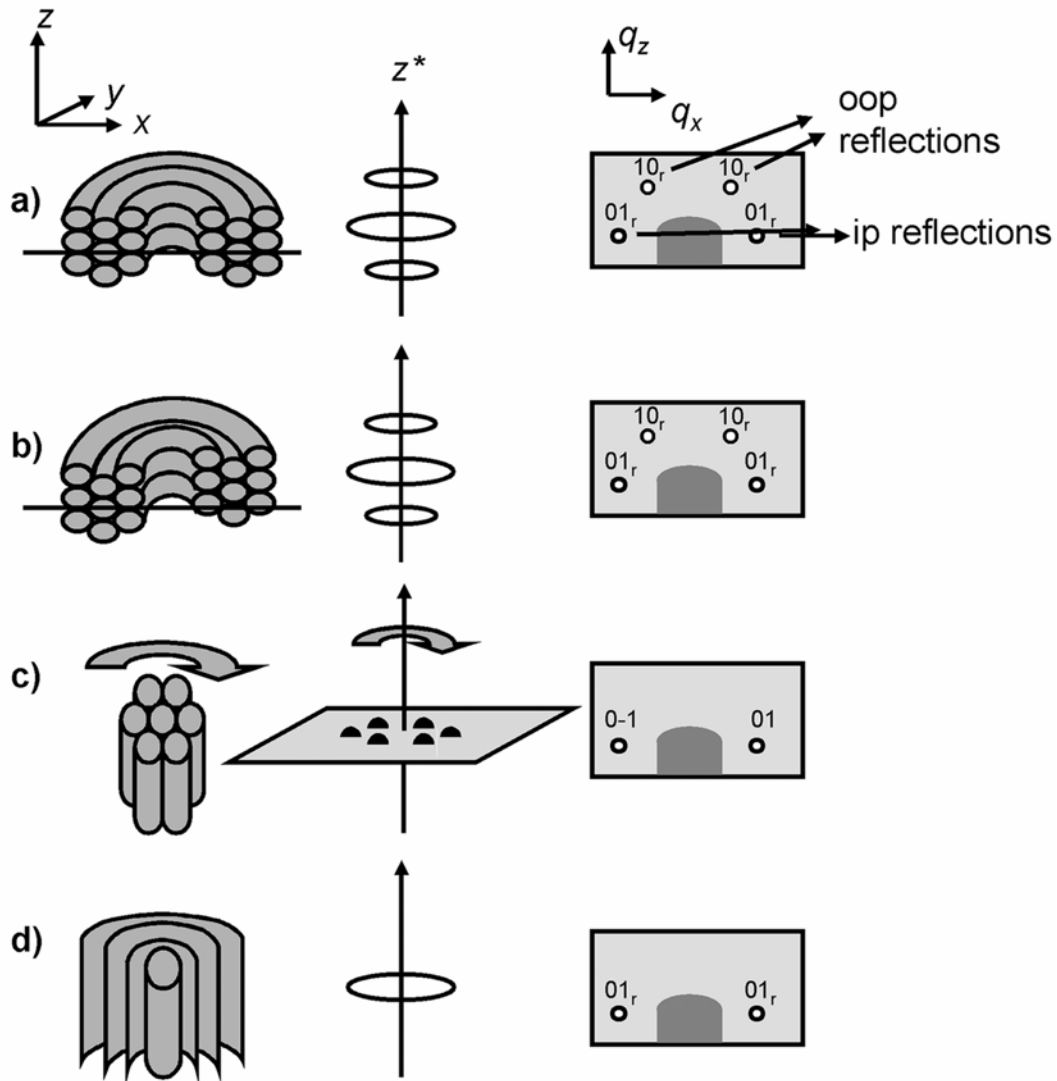
Figure 6: Sketch of the observed structures within the AAM-channels and description of their intensity-maxima in reciprocal space and their respective diffraction pattern corresponding to the 10 reflection of a normal hexagonal (a-c) or lamellar (d) lattice. The circular hexagonal structure forming rings (a) or spirals (b) results in two in-plane (ip) and two out-of-plane (oop) reflections. The columnar hexagonal structure (c) and the lamellar phase (d) both result in two in-plane reflections. In case of the columnar phase, the indexing of one reflection as 01 defines a coordinate system, hence the opposed ip-reflection is indexed 0-1. In contrast, in case of the lamellar phase, both ip-reflections stem from the same ring-shaped intensity maxima and therefore are both indexed as 01_r. The index "r" denominates "ring" for reflections from ring-shaped intensity maxima. The same principle is valid for the circular hexagonal structure. Hence, the ip-reflections are indexed as 01_r, and the oop-reflections are indexed as 10_r, referring to a normal hexagonal lattice.[9]

The intensity distribution of the columnar hexagonal structure in reciprocal space (c) is ring-shaped as well, corresponding to the formation of crystal-like domains rotated against each other around the z*-axis. The pure lamellar phase (d) shows sheets with increasing curvature when located closer to the center, finally forming one tube.

The detection of the lamellar structure is more difficult for the following reasons. In the given diffraction geometry both the columnar and tubular lamellar phases only show reflections in the in-plane directions. In addition, the vertically oriented channels of the amorphous alumina membrane lead to a strong background in the in-plane direction. With appropriately high resolution (e.g. at the synchrotron) it is possible to distinguish the lamellar phase from the hexagonal ones by their first order reflections since they appear at different 2θ-values. In a lamellar structure the lattice constant matches the d-spacing, but in hexagonal structures the d-spacing is smaller by a factor of sin(120°). However, this approach is limited when the d value becomes larger, since the intensity maxima will be closer together until it becomes impossible to separate them. Moreover, it will be always necessary to show diffraction data from a hexagonal and a lamellar phase to prove their existence.

3.2. In situ 2D GISAXS experiments

3.2.1. Introduction to the method

The main difference between SAXS and SAXS in grazing incidence geometry (GISAXS) is that measurements at grazing incidence are surface sensitive.[12] Thus, it is an optimal technique to investigate structured thin films that are deposited on a substrate. Depending on the angle of incidence, the incoming beam is more strongly reflected or refracted from a sample (Figure 7). In transmission, the beam is passing through the sample (Figure 7, red lines). Most of the beam would be absorbed, diffracted, or scattered from the substrate while the thin film on the surface would hardly contribute to the scattering or diffraction intensity. If the angle of incidence is lower (Figure 7, blue lines), the primary beam is partially transmitted through the sample and partially reflected. The reflected beam becomes more intense and the transmitted beam weaker if the angle of incidence is lowered (Figure 7, yellow lines). At the critical angle of the sample, the entire beam is specularly reflected and the surface sensitivity is maximized. Thus, GISAXS means performing one- or two dimensional X-ray scattering

experiments with an incident angle close to the critical angle of the material investigated. The penetration depth into the sample can be tuned by varying the incident angle. Most GISAXS experiments are carried out using synchrotron radiation, taking advantage of the high intensity of this radiation to perform *in situ* measurements.
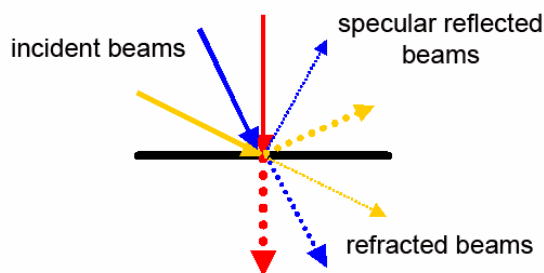
Figure 7: Schematic illustration of the dependence of the refracted and reflected beam intensities on the angle of the incident beam. The incident beams are solid lines. The reflected and refracted beams are dotted lines with different thickness illustrating stronger or weaker intensity.

3.2.2. Description of the experiment

Structure formation in the confined environment of the AAM channels was investigated *in situ*. Thus, the membranes had to be mounted on a Teflon plate during the measurements (see synthesis procedure: Chapter II, Section 1). The beam was aligned in grazing incidence onto the membranes (for the geometry of the measurement see Figure 8). The measurements were performed at the 1-BM beamline at the APS at ANL, Argonne, IL, USA. The sample-detector distance was 1040 mm, the wavelength of the primary beam was 1.24 Å. The angle between primary beam and sample substrate was 0.175° ($2\theta = 0.35°$). Additional scattering in air was avoided by He-filled tubes between the final beamline slit and the sample and between sample and detector. Every three minutes a diffraction pattern was recorded. After every measurement a background image of the detector was recorded. The time intervals between the measurements were limited by the detector readout speed.

In some samples, the temporary formation of a structured film on top of the AAM surface was observed in addition to the formation of periodic phases within the AAM-channels. The

diffraction spots corresponding to surface structures in case of the 2D-hexagonal phase could be distinguished by their different azimuthal angle, and were observed to be much sharper than reflections from structures within the channels (Figure 9).
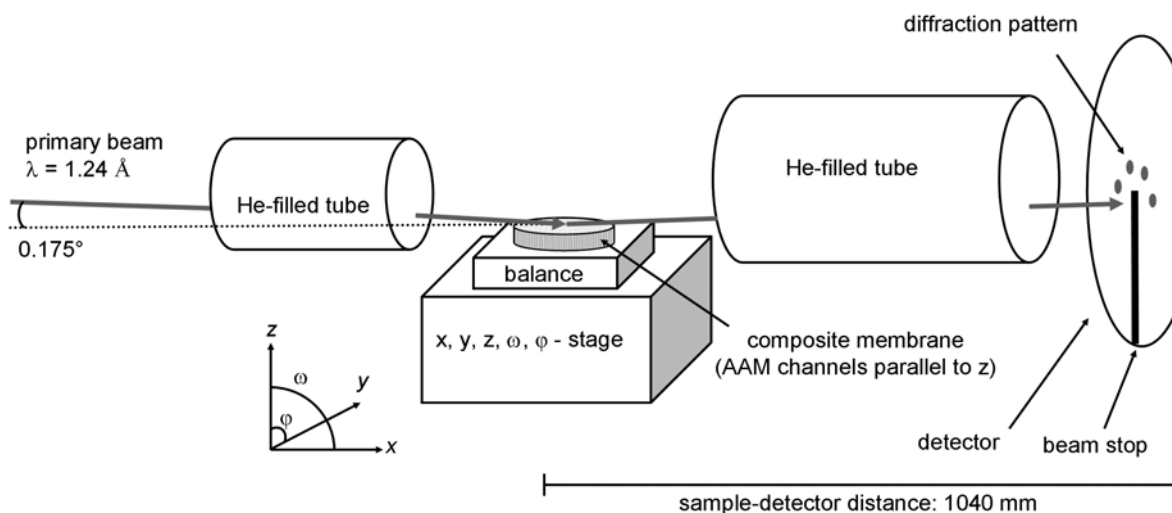
Figure 8: Geometry for the *in situ* GISAXS experiments. The incident X-rays hit the sample almost parallel to the planar AAM-surface, the primary beam is fully shadowed by a beam stop. The samples were mounted on a balance recording the weight loss.
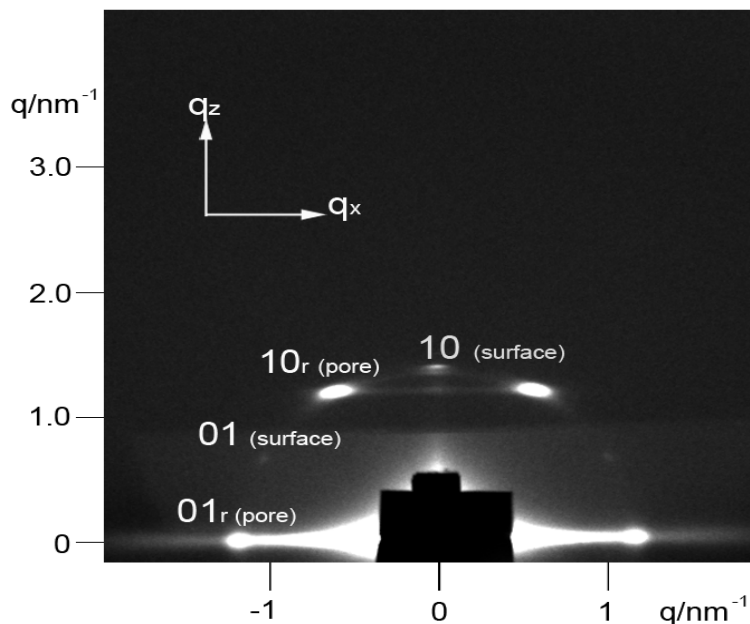
Figure 9: Diffraction pattern of a sample synthesized with Brij 56 at 40% r.h., recorded 45 minutes after the initiation of the experiment. The sharp reflections correspond to a hexagonally structured layer on top of the AAM, the broader, bright reflections correspond to a circular hexagonal structure formed inside the AAM channels. Those reflections are positioned on a ring representing the same 2θ-value, but occur at different azimuthal angles. The in-plane reflections are superimposed by diffuse scattering from the AAM. As the channels of the AAM are aligned along the z-axis, the diffuse scattering is mainly observed in q_x-direction, and it becomes weaker with increasing distance to the primary beam. The scale bar is given in $q = 2\pi/d$.

3.2.3. Evaluation of the *in situ* data

Examples of diffraction patterns obtained from samples synthesized with Brij 56 and P123 at two different surfactant:silica ratios are shown in Figure 10a-b and c-d, respectively. The temporal evolution of the integrated intensities of the reflections corresponding to the different phases is evaluated.[13] If only a circular hexagonal phase is forming, the temporal evolution of the intensities of the oop- and the ip-reflections types should show the same intensity profile with time. In contrast, a decoupled evolution of the intensity of the ip-reflections represents the concomitant formation of a columnar hexagonal or a lamellar phase.

The intensity of the oop-reflections is determined by integrating the area within the corresponding rectangle depicted in Figure 10a along q_z. In case of the ip-reflections, the area terminated by the second rectangle in Figure 10a was integrated along q_x starting from the calculated position of the primary beam at $q=0$ nm^{-1}. The integrated absolute intensities from ip- and oop-reflections are not comparable, since the ip-reflections are more or less obscured by the diffuse scattering of the AAM. The diffuse scattering was fitted and subtracted from the ip-reflection. It was found to be quite constant within one sample. However, the intensity of the diffuse scattering differs from sample to sample making it difficult to compare the absolute intensity values from different samples.

From the diffraction patterns depicted in Figure 10, it is generally possible to distinguish between ip-reflections corresponding to the hexagonal phases or the lamellar structure, because their d-values differ by a factor sin(120°). This is not possible for samples synthesized with P123, since their ip-reflections are superimposed by the diffuse scattering from the AAM and because they appear too close to the primary beam to be fully resolved. Additional transmission electron microscopy is needed to exclude the existence of a lamellar phase and to interpret the temporal evolution of the ip-reflections in case of the P123 samples.
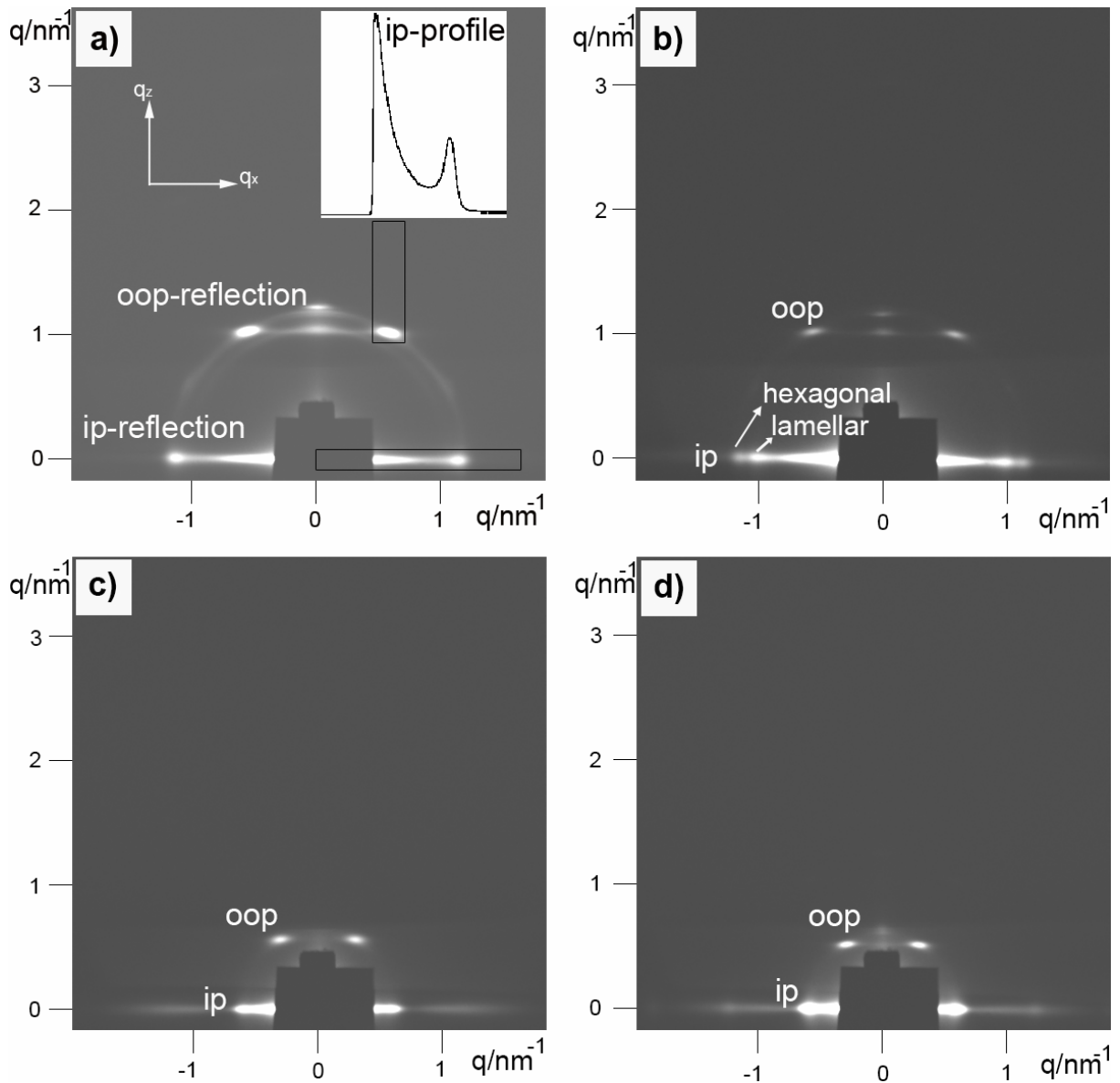
Figure 10: Representative GISAXS pattern of the samples
   a)   B-L-60% recorded after 170 minutes
   b)   B-H-60% recorded after 80 minutes
   c)   P-L-60% recorded after 115 minutes, and
   d)   P-H-60% recorded after 105 minutes.
The black rectangles mark the integrated areas for the determination of the ip and oop intensities. The intensity profile for the ip-reflection is given as inset in a). In pattern b) the ip-reflections corresponding to the circular lamellar phase can be distinguished from the ones corresponding to the hexagonal structures because of their different d-spacings. The intensity maxima cannot be separated when P123 is used as structure directing agent (GISAXS pattern d). But it is clear that the ip-reflections contain significantly more intensity than the oop-reflections.

3.3. Electron microscopy

3.3.1 Introduction to the method

The Transmission electron microscope allows us to investigate the inside of a sample due to the detection of transmitted electrons. It can be successfully used on samples thin enough to be penetrated by electrons. Thus, in most cases thinning of the samples in advance of the investigation is needed. One advantage of this technique is that high-resolution microscopy can be performed, due to the small wavelength of accelerated electrons, which is

$$\lambda = \frac{h\sqrt{\frac{1}{2}m_e}}{m_e\sqrt{eV}}$$ according to de Broglie[b]. Electrons that are accelerated with 200 kV therefore

have a wavelength of about 3 pm. However, the resolution of such microscope is limited to about 3-4 Å due to the imperfections of the lenses. Obviously, optical lenses cannot be used to focus the electron beam; the common circular magnetic lenses suffer from comparatively strong aberration and astigmatism.[14]

The lens system itself is rather complex; there are mainly three kinds of lenses. The condenser lens is focusing and aligning the electron beam before it meets the sample. The size of the illuminated area on the sample can be tuned with the condenser lens. The objective lens is most important and forms the first enlarged image of the sample. The defect coefficients of the objective lens are the limiting factors for the resolution of the microscope. The final magnification is reached with a set of projector lenses and a fluorescent phosphor screen is giving a visible picture of the transmitted electrons. The working principle of the objective lens is schematically shown in Figure 11.

---

[b] $\lambda = h/p = h/(m_e v)$
 $eV = \frac{1}{2}(m_e v^2)$, with m_e: mass of an electron, v: velocity, e: elementary charge, V: accelerating voltage
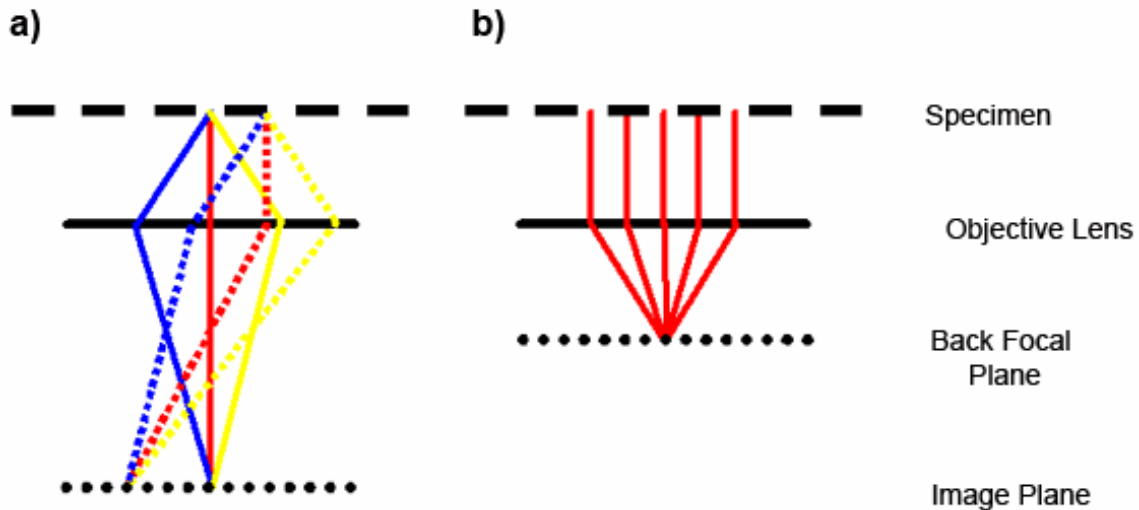
Figure 11: Schematic ray diagram illustrating the scattered electron rays focused on
      a) the image plane
      b) the back focal plane

The objective lens is positioned right after the specimen. Electron rays that are scattered at the same position within the sample (bold or dotted lines in Figure 11a) are focused on the same spot at the image plane through the objective lens even though they are scattered at different angles. The stronger the objective lens bends the electron rays, the farther away is the image plane from the objective lens and the larger is the magnification. It is also visible in Figure 11a that all rays scattered at the same angle (lines of the same color) are crossing at another plane more close to the objective lens no matter at which position within the sample they are scattered. This plane is called back focal plane and is shown in more detail in Figure 11b. If a crystalline sample is imaged, positive interference of the electron rays will occur only at distinct angles, analogous to X-ray diffraction. Thus, the back focal plane shows the electron diffraction pattern of the sample. When the microscope is working in the imaging mode, the image plane is displayed on the phosphor screen. When the microscope is working in the diffraction mode, the back focal plane is imaged.[14,15]

One of the advantages of electron microscopy is that an electron diffraction pattern can be obtained from very small crystals or a specific fraction of particles in a mixture of crystals. In

order to get the diffraction pattern of only the desired area and to prevent diffraction from more than one crystal, working with apertures is necessary. Schematic ray diagrams illustrating the image- and the back focal plane and the two apertures needed are shown in Figure 12.
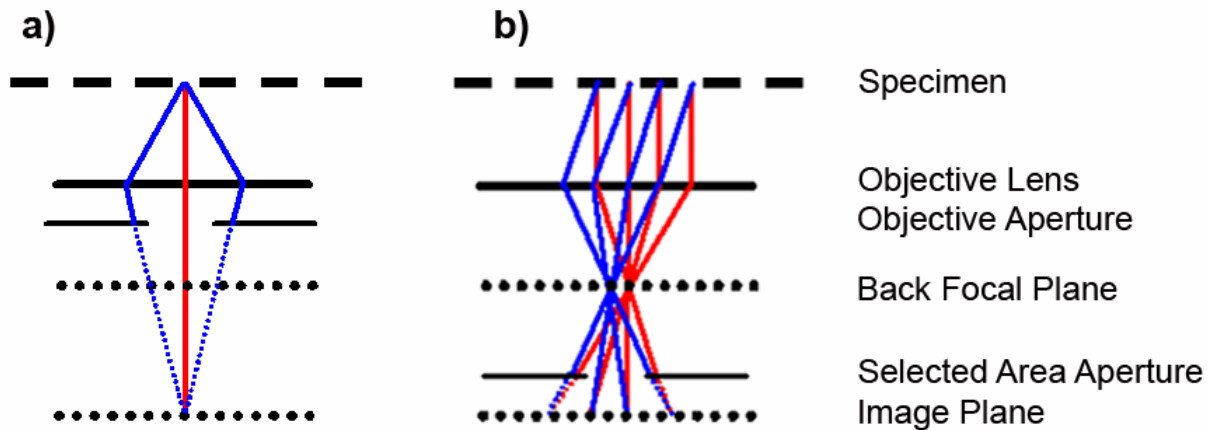
Figure 12: Schematic ray diagram illustrating the generation of both the back focal and the image plane as well as the working principle of
a) the objective aperture that filters electron rays scattered in a range of certain angles, and
b) the selected area aperture that filters electron rays scattered from a particular area.

The selected area aperture for diffraction is positioned right before the image plane. It filters electron rays originating from points within a particular area around the optical axis. A second aperture named objective aperture is positioned right after the objective lens and is used to filter electron rays that are scattered in a particular range of angles. Contrary to the selected area aperture, this aperture is used mostly in the imaging mode to obtain higher contrast. The third aperture used in TE microscopy is the condenser aperture, which sits above the specimen and additionally focuses the electron beam onto the sample.

Sometimes a measurement can be difficult since electrons strongly interact with matter. Mesostructured silica materials investigated for this thesis are comparatively sensitive to the electron beam. The samples can drift and move from their position due to charging, the structure can collapse due to irradiation with electrons, or the sample itself can decompose.[15]

Therefore, all samples were mounted on an additional conductive copper grid and measured with carefully adjusted size and brightness of the electron beam.

3.3.2. Description of the experiment

TEM images of films and composite membranes were obtained with a JEOL 2011 transmission electron microscope operating at 200 kV. Samples for electron microscopy were prepared by the following methods: (i) the alumina matrix was dissolved in phosphoric acid to release the embedded mesoporous silica; (ii) plan-views and cross-sections were prepared by dimple grinding, followed by Ar-ion polishing. For samples prepared as thin films on flat glass substrates, the mesostructured film was either prepared as cross-section or scratched off the substrate using a razor blade; the resulting mesophase powder was transferred onto a copper grid for TE microscopy. Membrane composites were mounted on a copper TEM grid prior to the measurement to prevent charging and/or destruction of the structure due to the electron beam.

When the composite membranes are viewed normal to the membrane surface (plan-view), the circular hexagonal and the lamellar structure look identical, as do cross-sectional views from the columnar hexagonal and the lamellar structure. However, lamellar structures tend to become instable when thinned and often collapse when irradiated with the electron beam. Thus, in most cases they can be distinguished by a comparatively high degree of distortion when imaged. Nevertheless, to truly confirm the existence of a lamellar phase, it is necessary to combine either the diffraction pattern with plan-view TEM images, or plan-view and cross-sectional micrographs.

3.4. Sorption experiments

Nitrogen sorption measurements were performed on Quantachrome Instruments NOVA 4000e and Autosorb-1 at 77 K. For calculations of pore sizes and volumes a NLDFT equilibrium model of N_2 on silica was used. A BET model was applied to evaluate the surface areas.

Sorption measurements can be performed under static or dynamic conditions. In a dynamic experiment the sample is mounted in a gas flow of inert and probe gas. The composition of the gas flow changes during adsorption or desorption; changes in the gas composition are measured, for example, as changes in the heat conductance of the gas mixture. This technique is a fast method to investigate the specific surface area of a sample. However, it is inappropriate for obtaining isotherms. In a static experiment the sample is mounted in a vacuum and distinct relative pressures (p/p_0, p_0 is the saturation pressure) of the probe gas are adjusted. Sorption is investigated either by measuring changes in the sample weight (gravimetric method) or by measuring the effective gas pressure above the sample in a volume-calibrated system (volumetric method). Thus, the adsorbed or desorbed gas volumes (in cm^3 (STP) per amount of sample in gram) are measured for every step p/p_0 and sorption isotherms are obtained.[16]

Sorption isotherms of microporous materials are typical Type I isotherms (Figure 13a). The micropores are filled at comparatively low relative pressure. With completion of the micropore adsorption the slope of the isotherm levels off and reaches a plateau. Non-porous materials most often follow the shape of a Type II isotherm (Figure 13b). Adsorption at low pressures is much less pronounced due to the lack of porosity; after monolayer adsorption, a second relatively steep part according to multilayer adsorption is observed. Mesoporous materials typically show Type IV isotherms (Figure 13c). After a steep increase at low

relative pressures due to the monolayer adsorption (and possibly additional microporosity of the samples), the slope levels off into the second part representing the multilayer adsorption followed by a steep increase of adsorbed gas volume due to capillary condensation within the mesopores at higher relative pressures.
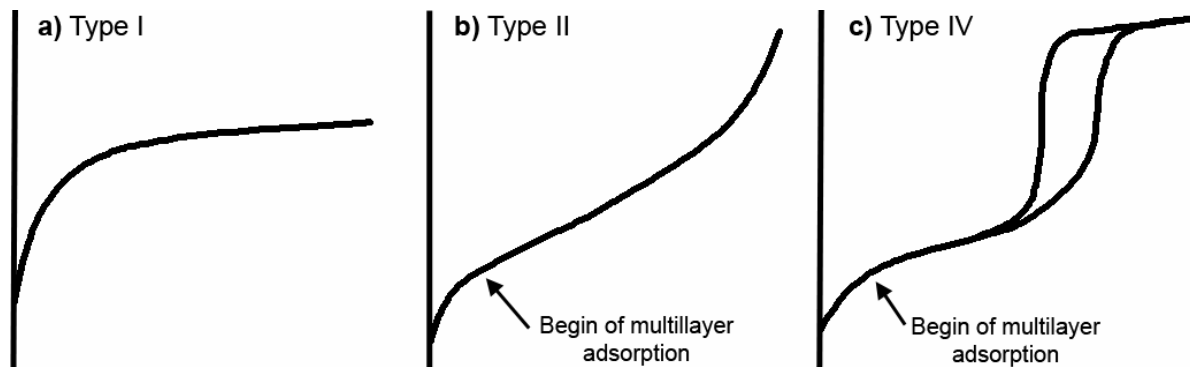
Figure 13: Typical shape of sorption isotherms
    a)   Type I (microporous material)
    b)   Type II (non-porous material)
    c)   Type IV (mesoporous material)

Most often, a hysteresis loop of the adsorption and desorption branch is observed in that range. The steeper the curve is in the capillary condensation regime, the narrower is the pore size distribution. While the desorption branch represents capillary condensation at equilibrium conditions, the capillary condensation is shifted to higher relative pressures in the adsorption branch due to kinetic effects (e.g., nucleation of droplets). Ideally, the slope of the capillary condensation is identical for the adsorption and desorption branch. However, the slope can be different, for example, if smaller pores are interconnected with bigger pores thus hindering desorption from the bigger pores (pore-blocking or cavitation). In this case the desorption branch does not anymore represent condensation at equilibrium conditions. After capillary condensation, a plateau is reached. The mesopore volume is calculated from that plateau. A BET (Brunnauer, Emmett, Teller) surface area[17] can be calculated from the shape of the isotherm prior to capillary condensation.

3.5. TGA measurements

Thermogravimetric analyses (TGA) of the bulk samples were performed on a Netzsch STA 440 C TG/DSC (heating rate of 10 K/min in a stream of synthetic air of about 25 mL/min). The sample weight was recorded as a function of temperature under controlled heating. In composite materials, the different components will be decomposed at different temperatures. Every step in weight loss corresponds to the combustion or desorption of one specific component and/or intermediates.

3.6. IR- and Raman spectroscopy

Raman spectra were recorded on a Jobin Yvon Horiba HR800 UV Raman microscope using a HeNe laser emitting at 632.8 nm. Infrared spectra were recorded on a Bruker Equinox 55s in transmission.

Raman- and Infrared spectroscopy are methods that probe the vibration modes of a sample. The infrared radiation induces vibrations within the molecules and thus, information about the local structure of molecules or materials is obtained. The moieties of a molecule such as a methyl group can be identified by their specific absorption bands in the infrared spectrum. A chemical group has to change its dipole moment during vibration in order to be detectable in infrared spectroscopy.

In Raman spectroscopy, vibrations of molecules are induced by energy transfer from incident light of higher energy, and the scattered light from the sample is analysed. The energy for the molecular movement is taken from the photons (Stokes-frequencies) or the energy of the movement is transmitted to the photons (Anti-Stokes frequencies), respectively. During vibration, the polarizability of the molecule has to change in order to observe Raman-active modes.

References

[1]   www.whatman.com/products/?pageID=7.57.293

[2]   D. Zhao, Q. Huo, J. Feng, B. F. Chmelka, G. D. Stucky, *J. Am. Chem. Soc.* **1998**, *120*, 6024-6036.

[3]   www.basf.com/businesses/chemicals/performance/pdfs/**Pluronic_P123**.pdf

[4]   D. Himsl, Forschungsbericht zum Praktikum in der Physikalischen Chemie an der LMU München **2006**.

[5]   M. von Laue, *Materiewellen und ihre Interferenzen*, Leipzig: Akademische Verlagsgesellschaft Becker und Erler, **1944**.

[6]   B. K. Vainshtein, *Fundamentals of Crystals*, Springer-Verlag, **1994**.

[7]   H. Schnablegger, Y. Singh, *A practical guide to SAXS*, Anton Paar GmbH Austria, **2006**.

[8]   M. Klotz, P.-A. Albouy, A. Ayral, C. Menager, D. Grosso, A. Van der Lee, V. Cabuil, F. Babonneau, C. Guizard, *Chem. Mater.* **2000**, *12*, 1721.

[9]   B. Smarsly, A. Gibaud, W. Ruland, D. Sturmayr, C. J. Brinker, *Langmuir* **2005**, *21*, 3858.

[10]   S. Zimdars, Forschungsbericht zum Praktikum in der Physikalischen Chemie an der LMU München **2007**.

[11]   F. Marlow, I. Leike, C. Weidenthaler, C. W. Lehmann, U. Wilczok, *Adv. Mater.* **2001**, *13*, 307.

[12]   D.-M. Smilgies, P. Busch, D. Posselt, C. M. Papadakis, *Synchrotron Radiation News* **2002**, *15(5)*, 35.

[13]   D.A. Doshi, A. Gibaud, V. Goletto, M. Lu, H. Gerung, B. Ocko, S. M. Han, C. J. Brinker, *J. Am. Chem. Soc.* **2003**, *125*, 11646.

[14]   D. B. Williams, C. B. Carter, *Transmission Electron Microscopy*, New York, **1996**.

[15] O. Terasaki, T. Ohsuna, *Handbook of Zeolite Science and Technology*, New York, **2003**
      291.

[16] K. S. W. Sing, D. H. Everett, R. A. W. Haul, L. Moscou, R. A. Pierotti, J. Rouquerol,
      T. Siemieniewska, *Pure Appl. Chem.* **1985**, *57*, 603.

[17] S. Brunauer, P. H. Emmett, E. Teller, *J. Am. Chem. Soc.* **1938**, *60*, 309.

III. Results and Discussion

1. Characterization of the AAMs

The commercially available AAMs used in this work (47 mm, Anodisc[TM], Whatman) were characterized using X-Ray diffraction, electron microscopy, thermogravimetric analysis, and Infrared- and Raman spectroscopy. Nowadays there is general agreement on the amorphous character of porous anodic alumina.[1,2] As expected, this is supported by the X-ray diffraction pattern of an AAM depicted in Figure 1.1 a. However, a minor increase of intensity is observed at 34 2θ indicating some limited degree of order.

The regular porosity and vertical alignment of the channels was observed in scanning electron microscopy images (see Chapter II, Section 1). However, the pore diameters were not around 20 nm as claimed by the company but mainly in the range of 150-300 nm. Moreover, transmission electron micrographs were taken of various composite samples, showing the shape, size, and arrangement of the AAM channels as well as the two aluminum oxide layers making up the AAM.[3] A representative example is depicted in Figure 1.1 b. The inner oxide layer is dark in the TEM picture and surrounded by the brighter outer oxide layer. It is known that the outer oxide layer is contaminated with anions from the electrolyte and that it is less dense than pure alumina. The AAM channels have various diameters and shapes. In some cases, initially separated channels seem to be grown together (Figure 1.1 b, center).
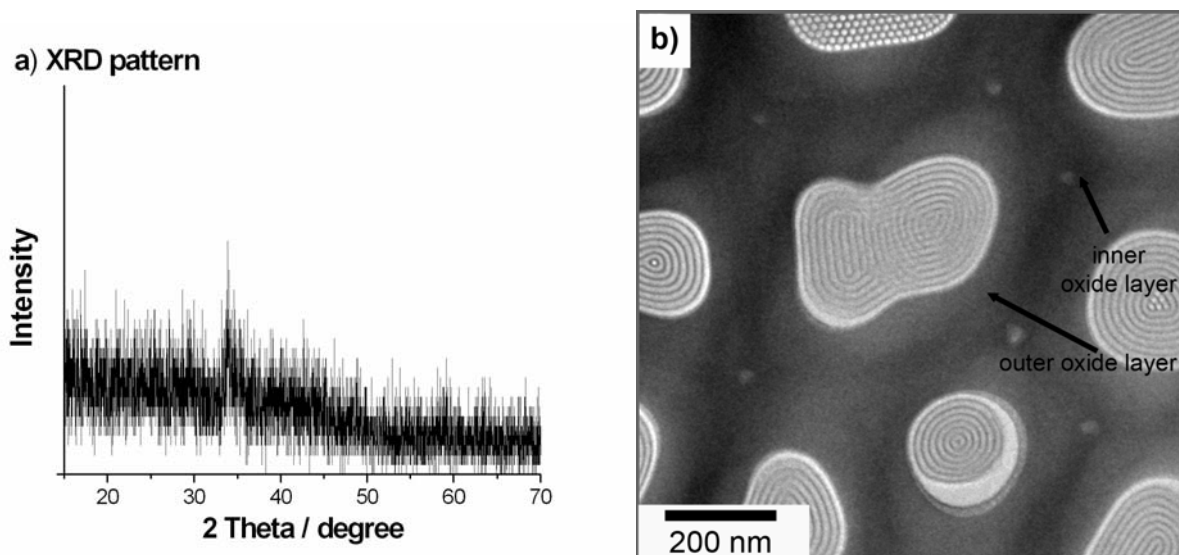
Figure 1.1: a) Diffraction pattern of an AAM showing the amorphous character of the alumina.
b) TEM image of a composite membrane. AAM channels with various shape and diameters are shown. Two oxide layers are visible as darker and brighter areas of the alumina matrix.

Thermogravimetric analysis was performed on a pure AAM (Figure 1.2 a, d) and an AAM that was annealed at 800 °C for 7 h. In the pure AAM, the weight loss proceeds in three steps. The first step is probably due to the loss of adsorbed water, starting shortly above 100 °C and being endothermic according to the DSC curve. The second, exothermic step between 200-400 °C is assumed to be due to condensation of Al-OH species in the outer oxide layer. The weight loss curve shows a small third step above 700 °C that is correlated with a strong exothermic process according to DSC. This is interpreted as a phase transformation accompanied by further condensation of OH groups. It is known from the literature that low temperature alumina phases loose water upon thermal treatment until complete dehydroxylation produces α-alumina.[4] The overall weight loss in that sample is 0.32 weight % due to OH condensation.

The weight loss and DSC curves of the AAM annealed at 800 °C follows the same shape as the curves of the untreated AAM until 200 °C. The second step according to OH condensation is missing; little weight loss is observed above 700 °C. In general, the data appear noisy due to the little overall weight loss in this sample. The DSC data does not show a pronounced

exothermic peak indicative for phase transformation. It is concluded that annealing at 800 °C

is sufficient to remove incorporated OH groups from the outer aluminum oxide layer.
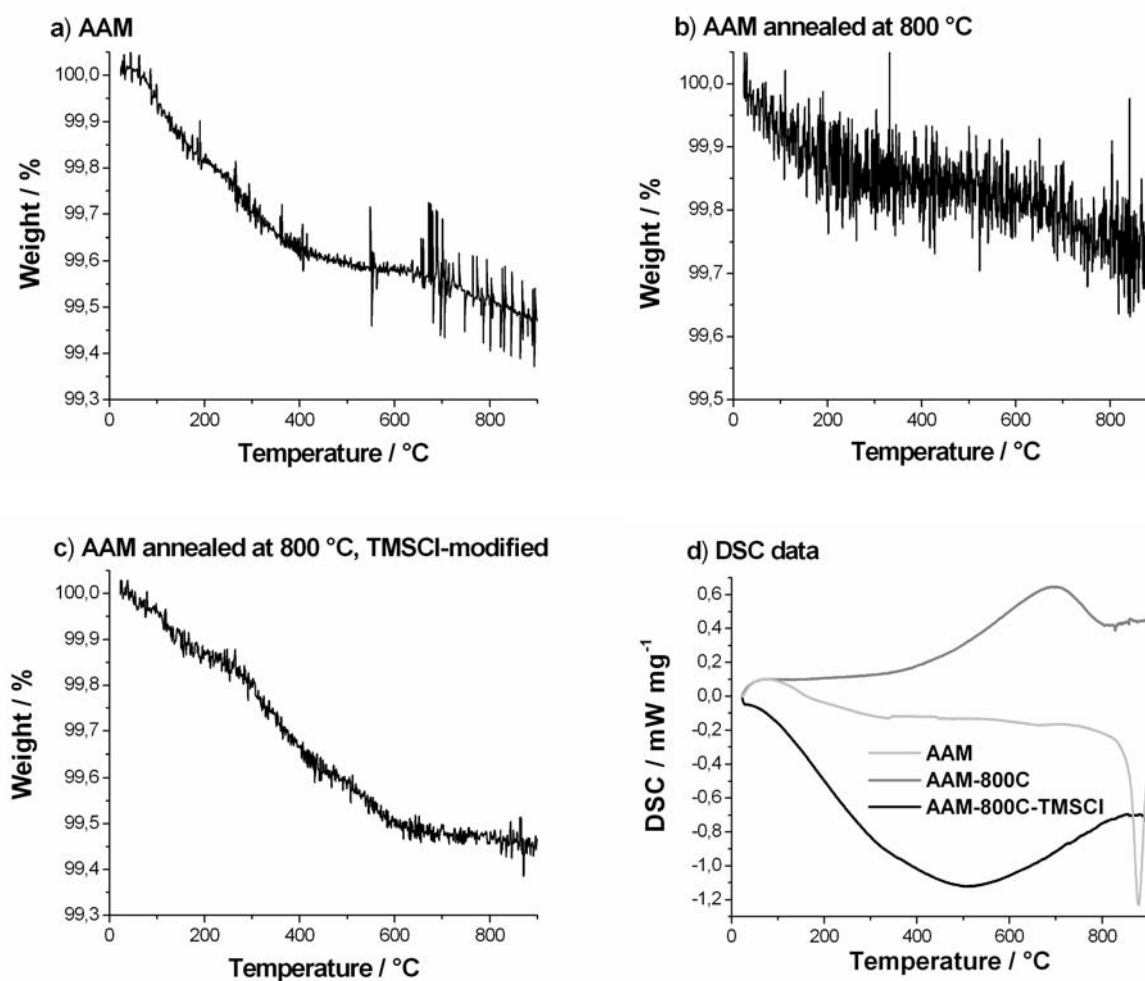
Figure 1.2: a)-c): TGA data of an untreated AAM [a)], and AAM annealed at 800 °C for 7 h [b)], and
annealed AAM additionally modified with TMSCl [c)]
d): Corresponding DSC curves

In another experiment, AAMs were hydrophobized by modification with trimethyl-

chlorosilane (compare Chapter III, Section 6). Previous to modification, some AAMs were

annealed at 800 °C, in order to obtain interpretable TGA data that are not superimposed by

possible weight loss from OH group condensation (Figure 1.2 c). The exothermic weight loss

at 100-600 °C is interpreted solely as loss of methyl groups. As expected for an AAM

annealed at high temperature, no weight loss or phase transformation is observed above

700 °C. The overall weight loss of the modified sample is 0.41 weight % due to CH_3

decomposition.
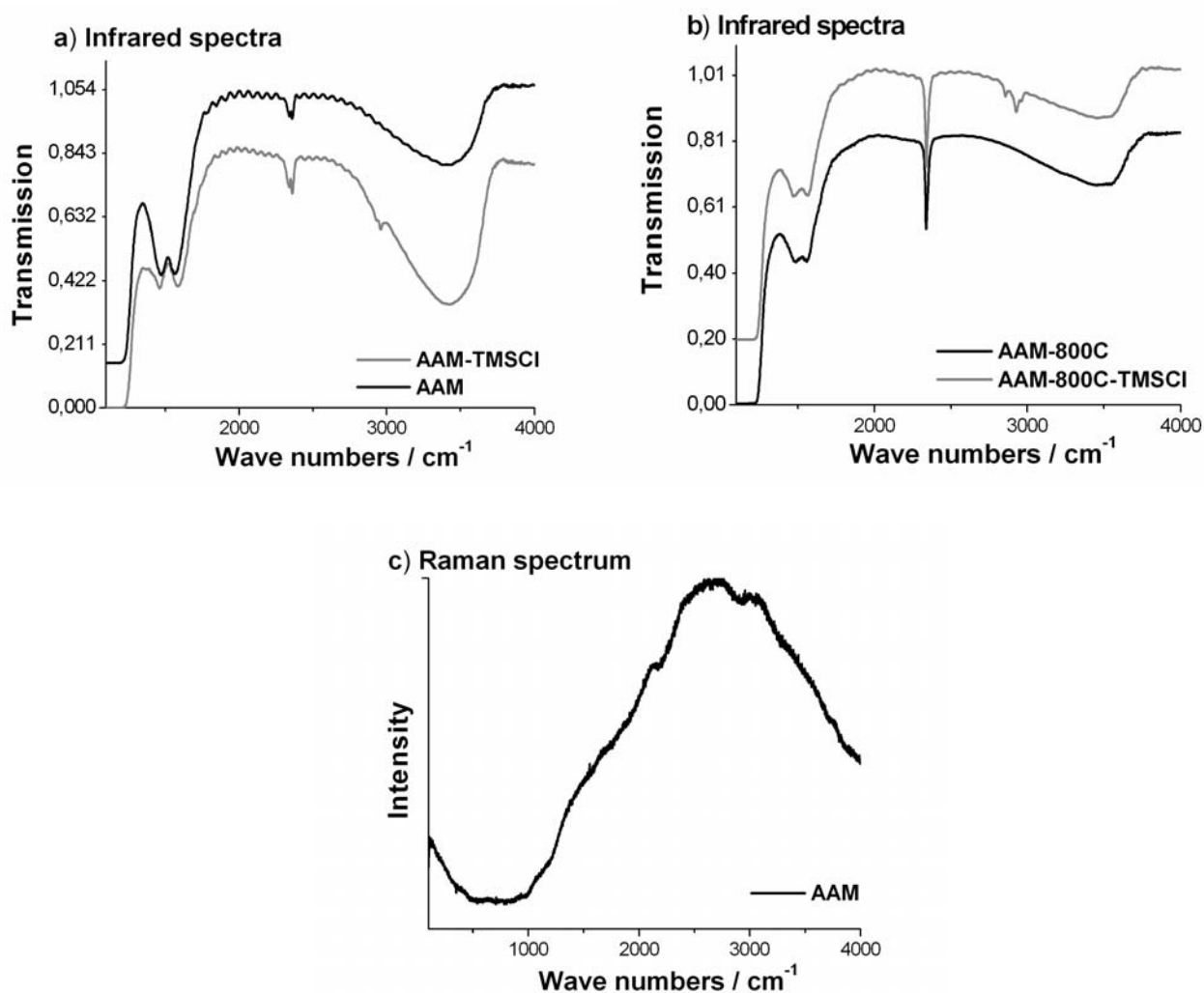
Figure 1.3: a) Infrared spectra of modified and not modified AAM
b) Infrared spectra of previously annealed modified and not modified AAM
c) Raman spectrum of untreated AAM

Transmission infrared spectra were obtained from modified and unmodified AAMs annealed and not annealed at 800 °C, respectively. The alumina membranes give interpretable data in the range of 3500-1200 cm^{-1}, but they are not transparent at wavenumbers below 1200 cm^{-1} (Figure 1.3 a, b). At 3500 cm^{-1}, a broad absorption band is visible, coming from the OH groups present in the outer oxide layer and adsorbed water from the ambient air. This broad band is less pronounced in annealed membranes, most probably due to the absence of framework OH-groups in these samples. The sharp absorption bands at 2300 cm^{-1} are from gaseous CO_2 present in the atmosphere during the measurements. Two peaks were recorded at 1460 cm^{-1} and 1570 cm^{-1} that have been previously observed but not discussed in

commercially available AAMs[5]. As already discussed in section 1.3, these bands might originate from AlO(OH) ring stretching vibrations similar to those observed in boehmite.[6,7] Interestingly, these bands are present as well in annealed samples that most probably have already transformed to pure alumina. However, these bands might as well be correlated with other ions from the electrolyte e.g. phosphate ions that were incorporated into the framework during anodization.

The additional band corresponding to a CH_3 vibration at 2950 cm^{-1} in modified samples is less pronounced and superimposed by the broad water band in not annealed membranes, but it is clearly visible in annealed and modified samples. Raman spectroscopy avoids superposition with the broad band coming from water or OH-groups. Nevertheless, the Raman spectrum of an unmodified not annealed AAM shown in Figure 1.3 c shows high self-fluorescence of the AAM in the relevant energy range. Additional absorption bands in modified AAMs were not visible in the Raman spectra. However, the modification is verified by infrared and TGA data and moreover was observed to have a pronounced effect on the self-assembly of the mesostructured silica (compare Chapter III, Section 6).

2. Tuning the structure and orientation of ordered mesostructures inside the channels of anodic alumina membranes

In this chapter, a synthesis of mesostructured silica within the channels of AAMs will be presented, using the ionic surfactant CTAB as well as the non-ionic Brij 56 or Pluronic P123 as structure directing agents and the EISA method. The influence of different surfactant:silica ratios as well as the humidity during the solvent evaporation will be discussed. The samples were characterized with 2D SAXS and TEM, giving the option to estimate the ratio of the different structures that were formed even in phase mixtures by calculating the ratio of the intensities of the oop- by the ip-reflections (see Chapter II, Section 3.1). While a pure circular hexagonal structure will have ip- and oop-reflections of roughly the same intensity in the diffraction pattern (oop:ip=1), a pure columnar hexagonal or a circular lamellar phase will result in only the ip-reflections (oop:ip=0).

2.1. Ionic CTAB

A pure columnar hexagonal phase was observed for the two CTAB-templated samples having different surfactant concentrations shown in Figure 2.1 a. This is indicated by the absence of oop-reflections in the corresponding diffraction patterns (Figure 2.1 a). Additionally, the hexagonal arrangement of the silica rods was directly observed in the representative plan-view TEM images shown in Figure 2.1 b. For the CTAB-2 sample, almost all of the pores of the alumina membrane (about 90%) were filled with fully mesostructured material. The power spectrum (inset in Figure 2.1 b) calculated from the corresponding TEM image showed well-ordered hexagonal mesophase structure with a d-spacing of about 4.5 nm which corresponds to the spacing observed for CTAB-templated mesoporous powders, e.g., MCM-41-type materials.[8]
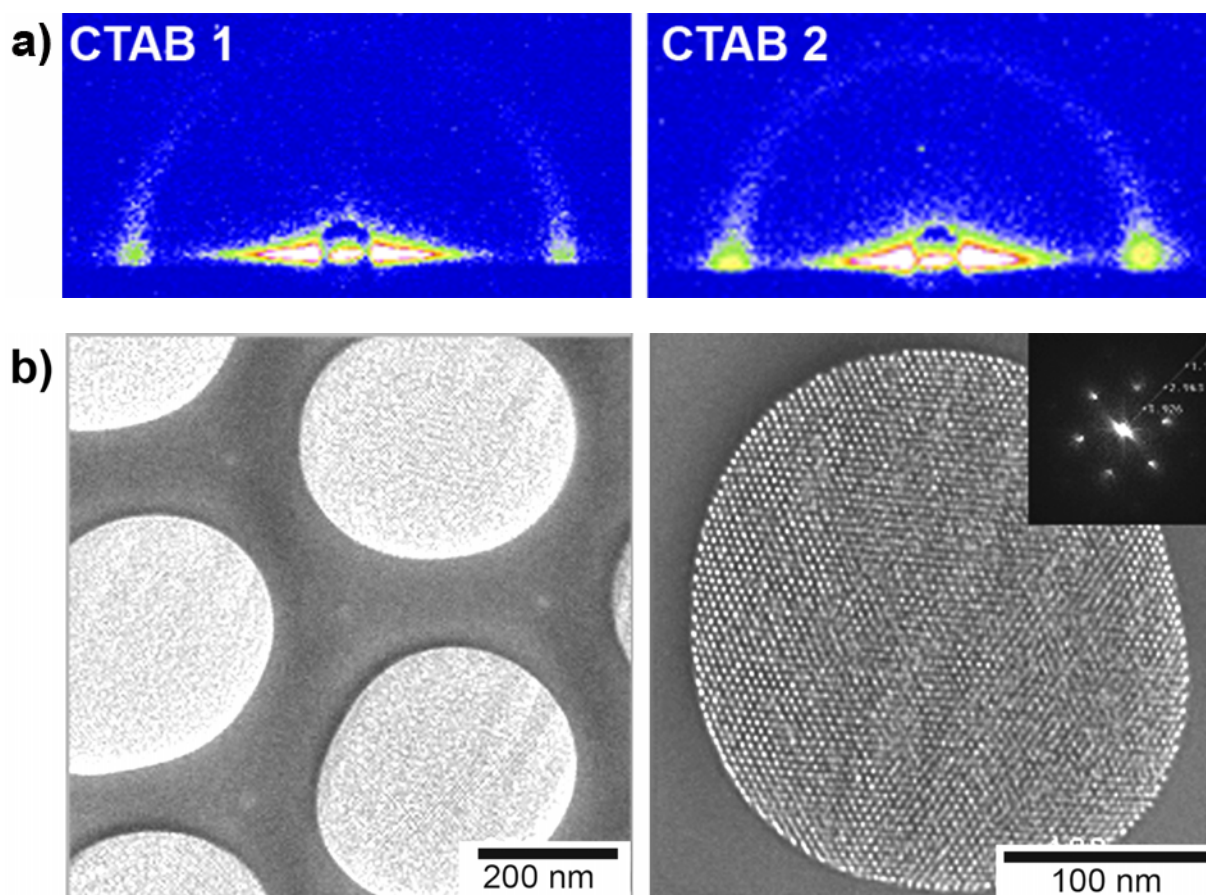
Figure 2.1:
a) GI-SAXS patterns of the samples CTAB-1, CTAB-2 (at different surfactant concentrations)
b) Plan-view TEM images of sample CTAB-2 showing the columnar oriented hexagonal mesostructure
(insert: 2D power spectrum)

It was observed that with the decrease of the surfactant concentration in the deposition mixtures (sample CTAB-1, Figure 2.1 a), the intensity of the diffraction spots in the SAXS patterns decreases (Table 2.1). This may be due to the decreased density of the ordered mesostructured domains in the alumina matrix. The corresponding TEM images show that in this sample almost 30% of the alumina pores were either empty or showed inferior hexagonal order. The observed results suggest that direct control over the ordering process (formation of the lyotropic liquid-crystalline mesophase) can be achieved by changing the surfactant concentrations in the deposition mixtures.

Table 2.1: Summary of SAXS data of CTAB-templated mesoporous channel systems.

Sample name	Surfactant/Silica molar ratio	Diffraction spots detected	Relative intensity (a.u.)[a]	d-spacing /nm[b]
CTAB 1	0.18	ip-reflections	0.14	4.5
CTAB 2	0.26	ip-reflections	0.19	4.3
[a] The intensity of the reflections was normalized to the intensity of the primary beam after the semitransparent beamstop. [b] The d-spacings were calculated from the position of the diffraction spots according to q = 2π/d.				

2.2. Non-ionic surfactants (Brij 56 and Pluronic P123)

The other mesophase configuration (having circular mesopores) was realized in this work by using P123 or Brij56 as structure directing agents. With these samples four well-resolved diffraction spots were recorded coming from both out-of-plane and in-plane reflections. It should be mentioned that the circular hexagonal structure was not observed if CTAB was used as structure directing agent. This might be due to the fact that CTAB is an ionic template and therefore interacts differently with the silica-precursors and the AAM-surface.

In the following it is shown that the mesophase structure of the AAM-embedded Pluronic123 and Brij56 templated material can be tuned by varying the amount of surfactant in the deposition mixtures or by adjusting the humidity during the drying process. The oop:ip intensity ratios for the Pluronic123- as well as for the Brij56-templated silica material in the AAMs are shown in Table 2.2. The corresponding SAXS patterns of the mesophase structures prepared in the channels of the AAMs with deposition solutions containing increasing amounts of template and being synthesized at different humidity are shown in Figure 2.2.

Figure 2.2:
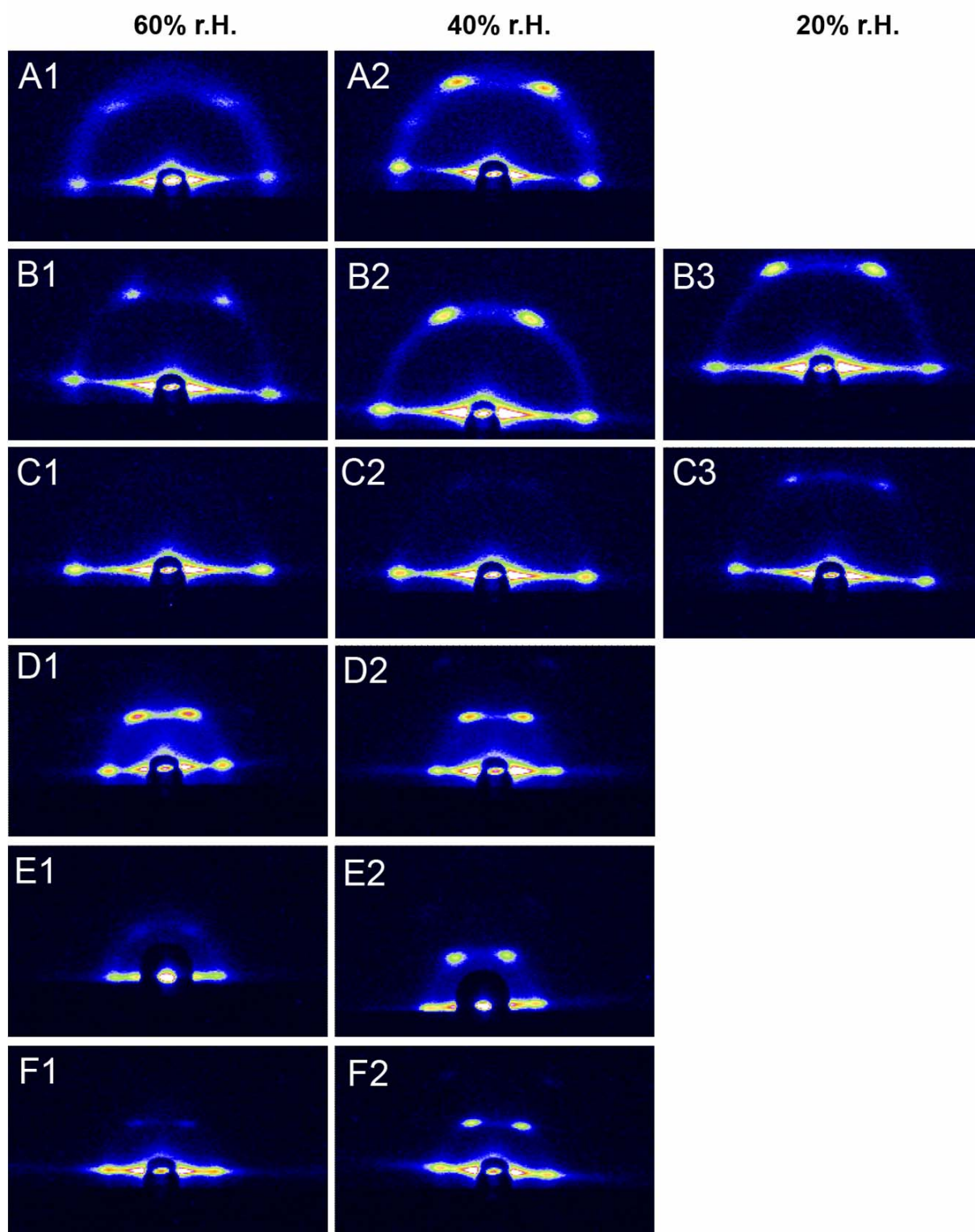of samples A1-A2, B1 - B3, and C1 - C3, reacted at different humidities (Brij56 templated, A, B and C synthesized with different surfactant concentrations, respectively), and of samples D1, D2, E1, E2, F1, and F2 reacted at different humidities (P123 templated, D, E, and F synthesized with different surfactant concentrations, respectively – see text)
(Same spatial and intensity scales for all images).

Table 2.2: Summary of SAXS data of block-copolymer-templated mesoporous channel systems.

Sample name	Surfactant:Silica molar ratio	Relative integrated intensities of diffraction spots, (oop:ip)			d-spacings /nm [a]
		60% humidity	40% humidity	20% humidity	
A1-A3	Brij56/Si = 0.063	0.4	1.2	[b]	A1: 6.54 A2: 6.4
B1 - B3	Brij56/Si = 0.133	0.4	0.6	1.1	B1: 6.2 B2: 6.0 B3: 5.8
C1 - C3	Brij56/Si = 0.265	0	0.05	0.2	All: 6.4
D1 – D2	P123/Si = 0.013	1.1	1.2	[b]	All: 11.0
E1 – E2	P123/Si = 0.014	0.1	0.5	[b]	All: 11.7
F1-F2	P123/Si = 0.017	0.01	0.25	[b]	All: 11.5
[a] The d-spacings were calculated from the position of the diffraction spots according to q = 2π/d. [b] no structure detected					

It is striking that increasing the concentration of surfactant in the deposition mixtures and synthesis at high humidity generally leads to a decreased oop:ip ratio. The oop:ip ratio of the samples synthesized with Brij 56 at 40% relative humidity was decreased from 1.1 (pure circular hexagonal phase) to 0.75 by increasing the surfactant: silica ratio from 0.063 to 0.133 (A2, B2). Additionally, the oop:ip ratio is decreased from 1 to 0.5 when the humidity was changed from 20% to 60% (B1, B3). Plan-view TEM images of the sample B1 (oop:ip ratio of 0.5) show an equal distribution of circular and columnar hexagonal structures. The TE-micrograph depicted in Figure 2.3 b shows an AAM channel filled with mesostructured material with solely columnar orientation. Besides the co-existence of the circular and columnar mesopores in different channels of the AAMs "twinned" structures showing both configurations in one AAM-channel are observed (Figure 2.3 a). Therefore we conclude that the oop:ip ratio of A1-A3 and B1-B3 directly reflects the distribution of the circular and the columnar hexagonal mesophases in the respective samples.

It was observed that the drying of the composite material (between three to five hours), takes longer at higher humidity or with higher surfactant concentration. Therefore it is suggested that a minor difference in energy should exist between both orientations, and with longer

74

synthesis time the reaction is driven towards the thermodynamically more stable state, which

would be the vertical, columnar mesopore alignment.
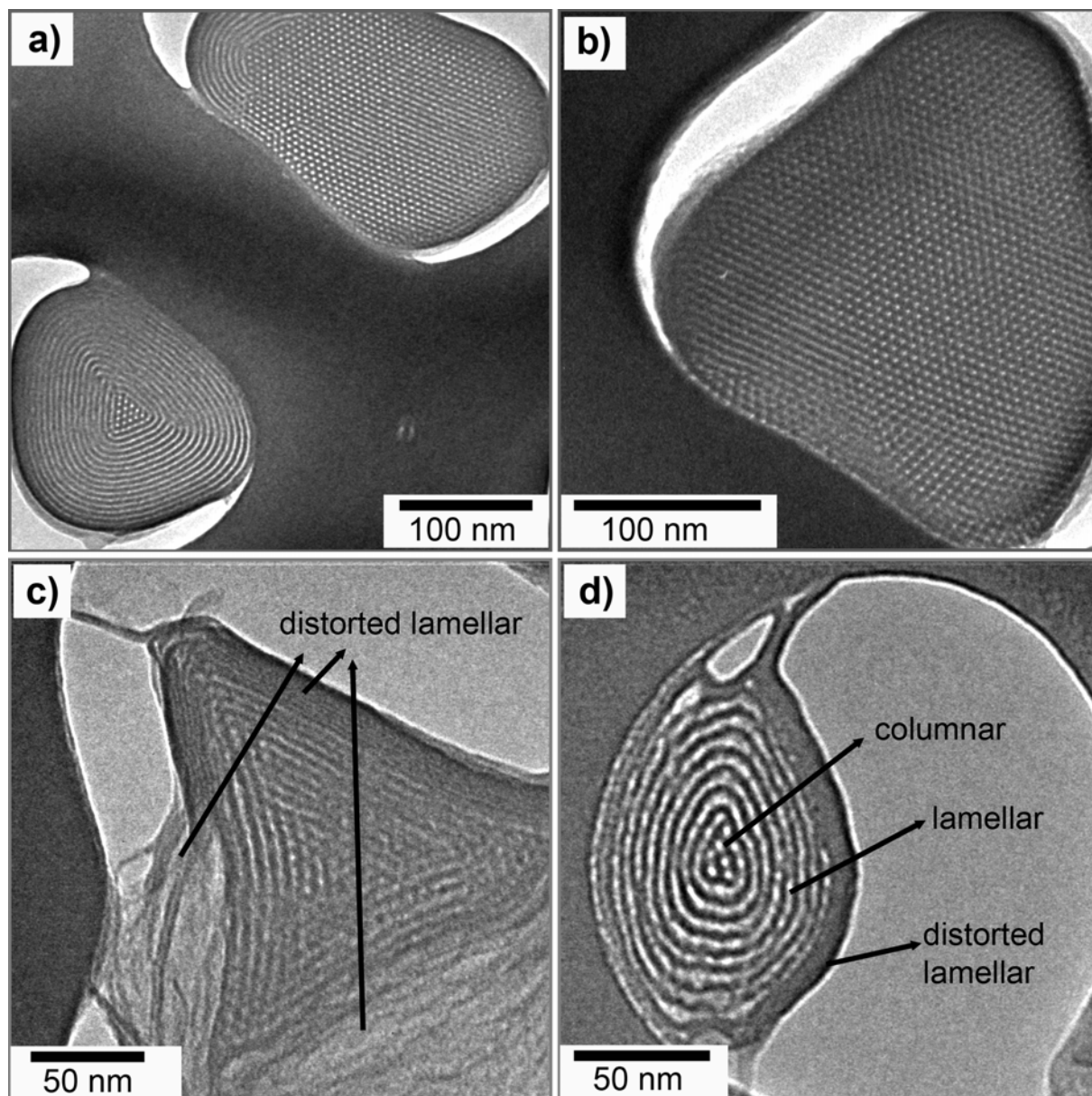
Figure 2.3: Plan-view TEM images of
a), b) sample B1 (Brij56 templated, 60% r.H.) with approximately equal distribution of columnar and circular mesophases.
c), d) sample C2 (Brij 56 templated, 40% r.H.) with a mixture of the columnar hexagonal and the circular lamellar structures. There are areas where the lamellar phase is collapsing upon irradiation with the electron beam.

Further increase of the Brij 56 **:** silica ratio led to the formation of a lamellar phase before

samples with a pure columnar mesostructure could be synthesized. This is concluded from the

absence of oop reflections in the diffraction patterns and corresponding TEM images showing many areas with a circular geometry (compare Chapter II, Section 3.1). TEM images of sample C2 (oop:ip ratio of 0.03) are given in Figures 2.3 c, and d as examples. Besides areas with a columnar arrangement of the silica mesophase, areas with a circular arrangement of silica sheets are observed. The circular lamellar phase can be distinguished from a circular hexagonal structure since it is typically collapsing in the electron beam of the TEM. The representative image in Figure 2.3 c shows the distorted lamellar phase. In some areas the silica sheets lay directly besides each other because the template is destroyed by the electron beam (Figure 2.3 c, upper edge of the mesophase-triangle). This can also lead to the complete destruction of the sheet-like geometry (Figure 2.3 c, lower right corner). There are also few areas where the lamellar phase shows only slight distortion (Figure 2.3 d). In the TEM images it is observed that in general, the smaller the diameter of the respective sheets, the more stable is the structure.

Samples synthesized with Pluronic P123 show in principal the same behavior than samples synthesized with Brij 56. However, no structure was detected when the samples were synthesized at 20% relative humidity. The oop:ip ratio is decreased from 0.7 to 0.1 when the humidity during the EISA process is increased from 40% to 60% (samples E1, E2) and it is decreased from 1.0 to 0.7 when the P123:silica ratio is increased from 0.013 to 0.014. Samples with predominantly lamellar phase were obtained when the P123:silica ratio was further increased to 0.017 (samples F1-F2). Representative TEM images of the samples D1, D2, E2, and F2 are depicted in Figure 2.4.
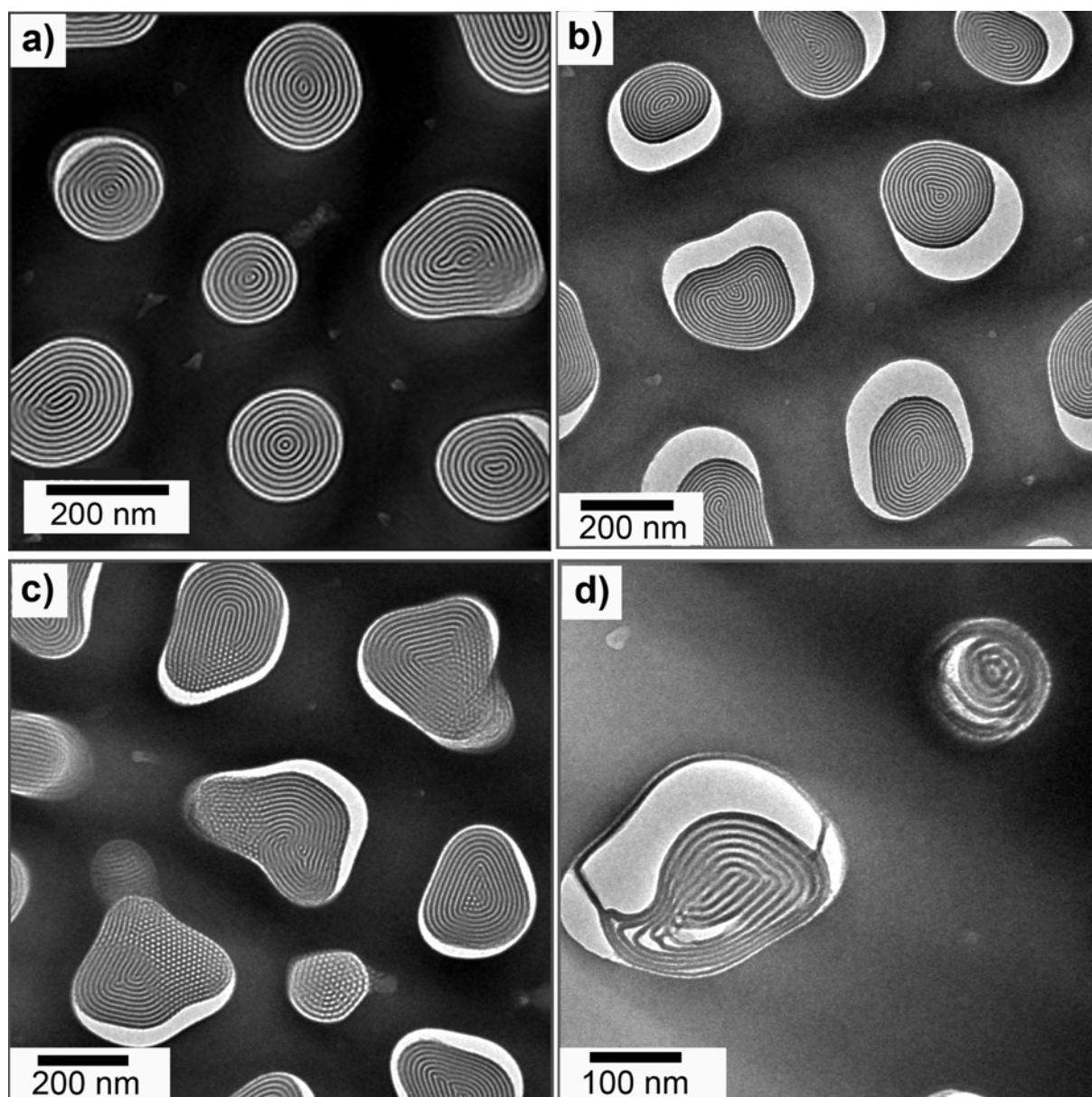
Figure 2.4: Plan-view TEM images of
a) sample D1 (P123 templated, 60% r.H.) with predominantly circular orientation,
b) sample D2 (P123 templated, 40% r.H) with circular hexagonal phase,
c) sample E2 (P123 templated, 40% r.H.) with circular and columnar phase mixture (oop:ip ratio of 0.7),
d) sample F2 (P123 templated, 40% r.H.) with a mixture of circular, columnar and lamellar phases (oop:ip ratio of 0.3).

The TEM images from the samples D1 and D2 synthesized with a P123:silica ratio of 0.013 at 60% and 40% humidity, respectively show only a circular arrangement of the silica rods (Figure 2.4 a, b). This corresponds to the oop:ip ratios of 1 calculated from the diffraction patterns for both samples. A mixture of the circular and columnar orientation is observed in sample E2, having a respective oop:ip ratio of 0.7 (Figure 2.4 c). A predominantly tubular

lamellar phase was found in sample F2 having an oop:ip ratio of 0.3 (Figure 2.4 d). The distortion of the lamellar structure upon electron beam irradiation is also observed in this sample. A cross-section image of F1 is shown in Figure 2.5. It depicts a mesoporous fiber coming out of an AAM channel at a site of fracture. The circular arrangement of the sheets is visible as well as the line pattern when viewing the lamellar structure from the side.
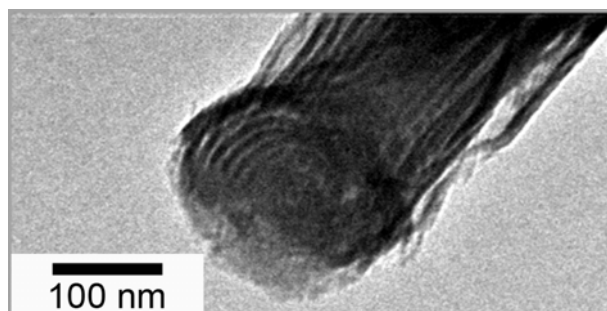
Figure 2.5: Cross-section TEM-Image of sample F1 (P123 templated, 60% r.H.) showing a mesoporous fibre with lamellar structure coming out of the AAM-channels at a site of fracture.

2.3. Sample preparation

The deposition mixtures were prepared by applying a two step synthesis procedure. First, 2.08 g (0.01 mol) tetraethyl orthosilicate (TEOS, Aldrich) was mixed with 3 g 0.2 M HCl, 1.8 g H_2O and 5 mL EtOH and heated at 60 ^{o}C for 1h to accomplish acid-catalyzed hydrolysis-condensation of the silica precursor. For the preparation of CTAB-containing deposition mixtures this solution was mixed with 0.644 g (1.77 mmol) or 0.947 g (2.6 mmol) CTAB dissolved in 10 ml EtOH, respectively (samples CTAB-1 and CTAB-2). The Brij56 containing samples were prepared using 0.453 g (0.63 mmol) Brij56 dissolved in 7.5 ml ethanol, 0.906 g (1.33 mmol) Brij56 dissolved in 15 ml ethanol, or 1.81 g (2.65 mmol) Brij56 dissolved in 30 ml ethanol, respectively (samples B1 - B3 and C1 - C3). For the preparation of the Pluronic123-containing solutions the pre-hydrolyzed silica was mixed with 15 ml (0.13 mmol P123), 16,25 ml (0.14 mmol), or 20 ml (0.17 mmol P123) 5 wt% ethanol solutions of Pluronic123 (sample D1 - D3, E1 - E3, respectively). The AAMs (47 mm, Anodisc^{TM}, Whatman) with average pore diameters of 120-200 nm and thickness of

approximately 60 µm were soaked with the prepared precursor mixtures by distributing 0.75 ml over the whole membrane surface. After 3-5 hours at room temperature and under controlled humidity the membrane appeared dry and homogeneously filled with the synthetic mixture.

3. *In situ* GISAXS study of the formation of mesostructured phases within the pores of anodic alumina membranes – different templates

The formation of different structure types in mesoporous films or powders has been well studied in the past. However, the existence of the two different orientations (circular or columnar) of one and the same structure has not been observed in films on flat substrates and is related to the unique confined geometry of the porous substrate investigated here. The energetic difference between the circular and the columnar hexagonal structure seems to be quite small, since the production of pure phases remains a challenge. The formation mechanism of the two orientations is unknown, and until now no information could be obtained whether or not both orientations are equally formed from the beginning of the reaction or if one phase is developed *via* conversion of the other phase. A detailed understanding of how the mesostructured material is formed inside the AAM channels will provide us with greater control over the structure and orientation of the synthesized products and hence the adaptation of the system for future applications. In this chapter an *in situ* grazing incidence small-angle X-ray scattering (GISAXS) study is presented, aimed at a detailed understanding of the formation process of the mesostructured material inside the confined environment of the AAM-channels. This is the first time that the formation of structured material within the ordered pores of a substrate was investigated by *in situ* diffraction.

3.1. General

Three different systems have been investigated, using either the ionic surfactant CTAB, the non-ionic triblock copolymer Pluronic P123, or the non-ionic diblock copolymer Brij 56 as structure directing agents. An overview of the observed structures inside the AAM channels and their respective diffraction patterns in the given diffraction geometry is depicted in

Chapter II, Section 3.1. The temporal evolution of the integrated intensities of the oop- and ip-reflections corresponding to the structures inside the AAM-channels was analyzed for each sample (see Chapter II, Section 3.2). When a circular hexagonal phase is forming, the time-dependent intensity curves of the oop- and the ip-reflections types should have the same shape. A decoupled evolution of the intensity of the ip-reflections represents the formation of a columnar hexagonal or lamellar phase. Furthermore, the weight-loss related to the evaporation of the solvent as a function of time is displayed in Figure 3.1 d.
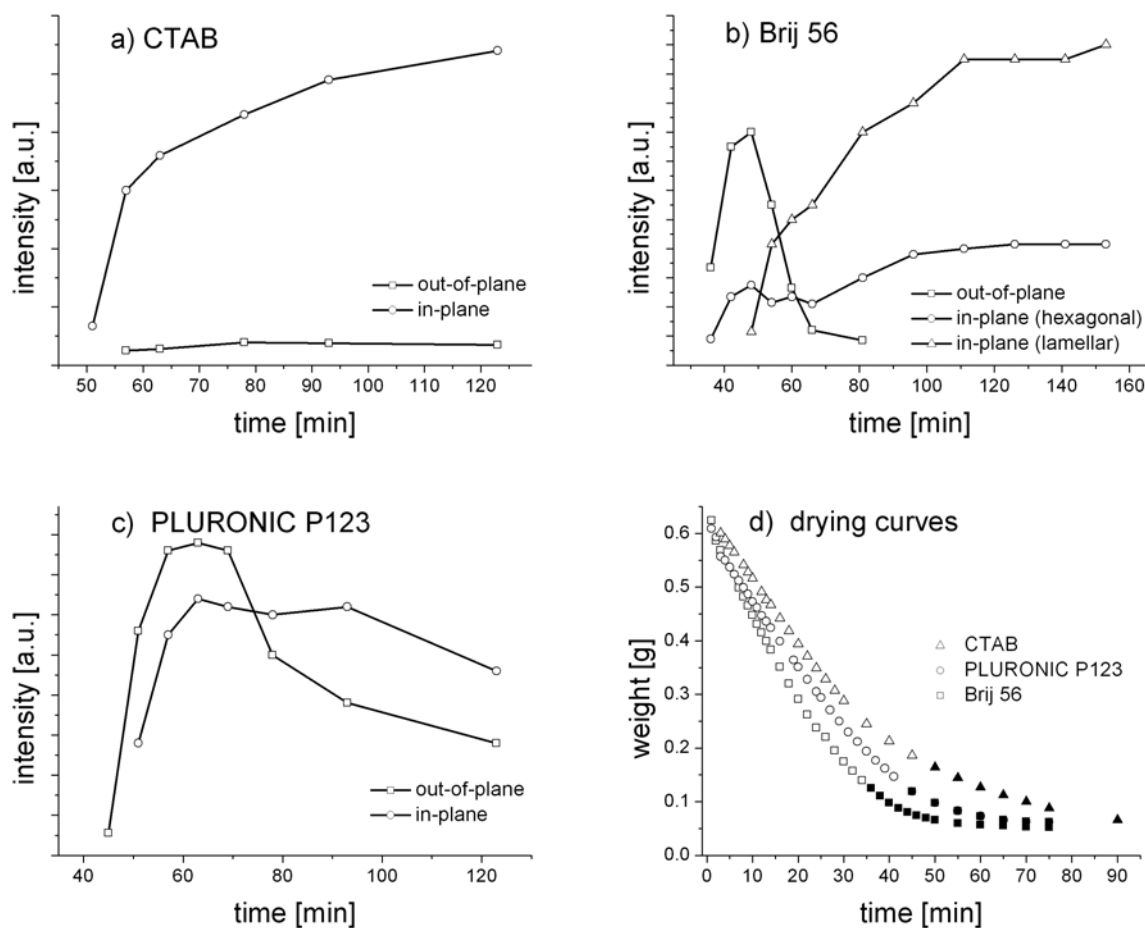
Figure 3.1: Intensity of the ip- and oop-diffraction spots plotted versus time for the samples synthesized
   a) with CTAB,
   b) Brij 56, and
   c) Pluronic P123 as structure directing agents.
   d) The weight loss for each sample is plotted versus time. Mesostructure was observed during the time period indicated by filled symbols.
The diffraction patterns of the sample synthesized with Brij 56 (b) show two distinguishable in-plane reflections assigned to the hexagonal and the lamellar phase.

3.2. Ionic CTAB

Using CTAB as an ionic surfactant, intrachannel mesostructure was generated within 50 minutes, when most of the solvent had already evaporated and the critical micelle concentration was exceeded (Figure 3.1 a, d). The intensity of the in-plane reflections increases strongly within the following ten minutes, reflecting increasing order of the structure. In the following period, the slope levels off, almost reaching a plateau after 100 minutes. At this time, the sample has almost reached its final weight suggesting that solvent evaporation is mostly completed. The intensity of out-of-plane reflections is extremely weak, leading to the conclusion that no significant amount of the circular hexagonal phase has been formed. TEM images confirm that the main phase is columnar hexagonal (Figure 3.2 d).

These results allow a better understanding of the formation mechanism of the mesostructure within the anodic alumina membrane pores. In a recent article the formation of this hexagonal structure in the direct vicinity of the pore wall was ascribed to the adsorption of cationic CTA to the alumina wall.[9] Due to this adsorption the hexagonal structure was supposed to form even before the critical micelle concentration (CMC) is reached within the entire pore. However, as demonstrated in our present study, the formation of structure starts very late in the evaporation process. Therefore we propose that the CMC is reached first, followed by structure formation in the vicinity of the alumina wall which acts as heterogeneous nucleation center. From there the structure formation into the center of the pore continues rapidly leading to the highly ordered hexagonal structure as depicted in the TEM in Figure 3.2 d.

3.3. Non-ionic surfactants

The mesostructures made with the non-ionic surfactants Pluronic P123 or Brij 56 exhibit out-of-plane reflections of considerable intensity (Figure 3.1 b-c). However, as the structures evolve, in both cases the intensity of the out-of-plane reflections does not reach a plateau, but

instead decreases significantly with time after showing an early maximum, indicating the metastability of the circular hexagonal phase. In both samples produced with non-ionic surfactants, the in-plane reflections show increasing intensity even after the intensity maximum of the respective out-of-plane reflections has passed. These results strongly support our earlier hypothesis (Chapter III, Section 2) that the circular hexagonal phase is kinetically favored but that it does not represent the stable phase in these mesostructured systems.

3.3.1. Brij 56

When using Brij 56 as structure directing agent, all three mesophase orientations are observed in the diffraction pattern (Figure 3.1 b). The in-plane reflections corresponding to a larger d-spacing are assigned to the lamellar phase, and the reflections corresponding to the smaller d-spacing to the columnar and circular hexagonal phases, respectively. The ratio of their d-values is $1 : 0.9$, which is in good agreement with the theoretically expected value $\sin(120°)$. In the first 20 minutes of structure formation, the intensity of the ip reflections with the smaller d-spacing progresses in the same manner as the intensity of the oop reflections. In the following 30 minutes of the synthesis, the intensity of the out-of-plane reflections vanishes completely, while the intensity of the in-plane reflections increases to finally reach a plateau after 95 minutes following the beginning of the experiment. Hence, the circular hexagonal structure forms first and is then transformed into the columnar structure. The lamellar structure forms after 45 minutes, roughly at the same time as the columnar structure starts to form. At the end of the synthesis, the circular structure has completely transformed into the columnar and the lamellar phases. This is confirmed by TEM images, showing a well-preserved columnar phase and a degraded lamellar phase (the latter was observed to immediately collapse after irradiation by the electron beam). It should be noted that the columnar phase most often resides in the centre of the AAM-channels, surrounded by the lamellar phase. The silica/surfactant lamellae are more and more curved when located closer

to the center of the AAM channels (Chapter II, Figure 6). Apparently the mesostructure avoids these high curvatures by forming a columnar hexagonal structure in the center of the AAM channels.
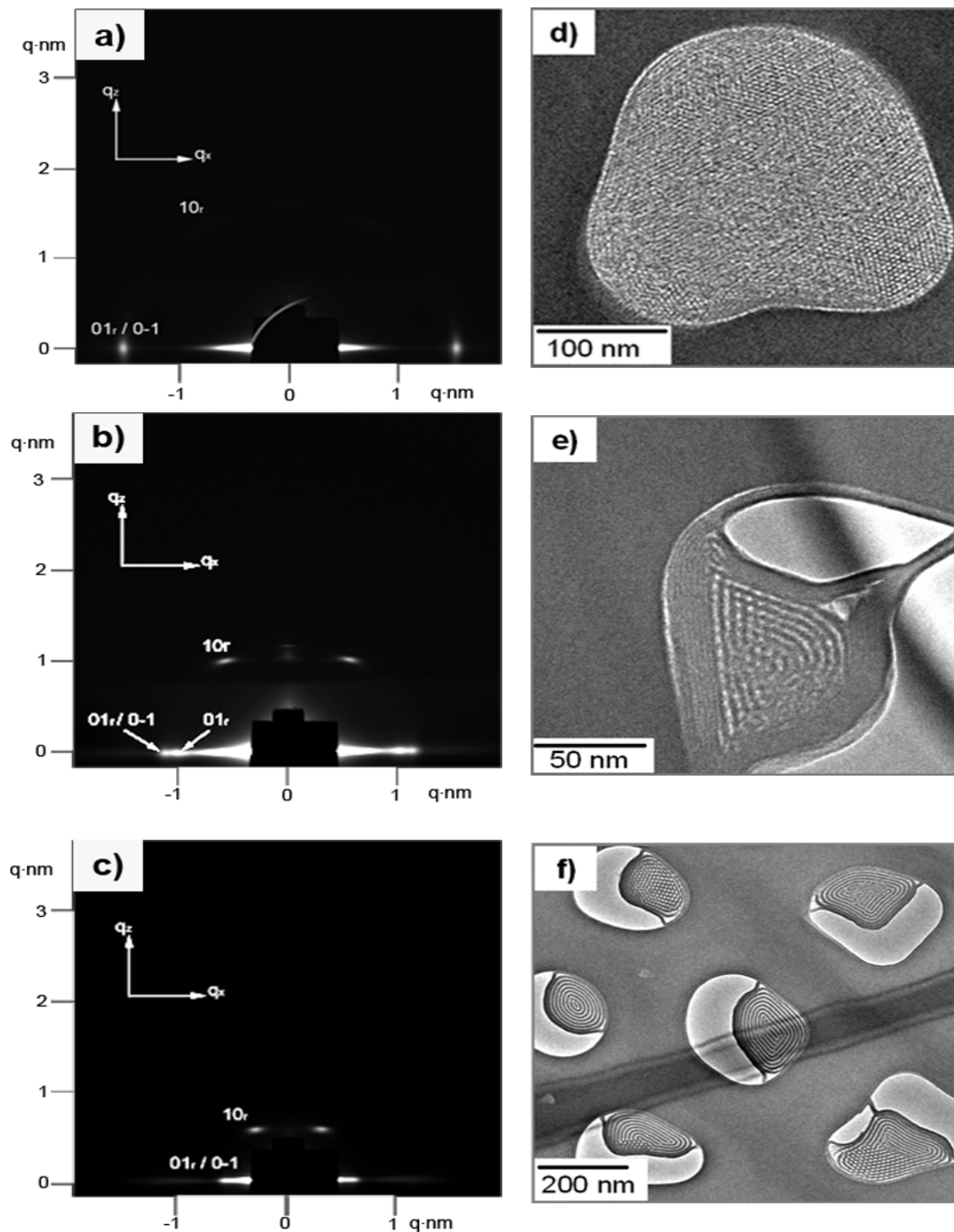

Figure 3.2 (a, b, c): Diffraction patterns from different samples.

a) Sample synthesized with CTAB and recorded after 70 minutes,
b) synthesized with Brij 56 and recorded after 57 minutes, and
c) synthesized with Pluronic P123 and recorded after 63 minutes.

The pattern of the sample synthesized with CTAB (a) shows mainly the formation of the columnar structure. The pattern of the sample synthesized with Brij 56 (b) shows the in-plane reflection closer to the primary beam that corresponds to a lamellar structure, as well as the in-plane reflection that is a superposition of the reflections corresponding to the columnar and the circular hexagonal structure. The oop-reflection corresponding to the circular hexagonal structure is also present in this pattern. The pattern of the sample synthesized with P123 (c) shows the existence of a circular and a columnar hexagonal phase. The strong superposition from the ip-reflections with the primary beam made it impossible to confirm or exclude a possible second maximum corresponding to a lamellar phase. Instead, the formation of a lamellar phase was excluded with high probability from the corresponding TEM images (see text).

Figure 3.2 (d, e, f): Corresponding transmission electron micrographs showing the plane perpendicular to the AAM-channel axis.

d) The columnar hexagonal mesophase was found in the sample synthesized with CTAB.
e) The sample synthesized with Brij 56 as surfactant shows a mixture of the columnar hexagonal and the lamellar structure, (where the lamellar phase collapsed when irradiated with electrons). This example is representative for most cases, showing the lamellar phase located at the AAM channel wall surrounding the columnar hexagonal phase in the center of the channels.
f) The sample synthesized using Pluronic P123 shows a mixture of the circular and the columnar hexagonal phase. In contrast to the lamellar phase in the sample synthesized with Brij56, no degraded lamellar phase was observed.

3.3.2. Pluronic P123

Mesostructure synthesis using Pluronic P123 as template results in the first detectable structure after 42 minutes, and the out-of-plane and in-plane intensity curves show the same shape for up to 60 minutes (Figure 3.1 c). In the following 30 minutes the intensity of the oop reflections strongly decreases, while the intensity of the ip reflections reaches a plateau. After 90 minutes, the intensity of the in-plane and the out-of-plane reflections decreases simultaneously, which suggests a general decrease in the mesophase order. The lamellar and the columnar hexagonal structure could not be distinguished in this case as the corresponding reflections for Pluronic P123 are located too close to the primary beam, where the superposition with the diffuse scattering from the AAM is relatively strong (compare Figure 3.2 c). In combination with the short distance between the first order reflections of both structures it was impossible to distinguish more than one maximum. However, Pluronic P123 was used at low concentrations to exclude the formation of a lamellar structure (Chapter III, Section 2). The intensities of both the out-of-plane and the in-plane reflections remain at a

high level, thus the circular phase as well as the columnar hexagonal or the lamellar phase are present after the synthesis was completed. The co-existence of the circular and the columnar hexagonal phase within this sample was confirmed by TEM (Figure 3.2 f).

For all three structure directing agents the start of the structure formation is correlated with the weight loss. All samples have roughly the same weight of 0.6 g (i.e. 0.75 ml of precursor solution distributed on the AAMs) at the initiation of the experiment. For the sample synthesized with Brij 56, the solvent evaporation is faster than for the samples synthesized with Pluronic P123 and CTAB, respectively. The same trend is observed for the start of the structure formation. While the Brij 56 sample shows first reflections after 35 minutes, the mesostructure of the Pluronic P123 sample occurs after 42 minutes, and the mesostructure formation in the CTAB sample starts after 50 minutes. At these respective times, the remaining weight of the samples was around 25% of their initial weight. For both samples synthesized with the non-ionic surfactants Pluronic P123 or Brij 56 it should be noted that at the point where the transformations between ordered phases start, the final sample weight is already reached. Hence, these transformations are independent of ongoing solvent evaporation.

3.4. Sample preparation

2.08 g (0.01 mol) tetraethyl orthosilicate (TEOS, Aldrich) was mixed with 3 g 0.2 M HCl, 1.8 g H_2O and 5 ml EtOH and heated at 333 K for 1 h to accomplish acid-catalyzed hydrolysis-condensation of the silica precursor. For the preparation of cetyltrimethylammonium bromide (CTAB)-containing deposition mixtures this solution was mixed with 0.947 g (2.6 mmol) CTAB dissolved in 10 ml EtOH. The decaethylene glycol hexadecyl ether (Brij 56)-containing samples were prepared by adding 1.81 g (2.65 mmol)

Brij 56 dissolved in 23.7 ml ethanol. For the preparation of the poly(ethylene oxide)$_{20}$-poly(propylene oxide)$_{70}$-poly(ethylene oxide)$_{20}$ (Pluronic P123)-containing solutions the pre-hydrolyzed silica was mixed with 15 ml of a 5 wt% ethanol solution of Pluronic P123 (0.13 mmol). The AAMs (47 mm, Anodisc^{TM}, Whatman) with average pore diameters of 120-200 nm and thickness of approximately 60 µm were mounted on a balance and soaked with the prepared precursor mixtures by distributing 0.75 ml over the whole membrane surface immediately before starting the *in situ* measurements. During the EISA-process, the ambient conditions were kept at 35-40% relative humidity and 299 K, respectively.

4. *In situ* GISAXS study of the formation of mesostructured phases within the pores of anodic alumina membranes – humidity dependence

In the previous chapter, results from *in-situ* GISAXS experiments on samples synthesized with ionic CTAB, or non-ionic Brij 56 or Pluronic P123 as structure directing agents were discussed. A previously postulated lamellar phase consisting of hollow cylinders stacked into each other was shown to exist in these systems. A significant difference was observed between samples synthesized with an ionic surfactant, that showed the direct formation of the columnar structure, and samples synthesized with non-ionic surfactants, that showed initially the formation of a circular hexagonal phase followed by a phase transformation into a columnar, or a mixture of columnar and tubular lamellar phase. These results showed that the circular hexagonal phase is kinetically favored but finally transforms into more stable phases.

The structural evolution of EISA-based films[10] was reported to take place during a period called the modulable steady state (MSS)[11] and is influenced by progressive silica condensation stiffening the film, by the kinetics of micelle (re)arrangement, and by the chemical composition of the film. The chemical composition depends not only on the amount of the non-volatile components (surfactant and silica) that are affected by the composition of the synthetic solution. Because the film is in equilibrium with the atmosphere during MSS, the amount of water or ethanol within the film is fixed by the atmospheric conditions, e.g., relative humidity. Furthermore, the systems can be highly dynamic. During increasing degrees of condensation, the solvent molecule diffusion is affected and quenching of intermediate structures is possible. Thus, relative humidity has an influence on both the final chemical composition of the film but as well influences the rate of silica condensation and thereby the kinetics of the system.

In this chapter an *in situ* GISAXS study is presented regarding the dependence of the structure formation on the humidity when the synthesis is carried out in the confined space of AAM channels. The results from samples synthesized with the non-ionic surfactants Brij 56 and P123 at two different surfactant : silica ratios are evaluated, respectively. TEM imaging reveals spatial variations typical for the structures formed in confined spaces. It is emphasized that results regarding mesoporous films on flat substrates are not easily transferred to these new systems.

By simultaneously recording the sample weight during the *in situ* measurements, we can follow the drying process of the samples. It is demonstrated that the samples show structure formation and transformations after complete solvent evaporation similar to what is observed in the formation of thin films. A mechanism for nucleation and phase formation of mesostructured material in confined environments is proposed (Chapter III, Section 5).

The synthesis was carried out at 20% and 60% relative humidity, respectively. In the following, a Brij 56 : silica molar ratio of 0.133 or a P123 : silica molar ratio of 0.013 will be referred to as low template concentration, a Brij 56 : silica molar ratio of 0.265 or a P123 : silica molar ratio of 0.017 will be referred to as high concentration of template. The samples will be named giving the type and concentration of the surfactant and the relative humidity during the EISA process. The capital letters P and B index the surfactant P123 or Brij 56, and the letters L and H indicate the low or high surfactant : silica ratio, respectively. The relative humidity will be given at the end of the sample code. For example B-L-20 names a sample synthesized at 20% relative humidity with a Brij 56 : silica ratio of 0.133 in the precursor solution. A summary of the samples investigated in this study and their codes is given in Table 4.1.

Table 4.1: Sample codes and respective synthesis conditions

Sample code	Structure directing agent	Surfactant : silica ratio	Relative humidity during EISA
B-L-20	Brij 56	0.133	20%
B-L-60	Brij 56	0.133	60%
B-H-20	Brij 56	0.265	20%
B-H-20	Brij 56	0.265	60%
P-L-20	P123	0.013	20%
P-L-60	P123	0.013	60%
P-H-20	P123	0.017	20%
P-H-20	P123	0.017	60%

4.1. General

The weight loss with time was recorded simultaneously during *in situ* X-ray experiments and therefore can be directly correlated with the structure formation. The drying curves for all samples investigated in this study are depicted in Figure 4.1. The filled symbols in the graphs indicate the time period during which ordered structure was observed. Comparing the final weight of each sample with the respective sample weight before evaporation, we found that up to 5% of the solvent does not evaporate. Exceptions were only found in samples synthesized with P123 at 20% humidity. Here the final sample weight corresponds to complete evaporation of ethanol and water. In all other cases, the "dry" samples may contain a certain amount of water. Nevertheless, we will refer to the period of constant sample weight as after solvent evaporation or after drying.

In general, it is observed that samples need more drying time when synthesized at 60% humidity and less drying time when synthesized at 20% humidity. Detectable structure formation starts after about 20 minutes for syntheses at low humidity and after 40 minutes at high humidity. Assuming a preferential evaporation of ethanol, structure formation starts after all ethanol and 40-60% of water is evaporated. An exception is the sample B-H-60. The structure was observed to form at about the same time as in the sample B-H-20 when the sample still contains about 5% ethanol. Supposedly, this is due to the comparatively high

surfactant : silica ratio. In this case, the sample already reaches the critical micelle concentration and forms a structure after a short drying time.
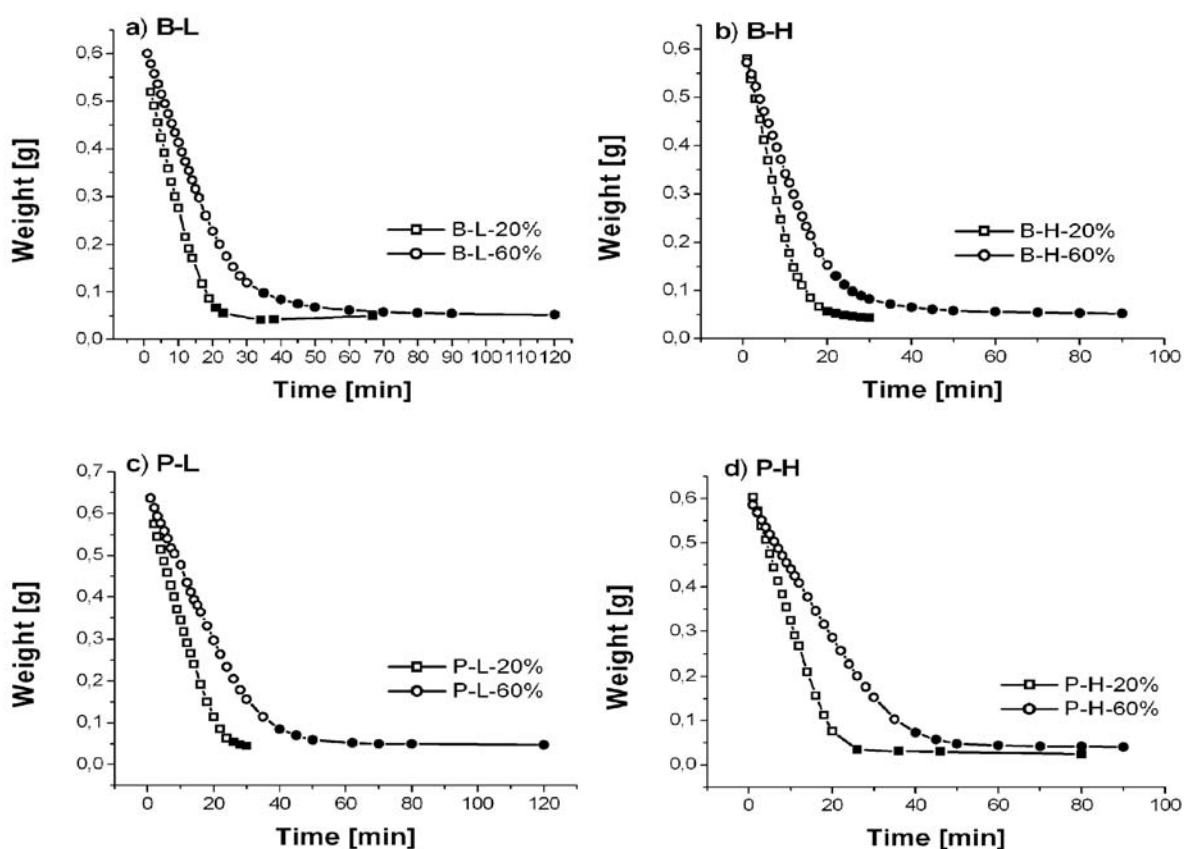
Figure 4.1: Drying curves of samples
   a) synthesized with Brij 56 at a low concentration
   b) synthesized with Brij 56 at a high concentration
   c) synthesized with P123 at a low concentration
   d) synthesized with P123 at a high concentration at 20% and 60% relative humidity, respectively.
Mesostructure was observed during the time period indicated by filled symbols.

After detection of the first reflections, the intensity of the diffraction spots increases in all samples due to the increasing order of the mesophase. In most cases, this period is followed by phase transformations until the final composition is reached. A summary of all phase transformations observed within the different samples is given in Table 4.2. Structure formation and transformations take place during about 20-45 minutes after immersing the membranes in synthesis solution for the samples at 20% relative humidity, and during 35-60 minutes for the samples at 60% relative humidity (20-60 minutes for sample B-H-60, respectively). These observations show that all samples retain a certain degree of structural

flexibility even after completion of the EISA process, probably corresponding to the modulable steady state observed in thin film synthesis. [11]

Table 4.2: Summary of the phase transformations observed
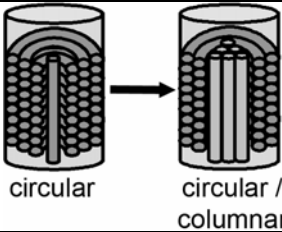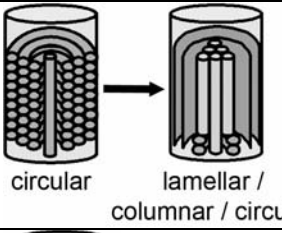
Phase transformations	Observed in samples
circular	B-L-20
circular → circular / columnar	B-L-60 P-L-20 P-L-60
circular → lamellar / columnar / circular	B-H-20 B-H-60 P-H-60
lamellar / columnar	P-H-20

Figure 4.2 shows TEM images from a cross section prepared from P-H-60. These images serve to illustrate the different phases observed in the samples and to show the occurrence of domain boundaries between the intra-channel mesophases. The images show domain–domain boundaries between circular and columnar or lamellar phases. It is sometimes difficult to distinguish between the columnar and the lamellar structure in cross-section TEM, since both phases show a pattern of straight lines. Nevertheless, the pattern from the lamellar structure is usually less regular in TEM cross-sections than the line pattern of the columnar phase, due to the lack of a three-dimensional network (Figure 4.2 a). When the plane normal to the AAM surface is imaged, the lamellar phase is observed to collapse immediately in the electron beam (Figure 4.4, 4.6).
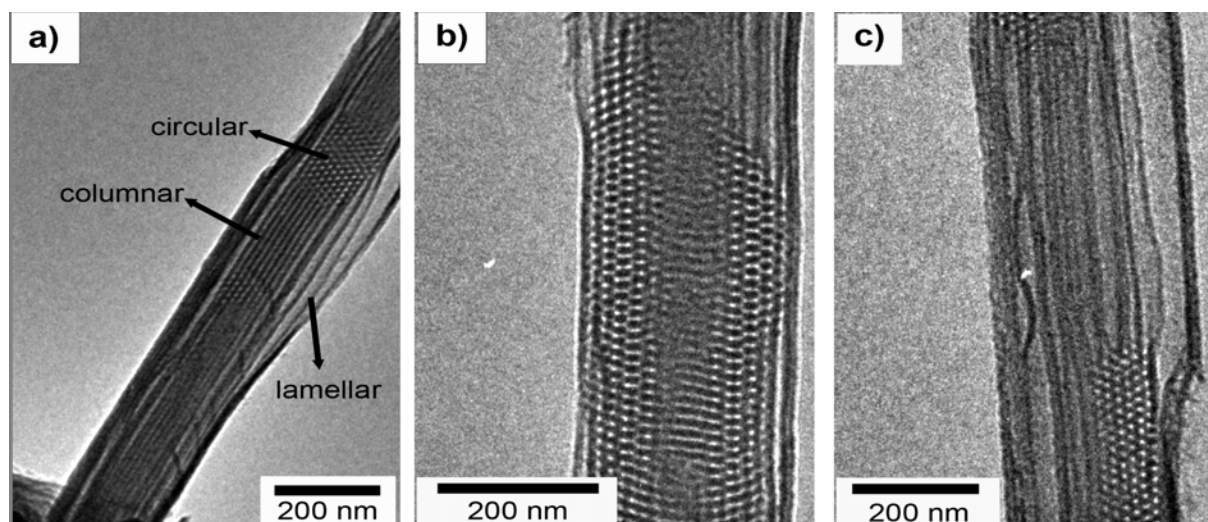
Figure 4.2: TEM cross-section images of B-H-60 showing
   a)   phase transitions between donut-like circular, columnar and lamellar phases,
   b)   transitions between spiral-like circular structures and lamellar (or columnar) phases,
transitions between circular and lamellar (or columnar) phases.

As mentioned above, various domain boundaries between the circular and the lamellar (or columnar) phase were observed. The presence of different structures and phase boundaries randomly distributed along the fiber axis indicates that the disorder-to-order transition or/and phase transformations start at various different positions inside the AAM channels.

4.2. Brij 56 – low concentration (B-L)
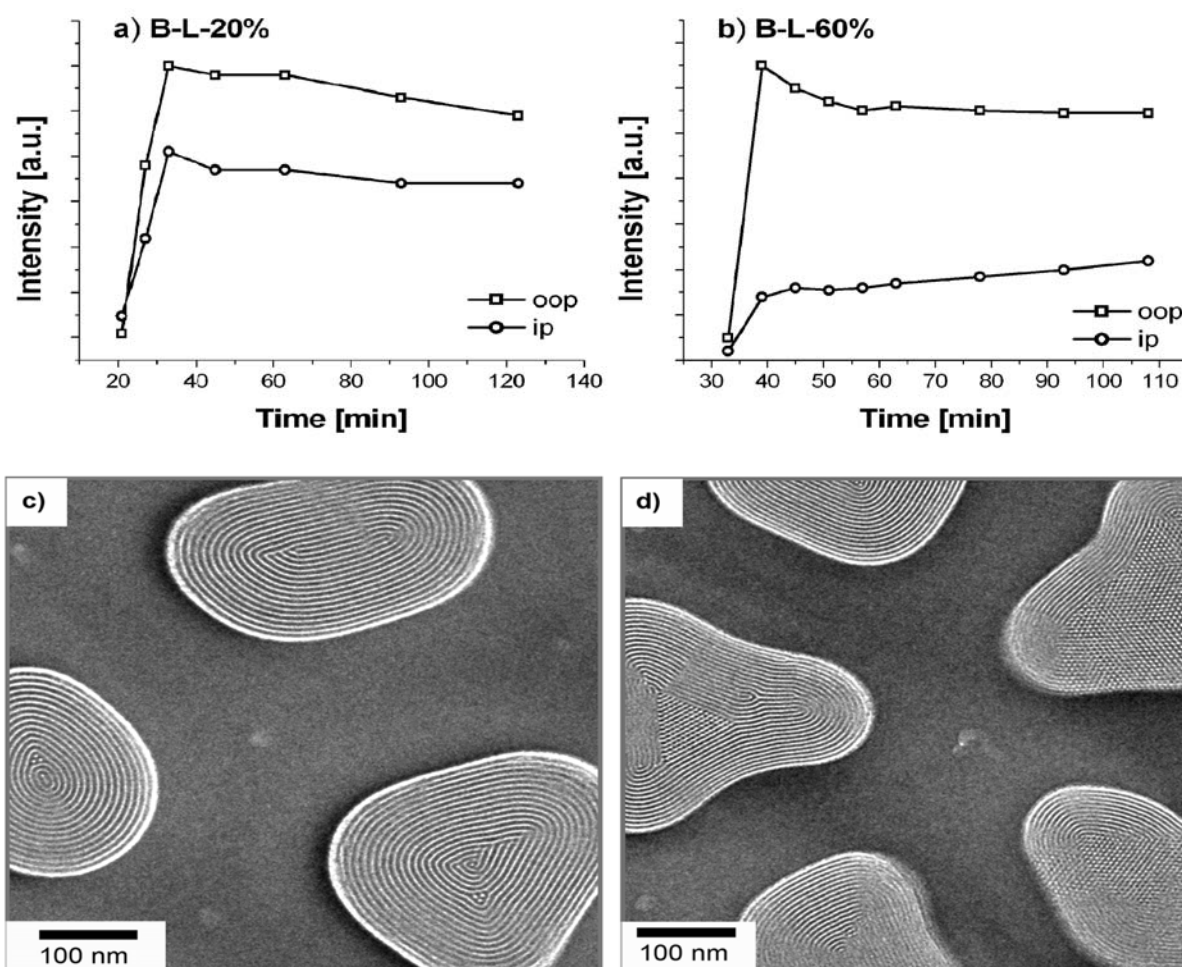
Figure 4.3: Intensity of the ip- and oop-diffraction spots plotted versus time for the samples synthesized using Brij 56 as template at a low concentration (B-L samples) at
  a) 20%, and
  b) 60% relative humidity.
Corresponding TEM images from the respective samples are presented as plan-view of the AAM surface.
  c) The exclusive presence of a circular structure is confirmed in the sample synthesized at low humidity.
The sample synthesized at high humidity shows a mixture of the circular and the columnar orientation.

In sample B-L-20% the formation of a structure was observed after 20 minutes synthesis time (Figure 4.3 a). The intensities of the oop- and the ip-reflections simultaneously show a steep increase for the next 15 minutes representing the formation and growth of circular hexagonal domains. After that, the intensity of the reflections remain quite constant at this level, the oop-reflections showing a slight decrease in intensity after 60 minutes synthesis time. The similar temporal evolution of the intensities of the oop- and ip-reflections is interpreted as the

formation of a circular hexagonal phase. This is confirmed by TEM images from this sample showing the circular arrangement of the mesophase within the AAM channels (Figure 4.3 c).

If the same synthesis is performed at 60% relative humidity, the first reflections are observed after 32 minutes (Figure 4.3 b). This shows that increased relative humidity slows down the synthesis, since the first formation of structure at 20% relative humidity was observed 12 minutes earlier. The structural order is strongly increased within the next 10 minutes, represented by the steep increase of intensity for both reflections. In the following 20 minutes the intensity of the oop-reflections decreases while the intensity of the ip-reflections is still slightly increasing. This is interpreted as a partially phase transformation from the circular hexagonal to the columnar hexagonal phase. The intensity of the ip-reflections shows a constant increase even after 60 minutes, while the intensity of the oop-reflection remains constant at their decreased level. The TEM images presented in Figure 4.3 d show that a phase mixture of a circular and a columnar oriented hexagonal mesostructures was formed within the channels of the AAM.

Assuming a lower flexibility of the system at low humidity due to faster silica condensation, it is not surprising that the kinetically favored circular hexagonal phase cannot be transformed into the more stable columnar phase. At higher humidity, phase transformation towards the more stable structure is possible. Another possible explanation for the different phases observed at different humidities could invoke their different chemical composition. However, the water content of the final compositions is the same within our measurement accuracy. Moreover, lower amounts of water should rather lead to a smaller head group area and therefore to structures with decreasing micelle curvature (columnar phase). Thus, the first explanation is strongly supported by the experiments.

TEM images of sample B-L-60 show many examples where the columnar structure is formed in the middle of one channel and surrounded by a circular phase. The opposite has not been observed. The silica rods forming the mesophase become more and more curved when located closer to the center of the fiber resulting in energetically less favored conformations. A similar effect was observed for the lamellar structure, where a columnar phase is forming at the fiber center instead of highly curved lamellae (Chapter III, Section 3). The TEM picture depicted in Figure 3d shows one example of an AAM channel of triangular shape. The silica rods forming the circular phase would be forced to mimic this triangular shape being highly curved at the three sharp edges. Instead, a columnar phase is formed in the middle of the fiber, because of the hexagonal order perfectly fitting the triangle. Therefore we suppose that the phase transformation from the circular to the columnar structure starts at locations where the circular rods are highly curved and the energetic difference between both orientations is comparatively large.

Regardless of the orientation, we observed the exclusive formation of a hexagonal structure in the samples B-L-20% and B-L-60%. Interestingly, when the same precursor solution is spin-coated on flat glass substrates, the formation of a hexagonal-lamellar phase mixture is reported (Compare Chapter III, Section 8). We suppose that this striking difference results from the drastically different boundary conditions, namely the curved spatial confinement of the AAM channels.

4.3. Brij 56 – high concentration (B-H)

For sample B-H-20 the first formation of an ordered mesostructure was observed after 20 minutes (Figure 4.4 a). A circular structure is formed within the next five minutes, possibly mixed with a columnar phase. Later on, the oop-reflection intensity corresponding to the circular phase continuously decreases, and a lamellar phase starts to form. The circular phase

transforms to the columnar hexagonal and the lamellar structure during the next 20 minutes. Afterwards, the reflections corresponding to the circular phase remain at a level hardly above the detection limit while the columnar hexagonal structure is partially transforming into the lamellar phase.
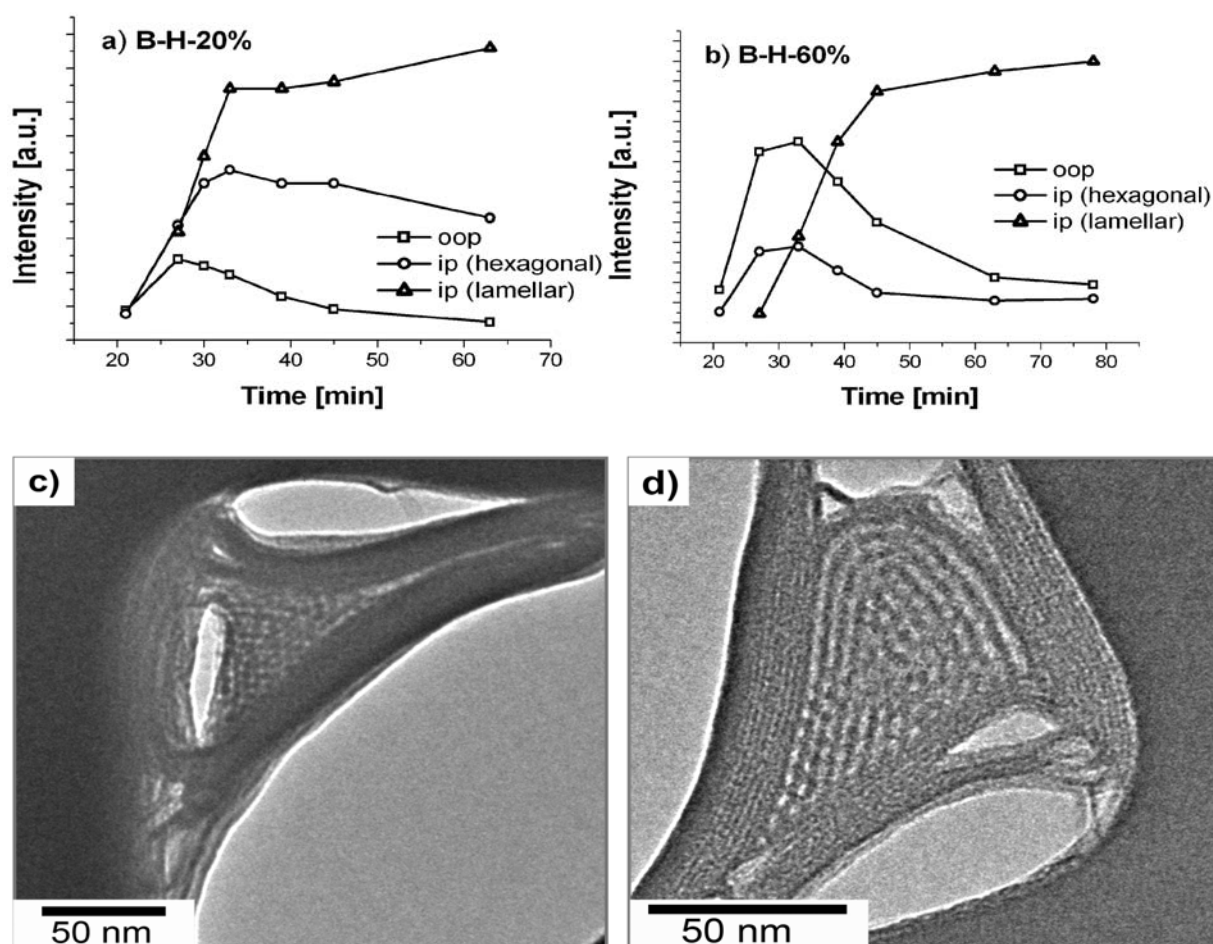
Figure 4.4: Intensity of the ip- and oop-diffraction spots plotted versus time for the samples synthesized using Brij 56 as template in a high concentration (B-H-samples) at
  a) 20% and
  b) 60% relative humidity.
Corresponding TEM images from the respective samples are presented viewing the plane normal to the AAM surface.
  c) The sample synthesized at low humidity was not stable over time. SAXS measurements confirm that the formerly well-ordered structure was destroyed with time. Nevertheless, the presence of ordered lamellar and columnar structure is visible in a few selected TEM images.
  d) The sample synthesized at high humidity shows a mixture of the circular, the columnar and the lamellar mesostructure in the micrographs [d)].
Note that the lamellar phase is collapsing during sample preparation or when irradiated with electrons.

For sample B-H-60, the first formation of an ordered phase was again observed after 20 minutes synthesis time (Figure 4.4 b). The reflections corresponding to the circular structure reach maximum intensity after 32 minutes, before the structure transforms to the tubular

lamellar phase. After 45 minutes, the oop-reflections still show a decrease in intensity, while the ip-reflections corresponding to the hexagonal phase remain at their intensity level. This indicates that the circular phase is still transforming into the lamellar phase, while the columnar phase is stable. TEM images of the sample show a final composition of a circular-columnar-lamellar phase mixture (Figure 4.4 d).

TEM images of both samples show that the lamellar phase is always formed at the channel wall surrounding a columnar phase formed at the center of the silica fibers as reported in the previous section. A lamellar phase in the confined space of an AAM channel has a special geometry, where lamellae that are located closer to the center have smaller diameters and higher curvature of the silica sheets. Hence it is suggested that the spatial confinement within the AAM channels results in energetically unfavorable configurations for high curvatures of the silica sheets and that the formation of a columnar phase is favored in the fiber center. A higher volume fraction of columnar phase is formed at low humidity. This again indicates a less flexible system at low humidity, thus hindering the system to transform to a larger degree into the more stable tubular lamellar phase.

4.4. P123 – low concentration (P-L)

P123 was used as template at low concentrations to exclude the formation of a lamellar structure (P123 : silica ratio of 0.013, Chapter III, Section 2). When the synthesis was performed at 20% relative humidity, the formation of structure was observed to start after 25 minutes (Figure 4.5 a). Note that the oop-reflections became visible about 5 minutes earlier than the ip-reflections. Ip-reflections must be rather strong to be detected because they are superimposed by the intense diffuse scattering of the AAM close to the primary beam. After 32 minutes, the circular phase transforms into the columnar hexagonal structure, whose reflections have an intensity maximum after 50 minutes synthesis time. Later, the intensity of

the reflections decreases constantly, possibly reflecting a certain loss of order of the finally

formed structure. In the sample synthesized at 60% relative humidity the formation of

structure was observed after 40 minutes (Figure 4.5 b). After 60 minutes synthesis time, the

circular phase partially transforms to the columnar phase for the next 40 minutes.

Figure 4.5: Intensity of the ip- and oop-diffraction spots plotted versus time for the samples synthesized using P123 as template in a low concentration (P-L- samples) at
   a)   20% and
   b)   60% relative humidity.
Corresponding TEM images from the respective samples are presented viewing the plane normal to the AAM surface. The presence of a mixed columnar and circular phase is confirmed in the sample synthesized at both humidities.

Both of these P123-based samples (at low and high humidity) show initially the formation of

a circular structure that partially transforms into a columnar phase. The transformation is

more pronounced at low humidity than at 60% relative humidity.

The larger fraction of columnar orientation in the sample synthesized at lower humidity is

confirmed by TEM images from both samples; a lamellar phase was not observed (Figure 4.5

c, d). Interestingly, the columnar orientation was formed rather randomly at the fiber center as well as close to the channel wall. This was not observed in the samples synthesized with Brij 56; the different behavior may be related to the different micellar dimensions in both cases.

4.5. P123 – high concentration (P-H)

For sample P-H-20% no oop-reflections could be observed (Figure 4.6 a), indicating the absence of a circular hexagonal structure. The first ip-reflections were observed after 25 minutes synthesis time when the final sample weight was already reached. They increase in intensity and after about 60 minutes remain at the final intensity level. TEM images from this sample show a combination of columnar hexagonal and tubular lamellar phases (Figure 4.6 c). Consistent with the above results, the lamellar phase surrounds the columnar phase formed at the center of the silica fibers. These two phases cannot be separately followed in the diffraction patterns, since the corresponding ip-reflections cannot be distinguished (Chapter II, Section 3.2). The sample synthesized at 60% relative humidity shows the formation of a circular phase observed after 40 minutes which subsequently transforms to a phase mixture of tubular lamellar and columnar hexagonal phase, as confirmed by TEM (Figure 4.6 b, d).
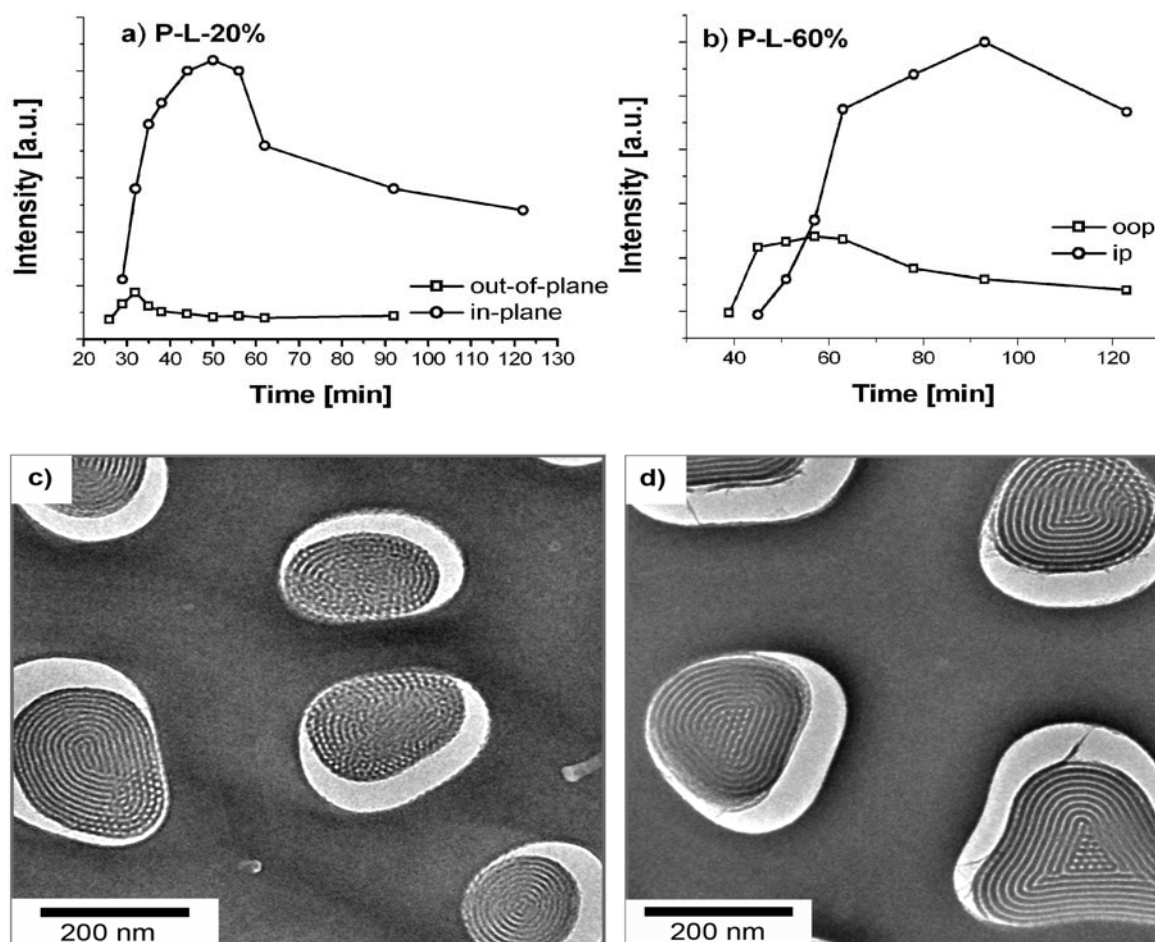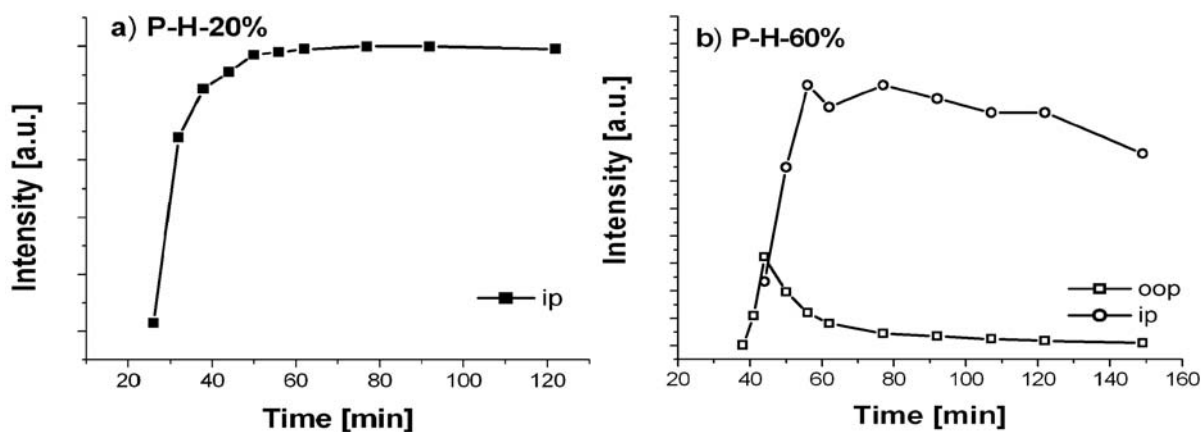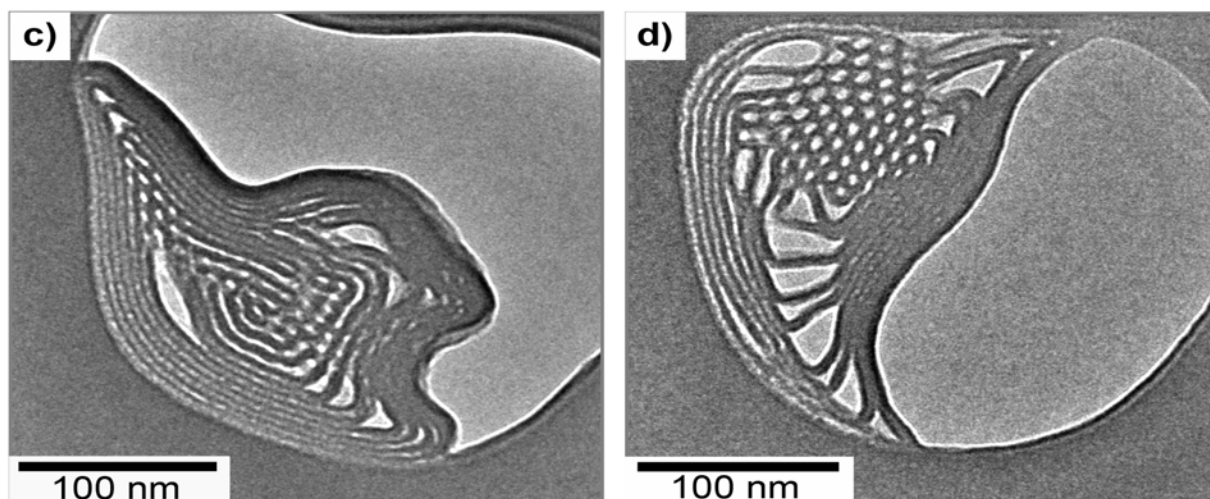
Figure 4.6: Intensity of the ip- and oop-diffraction spots plotted versus time for the samples synthesized using P123 as template in a high concentration (p-H-samples) at
   a)   20% and
   b)   60% relative humidity.
 c), d) Corresponding TEM images from the respective samples are presented viewing the plane normal to the AAM surface. A columnar-lamellar phase mixture was found in both samples. Just as with the samples B-H-20% and -60%, the lamellar phase is partially collapsed in the electron beam.

4.7. Sample preparation

For the synthesis, 2.08 g (10 mmol) of tetraethyl orthosilicate (TEOS, Aldrich) were added to 3.0 g of 0.2 M HCl, 1.8 g H_2O and 3.95 g EtOH and heated at 60 °C for 1 h for prehydrolysis. For the preparation of the precursor solutions of for the samples B-L-20 and B-L-60, 0.906 g (1.33 mmol) Brij 56 were dissolved in 11.85 g ethanol. The samples B-H-20 and B-H-60 were prepared using 1.81 g Brij 56 (2.65 mmol) were dissolved in 23.7 g ethanol. The P123-containing solutions were prepared using 0.75 g P123 (0.13 mmol) dissolved in ethanol for P-L-20 and P-L-60, and 1.0 g P123 (0.17 mmol) in 15.8 g ethanol for the synthesis of P-H-20 and P-H-60, respectively. After cooling to room temperature, the surfactant solutions were added to the corresponding prehydrolysed silica solutions under shaking for five minutes., respectively. The AAMs (47 mm, Anodisc™, Whatman) with average pore diameters of 120-200 nm and a thickness of approximately 60 µm were mounted onto a 5x5 cm Teflon block sitting on a balance, and soaked with the prepared precursor mixtures by distributing 0.75 ml over the whole membrane surface immediately before starting the *in situ* measurements. The

drying process was recorded by measuring the weight loss of the samples simultaneously during the *in situ* diffraction measurements. During the EISA-process, the ambient conditions were kept at 26 °C and 20% or 60% relative humidity, respectively.

5. Proposed mechanism for mesostructure formation inside AAM channels

In the following, a possible formation mechanism for the various mesophases in the AAM channels is discussed, based on the observations presented in the previous two sections. A one-dimensional nucleation and growth mechanism has been previously proposed for the formation of mesostructured material inside the channels of AAMs. [14] A solvent gradient in the AAM channels was assumed to be the cause for a boundary between ordered and disordered material, moving along the channels upon further solvent evaporation.

In the systems examined in the present study, cross-section TEM images (Chapter III, Figure 4.2) show various domain-domain interfaces irrespective of the height within the AAM channels. Moreover, phase transformations happen long after complete solvent evaporation and were found to preferably take place either from the channel wall to the center of the silica fibers (outside-in for transformations leading to a tubular lamellar structure) or from the fiber center to the AAM channel wall (inside-out for transformations leading to a columnar hexagonal phase). If we assume the phase transformations to be solvent gradient-induced, the different phases would rather be found at different heights within the membrane. Hence, for the present systems we propose a random nucleation and growth mechanism rather than structure formation along the channel height. Three major time periods of structure formation according to the suggested mechanism are shown in Figure 5.1.
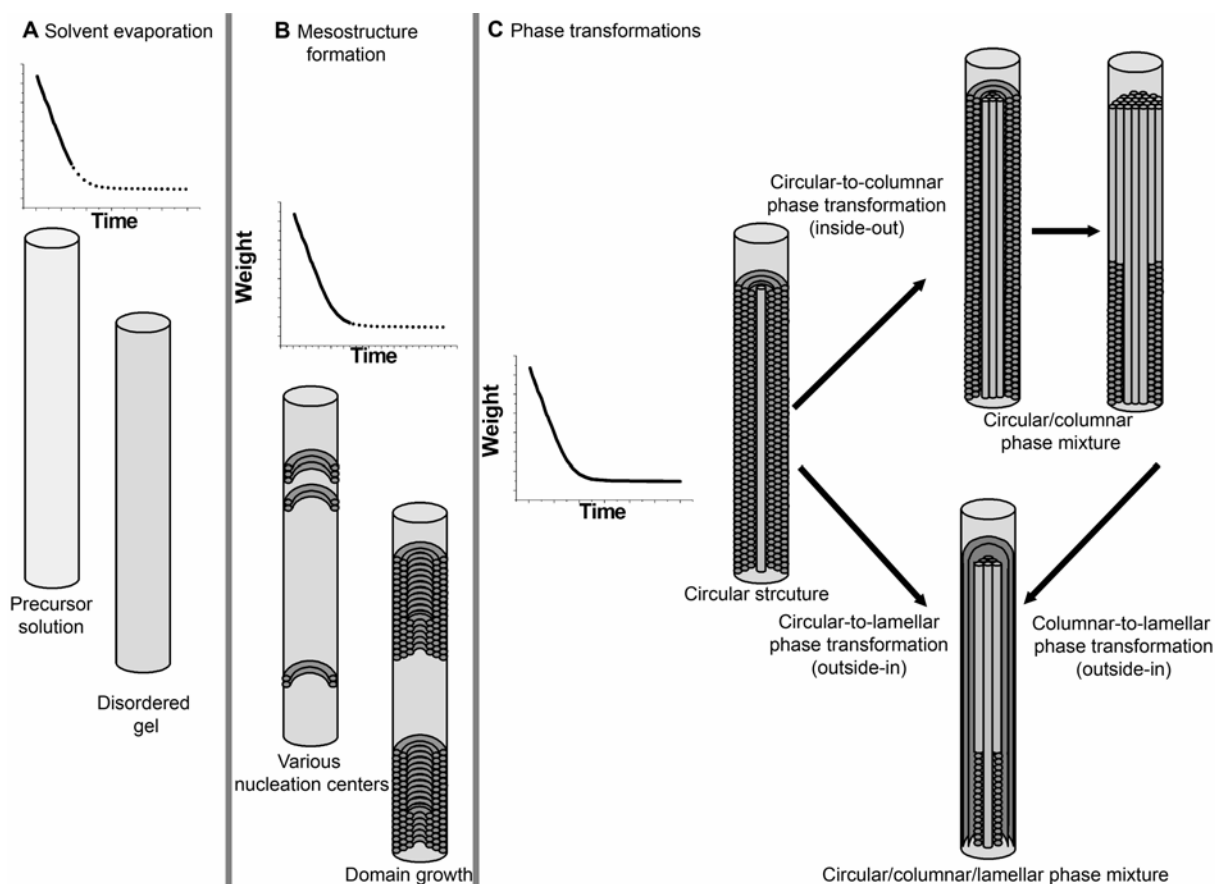
Figure 5.1: Proposed mechanism for the structure formation within the confined space of AAM channels. We distinguish three major time periods. Period A is dominated by solvent evaporation and the formation of a disordered gel. During period B the final sample weight is reached, accompanied by the formation of ordered mesostructure. The sample weight is constant during period C, corresponding to the completion of the EISA process. Various phase transformations are observed during this time period, as shown in the figure.

The first period A is dominated by the evaporation of the solvents (ethanol and water). During that period, no reflections are observed in the diffraction patterns, and a disordered gel is formed inside of the AAM channels. During the second period B, the final sample weight is reached, first reflections are observed in diffraction. This is the period of the disorder-to-order transition. We propose that the formation of ordered domains starts randomly at various positions along the channel axis at nucleation centers at the channel wall. During the last period C the sample weight remains constant and the EISA process is completed. The observed phase transformations from the circular to the columnar or lamellar structure are taking place during this time.

6. Salt-induced phase-transformation of mesostructures confined within anodic alumina membrane channels

Further applications of the mesostructured silica/alumina composite membranes (e.g. as template for the growth of nanowires or as biomembranes) often require that the AAM channels are completely filled with evenly structured phase-pure material. Nevertheless, non-ionic surfactants acting as structure directing agents resulted in hexagonal mesophases with mixed orientations (columnar and circular) or columnar / tubular lamellar phase mixtures. Addressing this challenge will permit the use of a variety of surfactants to produce ordered arrays of accessible, straight mesopores with high aspect ratios (maximum length is the thickness of the AAM) and various diameters. Previously, the effect of the geometry of the AAM channels on the formed mesostructure was experimentally studied and modeled by self-consistent field theory.[14] Although it was speculated, that the adsorption of CTAB to the channel surface might be the initial step for the formation of the composite material[9], no investigations have been made on the chemistry of the alumina surface so far.

In contrast to non-ionic templates, ionic CTAB acting as structure directing agent leads to the exclusive formation of the columnar orientation.[9,13] A reason for this different behavior might be the relatively strong Coulomb interactions between the ionic template, the charged silica-species, and the alumina wall compared to the weaker hydrogen bonding interaction between non-ionic surfactant, charged silica, and AAM surface. Recently, the behavior of the ionic surfactant CTAB was mimicked when cubic mesoporous single crystals were prepared by adding inorganic salt to a non-ionic triblock copolymer-containing synthesis solution.[15] A mechanism for the formation of silicate films at the air / water interface was discussed, proposing that a sphere-to-rod transition in the micellar structure is induced by silicate oligomers gradually replacing water molecules from the surfactant headgroups.[16,17] This change in micelle conformation was induced by addition of inorganic salt.[16] SBA-15 and

aluminum-doped SBA-15 particles with high hydrothermal stability have been produced with a non-ionic triblock copolymer by adding sodium chloride to the precursor solution.[18] It was assumed that salt-induced dehydration of the polyethylene units create a local non-polar environment stabilizing ordered arrangement of the micelles.

Additionally, increased interaction between silicate species and surfactant headgroups due to the additive electrolyte effect was discussed.[19] An adjustment of the micellar curvature by addition of inorganic salt was also reported.[20-22] Dehydration of the polyethylene oxide headgroups was assumed to reduce the effective headgroup area and therefore lead to decreased micellar curvature. An increase of the micellar radius was observed in mesostructured silica composite films upon increasing the surfactant : silica ratio and was related to changes in the surfactant headgroup area due to deceased solubilization of the polyethylene oxide units by water.[23] Extraction of water molecules from polyethylene oxide – polypropylene oxide tri-block copolymer upon salt addition was demonstrated by a recent ^{1}H-NMR spectroscopy study.[24] It was demonstrated that micellization is induced when water is removed from the polypropylene oxide moiety thus decreasing its solubility. Additionally, it was found that water molecules leave the polyethylene oxide shell of the micelles. It was argued that the ions from inorganic salts successfully compete with the polymer chains for the available water of hydration.

In this chapter, the influence inorganic salt addition on the orientation of the final mesostructure in the confined space of AAMs is examined, aiming at the synthesis of phase-pure columnar hexagonal structure even with non-ionic structure directing agents. Precursor solutions containing Pluronic P123 or Brij 56 were used. The temperature during the EISA process was also optimized, because it can result in different structures when non-ionic surfactants are used as templates.[25] Finally, the AAM channel surface was hydrophobized by

trimethylchlorosilane (TMSCl) treatment prior to the synthesis in order to investigate the influence of chemical interaction between the mesostructured material and the alumina channel wall. The progress of phase transformation was quantitatively followed by 2D small angle X-ray scattering (SAXS).

In the following, the samples are named with capital letters P or B indexing the used surfactants P123 or Brij 56, respectively. The synthesis temperature is denominated by 21 or 30 for 21 °C and 30 °C, added salt is given by its sum formula at the end; e.g. P-21-NaCl is a sample synthesized using P123 as structure directing agent at 21 °C temperature with sodium chloride.

6.1. Influence of inorganic salt addition

A first set of samples was synthesized at 21 °C. The corresponding diffraction patterns and oop:ip ratios are depicted in Figure 6.1 a-d. A summary of the oop:ip ratios of all prepared samples is given in Table 6.1. The oop:ip ratios of the diffraction patterns of the respective samples are calculated by dividing the peak height of after azimuthal angle integration and after subtraction of the background.

The subtraction of the background prevents overestimation of the oop:ip ratio (and therefore the presence of circular phase) if an almost purely columnar phase is present in a sample (high intensity of the ip-reflections and the oop-intensity close to the background). However, generally the error of the oop:ip ratio determination becomes larger if the intensity of all reflections is comparatively low, since slight intensity differences then have a high impact on the ratio. This distinct case was observed in samples B-21 and B-21-NaCl. B-21 has an oop-intensity of 5850, an ip-intensity of 5650 and a background intensity of 5350 [arbitrary units]. The oop:ip ratio is 1.7 after background subtraction, which is an unrealistically high value. In

comparison, sample B-30 has more intense reflections (oop: 6400, ip: 6300, background: 5500). In this case, the oop:ip ratio is 1.1 after subtraction of the background.

Table 6.1: Summary of the data from all prepared samples: Sample name, q-vector, d-spacing calculated from q, and the oop:ip-ratio of reflections from the respective diffraction patterns.

Sample name	Scattering vector q /nm^{-1}	d-spacing /nm	oop:ip ratio
P-21	0.62	10.2	0.7
P-21-NaCl	0.6	10.6	0.2
P-30	0.62	10.2	0.5
P-30-NaCl	0.6	10.4	0.2
P-30-LiCl	0.56	11.2	0.03
B-21	1.08	5.8	1.7
B-21-NaCl	1.08	5.8	1.6
B-30	1.05	5.9	1.1
B-30-NaCl	1.06	5.9	0.2
B-30-LiCl	1.06	5.9	0.03
P-21-KCl	0.6	10.4	0.1
P-21-KBr	0.62	10.2	0.2
P-21-KI	No structure observed		
P-21-KI*lc*[a]	No structure observed		
P-TMSCl-21	No structure observed		
P-TMSCl-21-NaCl	No structure observed		
B-TMSCl-21	No structure observed		
B-TMSCl-21-NaCl	No structure observed		
[a] *lc* indicates low salt concentration			

The reference sample P-21 has an oop:ip ratio of 0.7, while the corresponding sample synthesized with sodium chloride (P-21-NaCl) has an oop:ip ratio of 0.2 (Figure 6.1 a and 6.1 c, respectively). Thus, the reference sample exhibits a much higher fraction of the circular hexagonal phase than P-21-NaCl which shows a higher fraction of the columnar orientation. This is confirmed by TEM images viewed through the membrane plane. In case of a circular orientation the hexagonal order is not visible but the circular arrangement of the silica rods is imaged (Figure 6.2 a). In case of the columnar orientation the image is viewed perpendicular to the silica rods, showing the hexagonal arrangement of the phase in P-21-NaCl (Figure 6.2 c center). In Figure 6.2 a of sample P-21, only very little pores with columnar orientation were found, indicating that the oop:ip ratio of 0.7 is representative for a comparatively small

fraction of columnar phase. In Figure 6.2 c, showing sample P-21-NaCl, a mixture of both orientations is visible in the TEM image. Some AAM channels exhibit mesostructures with full alignment either in a circular or in a columnar way. In addition, hybrid structures were observed as well, showing both orientations formed side by side in a single AAM channel (Figure 6.2 c, right side of image). To our knowledge, similar salt-induced phase transformations (SIPT) in surfactant-templated mesophase systems have not yet been reported. As discussed above, the increased ionic strength of the precursor solutions lead to formation of less curved mesophases.[19,20]

Figure 6.1: SAXS patterns of samples
a) P-21 (oop:ip = 0.7),
b) B-21 (oop:ip = 1.1),
c) P-21-NaCl (oop:ip = 0.2), and
d) B-21-NaCl (oop:ip = 1.0) synthesized at 21 °C.

Turning now to the samples synthesized using Brij 56 as template, these systems show, both in their respective diffraction patterns as well as in the corresponding TEM images (Figures 6.1 b, d, 6.2 b, d) , the exclusive formation of circular orientation only whether or not inorganic salt was added to the precursor solution. The diffraction spots of B-21-NaCl are weaker than the ones of the reference sample, indicative for a reduced order upon salt addition. The reduction of order is confirmed by TEM, the representative image presented in Figure 6.2 d depicting areas of lesser order in comparison to the well structured circular arrangement of the mesophase in Figure 6.2 b.
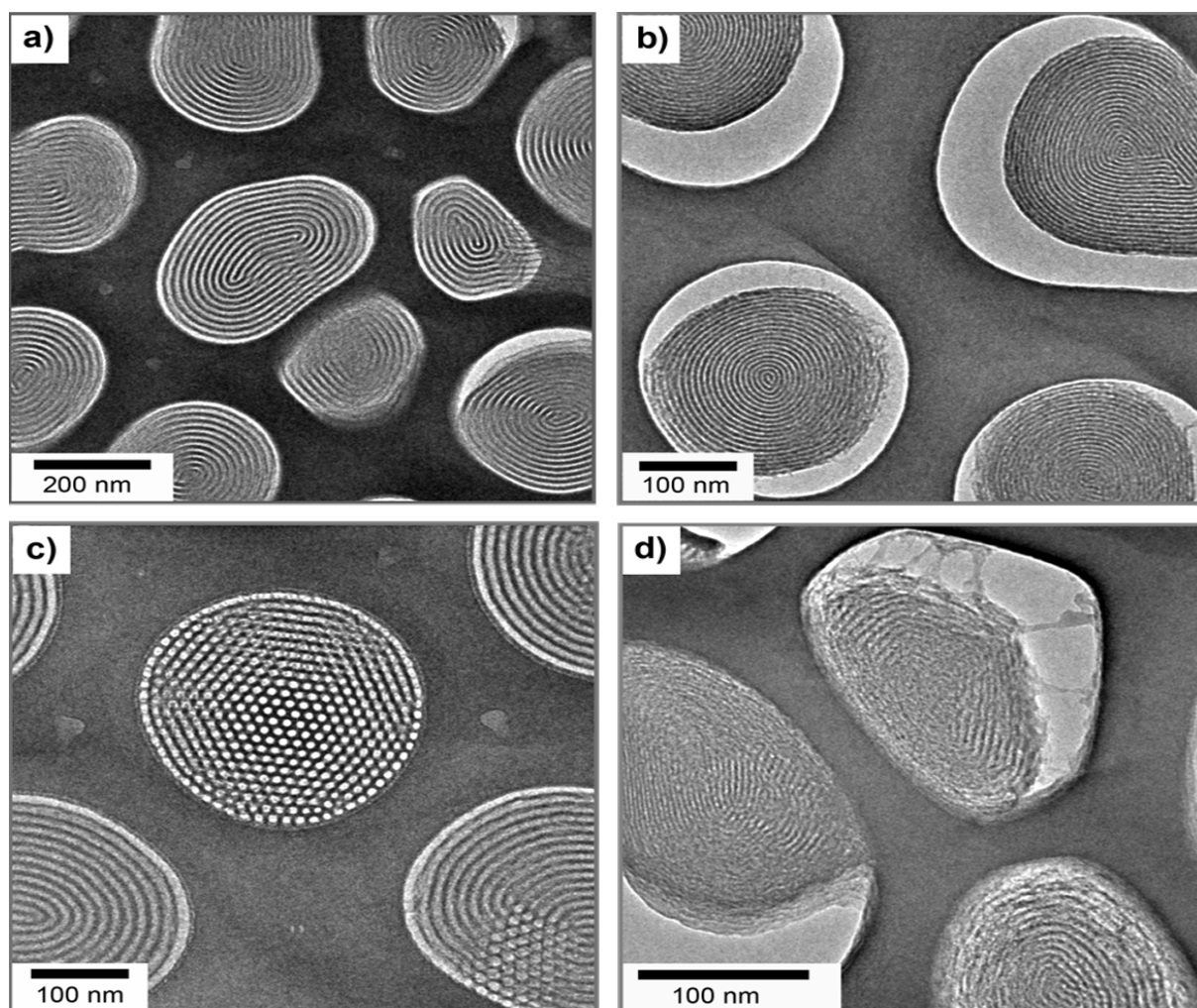
Figure 6.2: TEM images viewed normal to the AAM surface (plan-view). The reference samples
a) P-21, and
b) B-21 [b)], exhibit circular orientation. The sample
c) P-21-NaCl shows a mixture of circular and columnar orientation. Sample
d) B-21-NaCl shows a slightly distorted circular hexagonal phase.

6.2. Influence of the temperature during EISA

Figure 6.3 and 6.4 show the data for samples synthesized at 30 °C. The diffraction patterns of

the reference samples synthesized without the addition of inorganic salt using P123 and

Brij 56 as templates are depicted in Figure 6.3 a and 6.3 b, respectively. The oop:ip ratio is

about one if Brij 56 is used as template, corresponding to a pure circular phase. This is also

confirmed by the corresponding TEM images shown in Figure 6.4 b. The oop:ip ratio of

sample P-30 is 0.5, indicating a circular – columnar phase mixture, with a higher fraction of

columnar phase as compared to sample P-21 (oop:ip = 0.7), most probably due to the different

synthesis conditions (higher temperature). Nevertheless, no difference between the samples P-21 and P-30 was observed with TEM (Figure 6.2c, 6.4c). This is because TEM is a non statistical method and significant differences between two samples both exhibiting a phase mixture might be hard to extract.
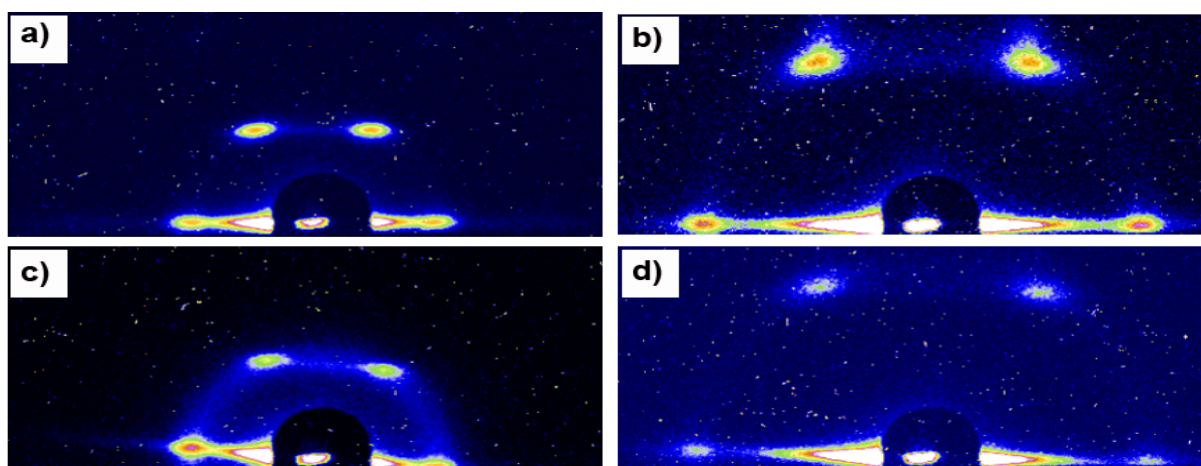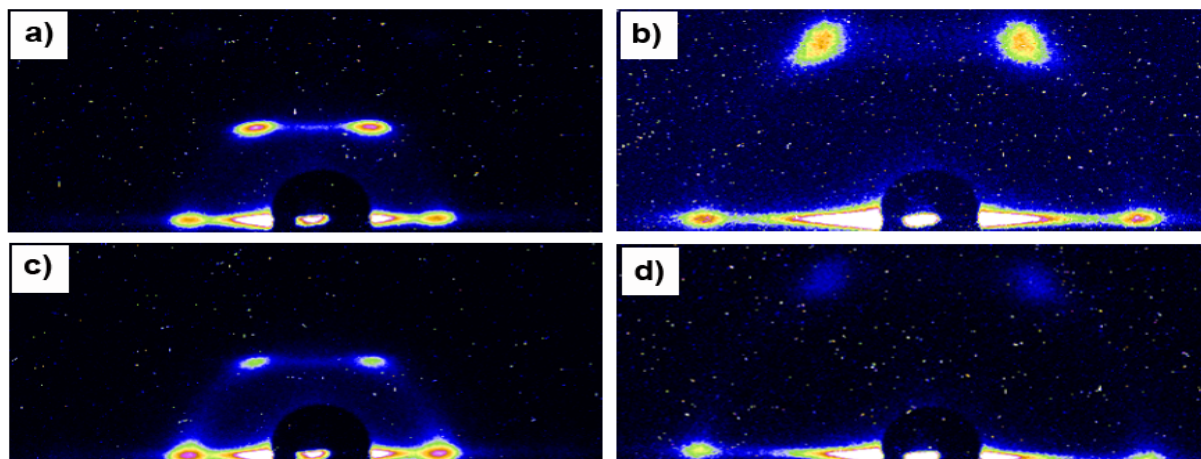

Figure 6.3: SAXS patterns from samples
a) P-30 (oop:ip = 0.5)
b) B-30 (oop:ip = 1.1)
c) P-30-NaCl (oop:ip = 0.2)
d) B-30-NaCl (oop:ip = 0.3) synthesized at 30°C.

When P123 was used as structure directing agent and sodium chloride was added to the synthesis solution, the oop:ip ratio derived from the respective diffraction pattern in Figure 6.3c is 0.2 (sample P-30-NaCl). TEM images confirm the significant transformation towards a columnar orientation; an example is given in Figure 6.4 c. This is similar to the oop:ip ratio found for the sample P-21-NaCl at 21 °C, as depicted in Figures 6.1 c and 6.2 c.

In contrast, the temperature plays a decisive role in the Brij 56-based systems. The sample synthesized at 21 °C (B-21-NaCl) showed a pure circular phase with an oop:ip ratio of 1, while sample B-30-NaCl shows an oop:ip ratio of about 0.2 (Figure 6.3 d), reflecting the formation of a circular-columnar phase mixture. The columnar orientation of the mesophase is shown in the corresponding TEM image presented in Figure 6.4 d. Hence, the salt-induced phase transformation is a concept valid for both non-ionic templates. Even Brij 56-templated

samples show a transformation from circular to columnar orientation, but only when the synthesis was carried out at elevated temperature.
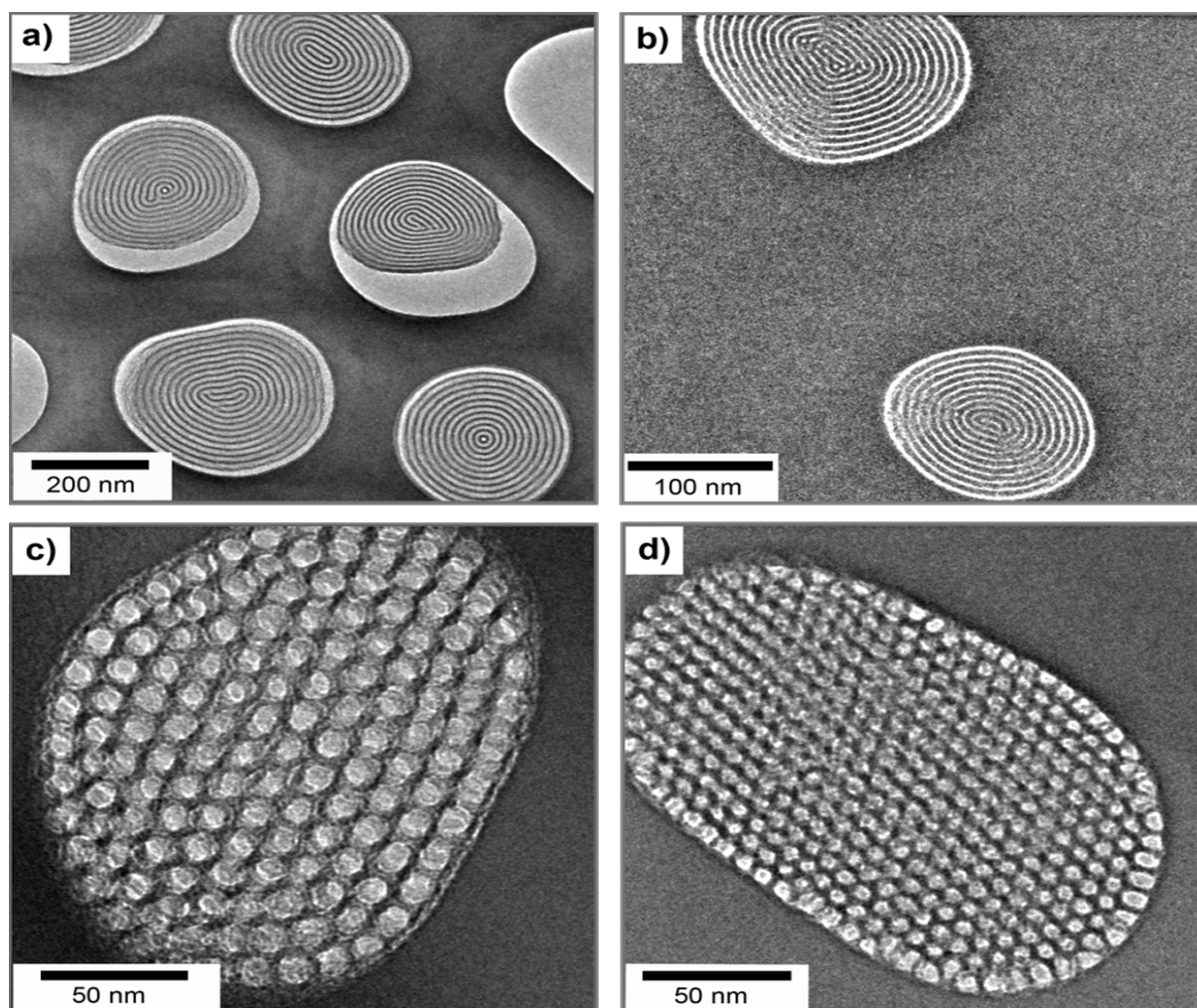
Figure 6.4: Plan-view TEM images of samples
     a) P-30,
     b) B-30,
     c) P-30-NaCl , and
     d) B-30-NaCl. Both reference samples in a) and b) show exclusively circular orientation of the mesostructure. Images c) and d) show the columnar hexagonal orientation present in the samples synthesized after addition of inorganic salt.

6.3 Influence of the anion

Different inorganic salts were used in the synthesis in order to study their effect on the orientation of the mesostructure in the confined space of the alumina channels. Focusing initially on the influence of the anion, we have examined a series of potassium salts with different counter ions. A diffraction pattern corresponding to a sample synthesized with addition of potassium chloride is shown in Figure 6.5 a. The oop:ip ratio of 0.1 reflects the

presence of mostly a columnar phase in the sample. Hence, the effect of sodium chloride and potassium chloride is comparable, although the SIPT seems to be more pronounced in samples synthesized with the smaller cation. Figure 6.5 b shows the diffraction pattern from a sample synthesized when the chloride of the salt was replaced by bromide. The oop:ip ratio of that sample is 0.2, but the signal-to-noise ratio is decreased compared to the sample synthesized with potassium chloride. When potassium iodide was added to the synthesis solution, no periodic structure was observed in the corresponding diffraction pattern (Figure 6.5 c). When the concentration of potassium iodide was decreased to 1/5 of the original amount, the corresponding diffraction pattern shows a slightly better ordered structure (Figure 6.5 d). Nevertheless, the sample is by far not as well organized as the ones synthesized with the smaller anions.
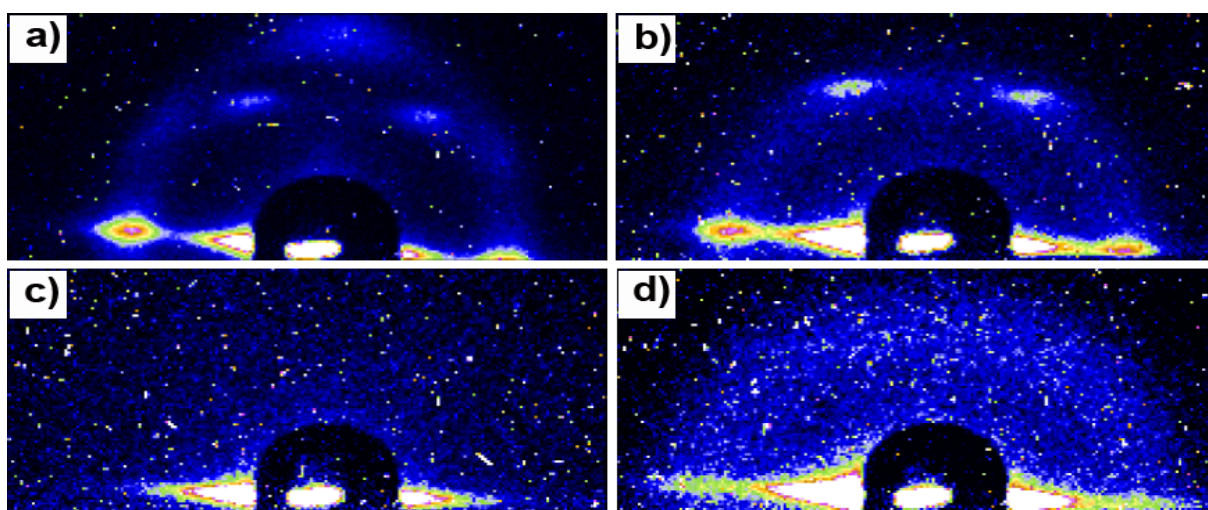
Figure 6.5: SAXS pattern from samples synthesized adding the same molar ratio (2 mmol per 10 mmol TEOS) of
a) potassium chloride (oop:ip = 0.1),
b) potassium bromide (oop.ip = 0.2), and
c) potassium iodide to the synthesis solution, and
d) from a sample synthesized with 0.4 mmol potassium iodide per 10 mmol TEOS.

6.4. Influence of the cation

In addition to the effect of the anions, a strong influence of the alkali cations in the salt was observed; the corresponding experiments were performed at elevated temperature (30 °C). With lithium chloride an almost complete transformation towards the columnar orientation

could be induced for both surfactants, leaving only negligible amounts of circular side phase. The corresponding reference samples P-30 and B-30 with mostly circular orientation have already been discussed above. Figure 6.6 a and 6.6 b show the diffraction pattern of the samples P-30-LiCl and B-30-LiCl, respectively. The oop:ip ratios derived from these patterns are 0.03 for P-30-LiCl and for B-30-LiCl, indicating a predominantly columnar orientation. The corresponding TEM images shown in Figure 6.6 c for P-30-LiCl and Figure 6.6 d for B-30-LiCl confirm the well organized columnar hexagonal arrangement of the mesophases.
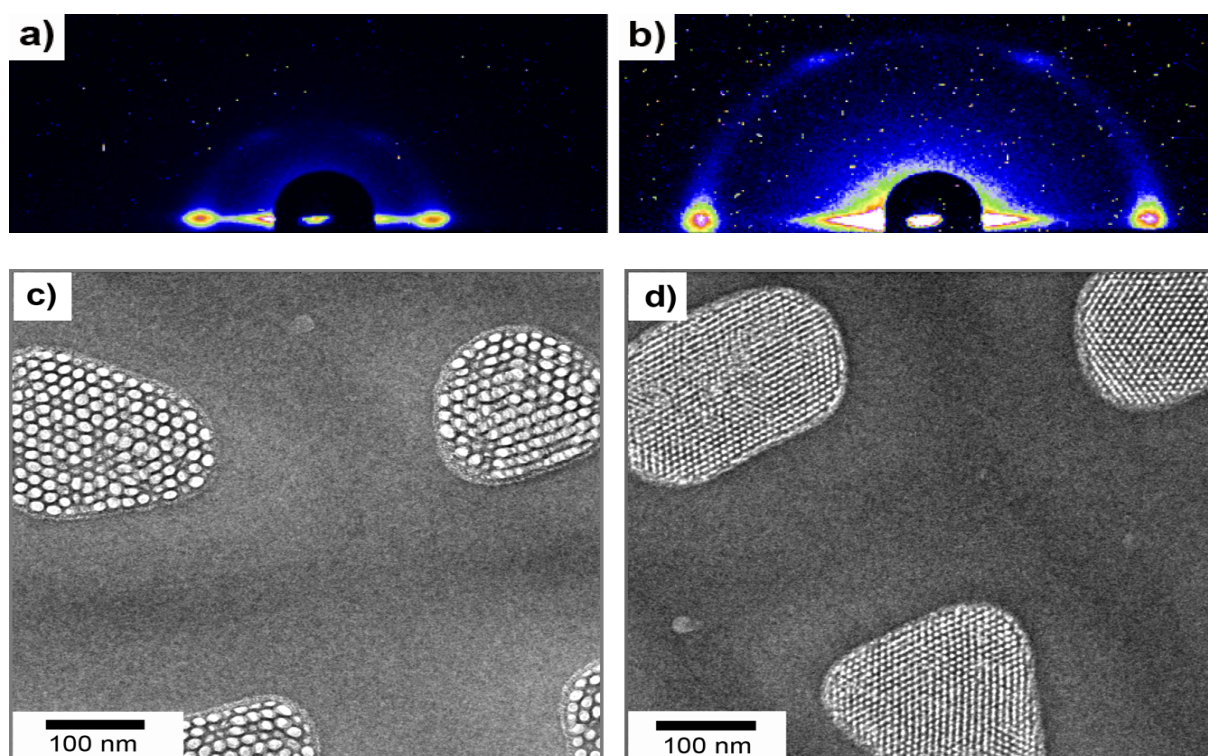
Figure 6.6: SAXS pattern of samples
      a) P-30-LiCl (oop:ip = 0.03), and
      b) B-30-LiCl (oop:ip = 0.03) synthesized at 30 °C. Plan-view TEM images of the samples
      c) P-30-LiCl, and
      d) B-30-LiCl showing pure columnar orientation of the mesostructure.

6.5. Influence of modification of the AAM surface

The interactions between the silica species and the alumina channel wall seem to be not only important for the formation of a certain orientation but also crucial for the formation of a mesostructure as such. When the surface of the AAM channels was made hydrophobic by modification with TMSCl, only unstructured material was found to form during EISA. Figure

6.7 a shows exemplarily the diffraction pattern of P-21-TMSCl. The diffraction pattern of the other samples listed in Table 6.1 look identical. No ring or reflections are visible in the diffraction pattern depicted showing the absence of structure. A corresponding TEM image is shown in Figure 6.7 b. There is some material visible within the AAM channel, but it is far from being mesostructured.
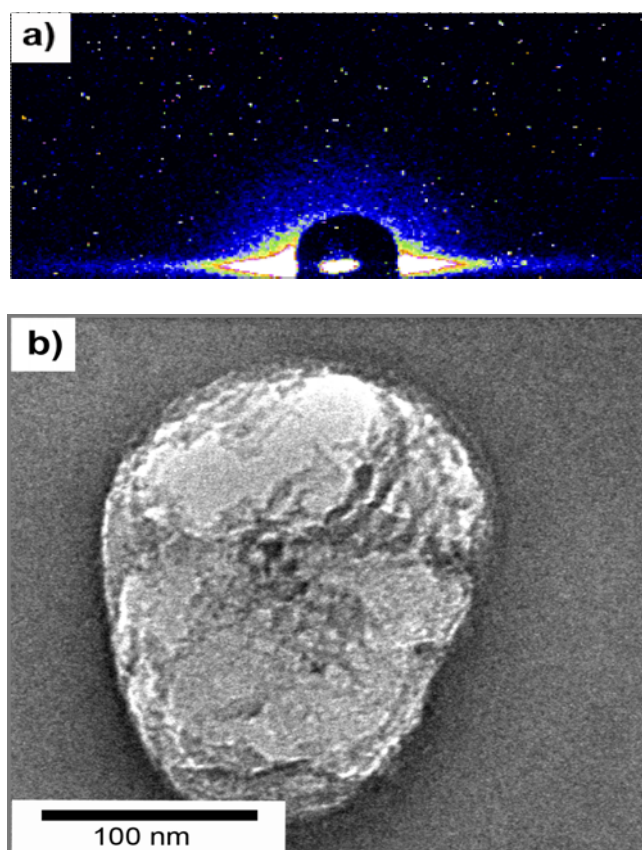
Figure 6.7: a) SAXS pattern from P-21-TMSCl, representative for all samples synthesized on modified AAMs.
b) corresponding TEM image from P-21-TMSCl confirming that no periodic material was formed inside the AAM channels.

6.6. Sample preparation

The synthesis solutions were prepared by mixing 2.08 g (10 mmol) tetraethoxysilane (TEOS), 1.8 g water, 3.0 g hydrochloric acid (0.2 molar), and 3.95 g ethanol in a polypropylene bottle. The TEOS containing solution was brought to 60 °C for 1h for pre-hydrolization. In another polypropylene bottle the respective surfactant (750 mg (0.13 mmol) P123 or 906 mg (1.33 mmol) Brij 56) was dissolved in 11.85 g ethanol. When cooled to room temperature, the

respective TEOS- and surfactant-containing solutions were combined and divided in two parts, one half serving as reference, the other used after addition of 1 mmol inorganic salt, respectively (58.5 mg NaCl, 42.5 mg LiCl, 74.5 mg KCl, 118 mg KBr, or 166 mg KI). The final synthesis solution has a corresponding salt:silica ratio of 0.2. For preparation of the sample P-21-KI*lc* only 33 mg KI (0.2 mmol KI) were used, corresponding to a salt:silica ratio of 0.04.

The AAMs were placed on a Teflon plate and 1 ml of each precursor solution was evenly spread on one AAM respectively and left to dry. Hydrophobization of the AAMs was carried out by heating the AAMs in 8 ml trimethylchlorosilane (TMSCl) at 70 °C under reflux for 7 h. If the temperature needed to be adjusted, the synthesis was carried out in an oven with adjusted relative humidity. The EISA process was carried out at two temperatures: 21 °C and 30 °C. The chosen difference of 9 °C between the synthesis temperatures is small enough to allow similar drying times.

7. Surfactant removal

7.1. Hexagonal phases

The embedded silica/surfactant nanocomposite mesophases obtained here differ significantly from those reported previously for confined polymer systems[26] in that the mesostructures discussed here form a rigid silica framework upon template removal, leaving solid supports with ordered porosity that can, for example, offer a matrix for the guided growth of a variety of conductive materials. The obtained hexagonal samples were stable upon calcination at 400 °C while the orientation was preserved (oop : ip ratios remain roughly at the same value before and after calcination). The diffraction patterns of calcined samples P-21-calc, P-30-calc, P-30-LiCl-calc, B-30-calc, and B-30-LiCl-calc are shown in Figure 7.1.
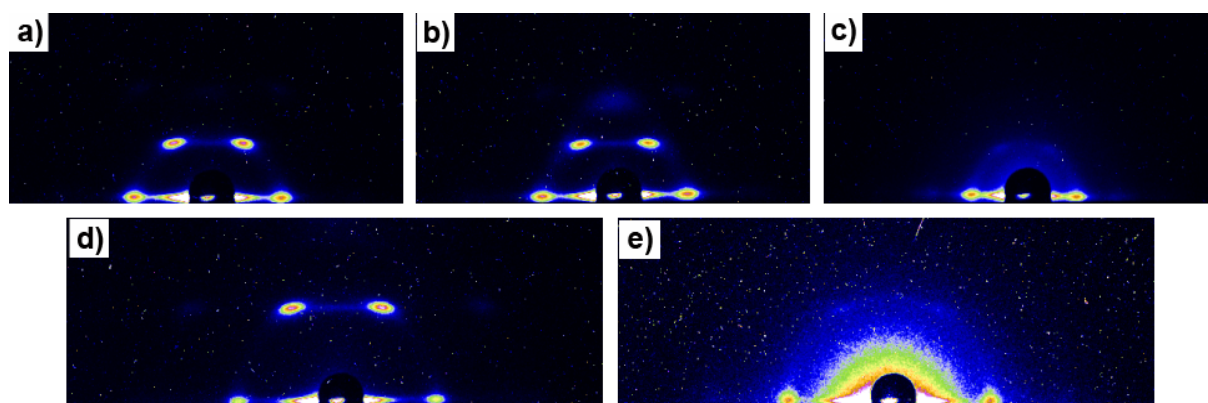
Figure 7.1: SAXS pattern of the samples
      a) P-21-calc (oop:ip = 0.7),
      b) P-30-calc (oop:ip = 0.5),
      c) P-30-LiCl-calc (oop:ip = 0.03),
      d) B-30-calc (oop:ip = 1.0), and
      e) B-30-LiCl-calc (oop:ip = 0.04) after calcination at 400 °C. Structure and orientation is maintained.

A list of the calcined samples, their d-spacing calculated from the respective diffraction patterns, and their oop:ip ratios is given in Table 7.1. The sample names are given as in the last chapter, first the used surfactant (B for Brij 56, P for P123), second the synthesis temperature (21 °C or 30 °C), third the sum formula of the added salt, if any. The index calc denominates calcined samples.

Table 7.1: Summary of the data from the calcined samples: Sample name, q-vector, d-spacing calculated from q, and the oop:ip-ratio of reflections from the respective diffraction patterns.

Sample name	Scattering vector q /nm^{-1}	d-spacing /nm	oop:ip ratio
P-21	0.62	10.2	0.7
P-21-calc	0.74	8.5	0.7
P-30	0.62	10.2	0.5
P-30-calc	0.74	8.5	0.5
P-30-LiCl	0.56	11.2	0.03
P-30-LiCl-calc	0.55	11.5	0.03
B-30	1.05	5.9	1.0
B-30-calc	1.04	6.0	1.0
B-30-LiCl	1.06	5.9	0.03
B-30-LiCl-calc	1.04	6.0	0.04

It is noticeable, that the calcined samples P-21-calc and P-30-calc exhibit smaller d-spacing after calcination due to shrinkage after template removal. In contrast to that the d-spacings calculated from the diffraction patterns for the uncalcined and calcined sample P-30-LiCl-calc are almost identical (see Table 7.1). This observation is confirmed by TEM imaging (Figure 7.2). Figure 7.2a shows a corresponding micrograph of sample P-30-calc, an image of sample P-30-LiCl-calc is depicted in Figure 7.2 c. While in sample P-30-calc a set of nine pores is about 100 nm wide, in sample P-30-LiCl-calc a 100 nm distance corresponds to a set of six pores.

It is well-known that mesoporous films tend to shrink in the direction normal to the substrate surface when they are calcined, resulting in elliptically deformed pores. In the confined environment of the AAM channels the mesoporous material is connected to the alumina channel wall at all sides throughout a length of about 60 microns, corresponding to the thickness of the AAM. Shrinkage in these systems therefore causes fracture and/or separation from the AAM channel walls. This effect is also observed for uncalcined samples that are shrinking due to further drying of the pre-structured material. Some TEM images show cases where the mesostructured material is detached from one side of the alumina channel wall, but

still mimicking the shape of the AAM channel (section 3.5: Figures 7.2 a, b, 7.2 d, 7.6 a). The location, where the mesoporous material detaches from the AAM channel wall is random. Pronounced shrinking of the structure in sample P-30-calc is not only indicated by the corresponding diffraction pattern (Figure 7.1 b, Table 7.1), but is directly observed by detachment of the mesoporous fibers from the AAM channel walls in the TE micrograph of this sample (Figure 7.2 a).

In contrast to the above, it was observed that the columnar phases prepared with the inorganic salts remain attached to the AAM channel surface. Self-assembly within an AAM channel forces the silica-template-composite to mimic the channel shape. Comparing as-synthesized and calcined samples, the mesopore diameter shows some variations in the as-prepared sample P-30-LiCl (Chapter III, Figure 6.6). The material is apparently flexible enough to form slightly smaller or bigger silica rods to meet the geometric requirements in the confined space. After calcination, the silica phase is much more condensed. The TEM images now show a very regular mesopore structure with consistent pore diameters, and the mesostructure does not fit the alumina channel as perfectly as before calcination (Figure 7.2). The average d-spacing represented by the diffraction pattern seems to be unaffected by these small rearrangements. The absence of shrinkage and separation suggests that the inorganic ions increase the chemical interactions between the silica mesophase and the AAM channel surface.
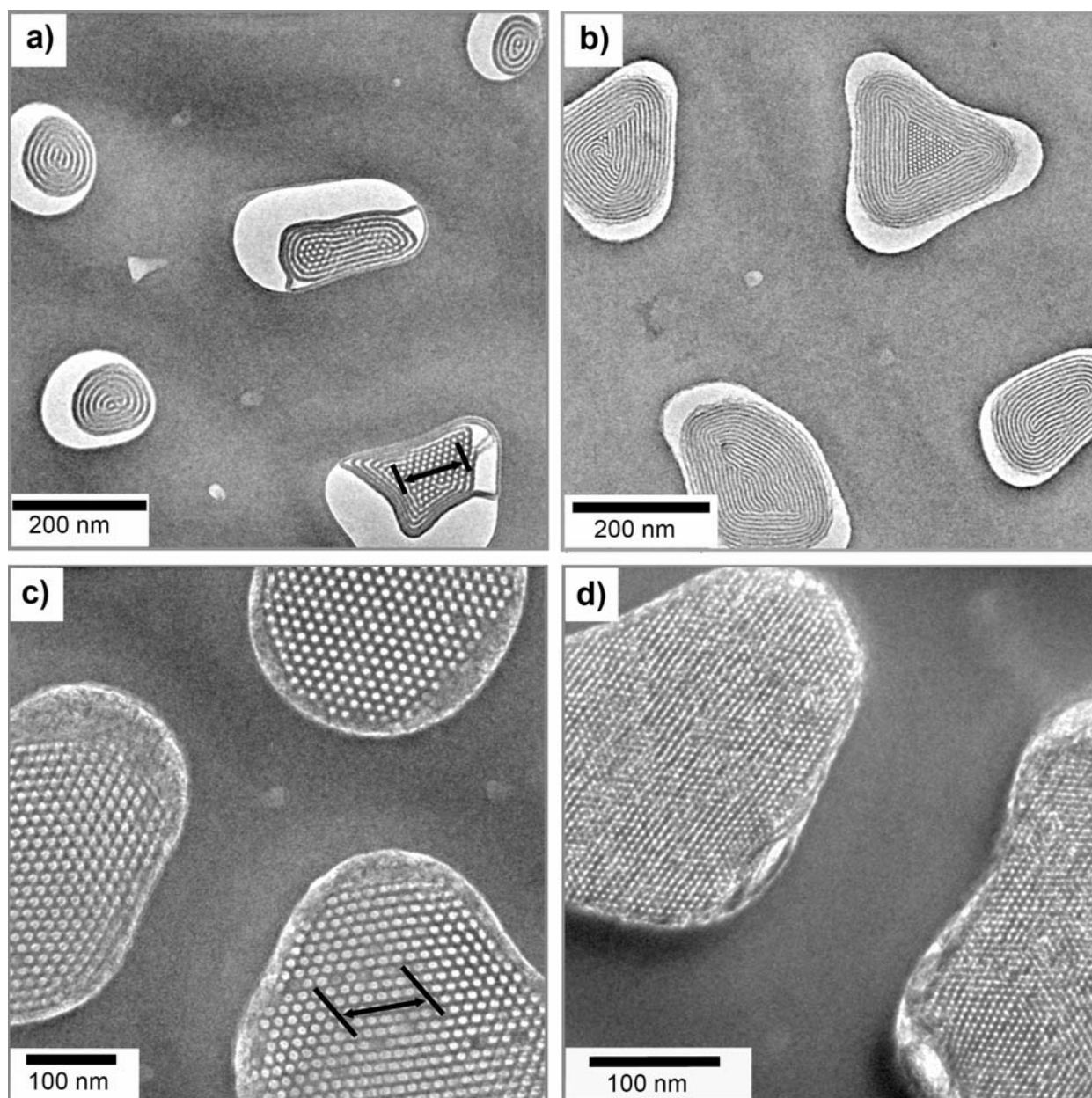
Figure 7.2: Plan-view TEM images of the calcined samples
       a) P-30 (inset scale is 100 nm, corresponding to about 9 pores),
       b) B-30,
       c) P-30-LiCl, and
       d) B-30-LiCl (inset scale is 100 nm, corresponding to about 6 pores). The reference samples show mostly circular orientation and shrinkage of the structure. The samples synthesized with salt exhibit columnar orientation and attachment to the alumina channel wall through an amorphous layer.

This is supported by another characteristic of the calcined samples synthesized with lithium chloride. It is clearly visible in Figure 7.2 c that there is an amorphous layer of material between the mesostructured silica phase and the surface of the AAM channel. That amorphous layer is as thick as up to three times the pore diameter of the mesophase. The same is visible in Figure 7.2 d for the sample synthesized with Brij 56. The TEM images of the

uncalcined samples synthesized with salt depicted in Chapter III, Figure 6.6 already show a thin amorphous layer at the mesostructure-AAM-interface. It is supposed that this layer is composed of silica covering the surface of the AAM channels. This silica layer apparently is expanded during calcination while the mesophase is getting tighter and more organized, possibly filling the gap between mesostructure and AAM channel surface. Such a pronounced layer of amorphous silica is not visible in calcined samples with circular structures prepared without the addition of inorganic salt. Instead, in those samples the silica mesophase tends to detach from the alumina wall leading to large gaps between the wall and the mesostructure. This is an important aspect regarding potential applications of these composite membranes, e.g., as templates for the growth of nanowires. For such applications, it is often essential that the AAM channels are completely filled with material.

7.2. Sorption measurements

Nitrogen adsorption/desorption isotherms and respective pore size distribution curves of calcined samples B-30-calc, B-30-LiCl-calc, P-21-calc, P-30-calc, and P-30-LiCl-calc are shown in Figure 7.3. Sample B-30-calc exhibits circular orientation of the hexagonal phase, P-21-calc and P-30-calc show oop:ip-ratios of 0.7 and 0.5 corresponding to circular – columnar phase mixtures, respectively, The samples synthesized with LiCl (B-30-LiCl-calc, P-30-LiCl-calc) represent pure columnar hexagonal structures. All samples show Type IV isotherms including the monolayer-multilayer adsorption and capillary condensation. Hysteresis loops are observed in the adsorption and desorption cycle around the capillary condensation, typical for mesoporous materials with cylindrical mesopores.
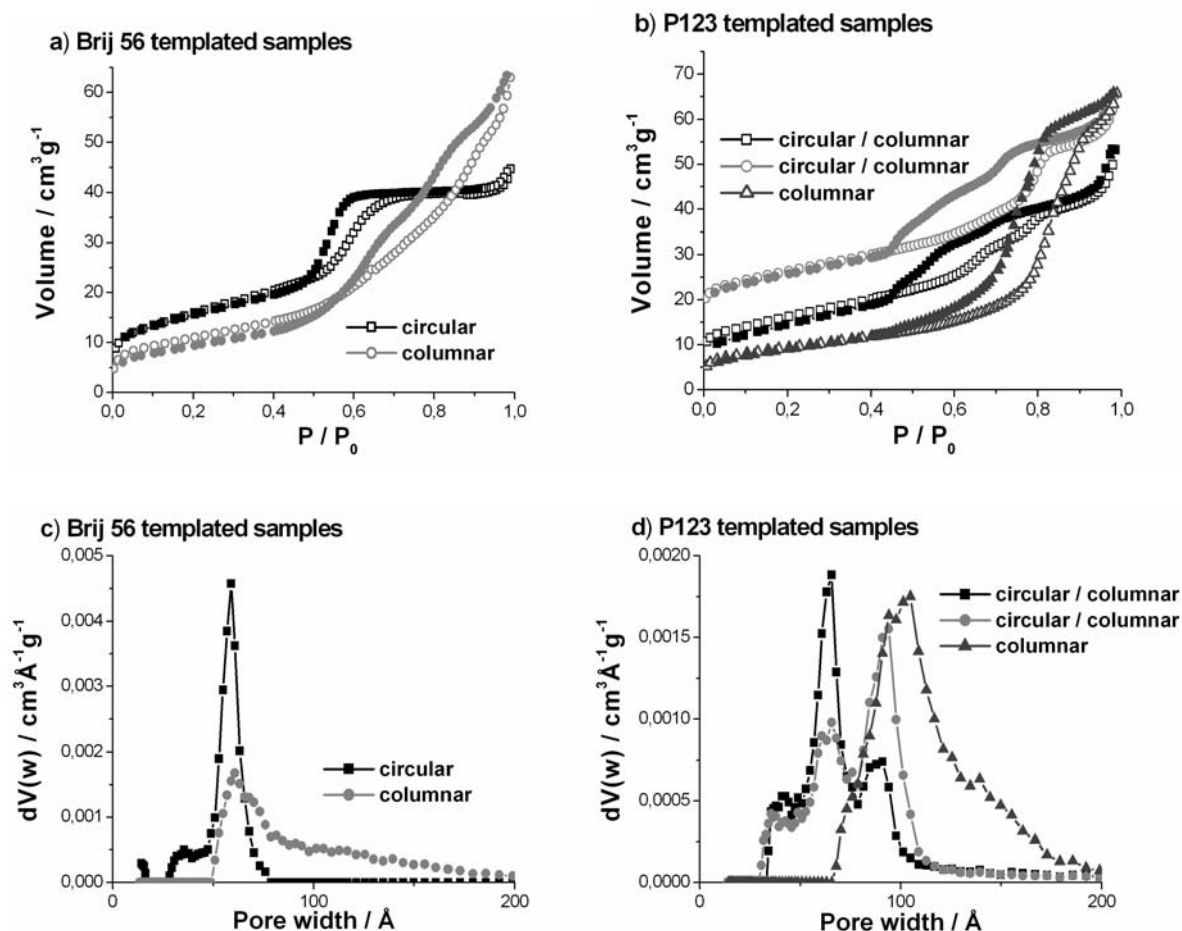
Figure 7.3: Nitrogen adsorption/desorption isotherms and the respective pore size distributions based on the adsorption branch and the DFT method of the samples
        a), c) B-30-calc (circular), B-30-LiCl-calc (columnar), and
        b), d) P-21-calc, and P-30-calc (circular / columnar phase mixture),
          and P-30-LiCl-calc (columnar).
Open symbols represent the adsorption branch, the desorption branch is represented by filled symbols. The isotherms from B-30-LiCl-calc and P-30-calc are vertically offset by 5 cm³/g, the isotherm of P-20-calc is offset by 15 cm³/g, respectively.

Specific surface areas calculated by the BET method and pore diameters corresponding to the maxima in the respective pore size distribution curves are given in Table 7.2 for each sample. The pore size distributions are calculated based on the adsorption branch and the DFT method. A bimodal pore size distribution is observed in most of the samples. Interestingly, the different pore diameters correlate with the different phases (circular vs. columnar) formed with the same surfactant. While distribution curves for circular samples exhibit narrow peaks at smaller pore diameters, the peaks are broadened and shifted to higher values in the columnar phases. In sample B-30-calc, which is a Brij 56 templated sample with circular

122

orientation, one comparatively sharp peak with a maximum at 5.9 nm pore diameter is visible, while the sample B-30-LiCl-calc which has pure columnar orientation exhibits two broad overlapping peaks with maxima at 6.1 and 6.8 nm pore diameter and an additional streak ranging from 8 to 18 nm.

Table 7.2: Sorption characteristics of circular and columnar samples prepared with Birj 56 and P123 and a P123 templated sample exhibiting a circular – columnar phase mixture.

Sample name	oop:ip-ratio	Specific surface area / m^2g^{-1}	Pore diameter / nm
P-21	1	41	6.6, 9.1
P-30	0.7	41	6.6, 9.5
P-30-LiCl	0.002	33	10.4 (and streak)
B-30	1.3	56	5.9
B-30-LiCl	0.01	39	6.1 (and streak)

A similar effect is observed in samples synthesized with P123. The mostly circular structure (P-21-calc) shows a bimodal pore size distribution with two comparatively narrow peaks having maxima at 6.6 and 9.1 nm pore diameters. The peak at larger pore size is much smaller than the one at 6.6 nm. The pore size distribution curve of P-30-calc with a larger fraction of a columnar phase shows again two peaks at 6.6 and 9.5 nm. In this case, the second peak is higher than the first one and shifted to slightly higher pore diameter. The pure columnar structure found in P-30-LiCl-calc shows only one broad peak with a maximum at 10.4 nm pore size plus a shoulder ranging from 13 to 18 nm. Thus, the smaller pore size at 6.6 nm is attributed to the circular phase, while the columnar phase formed in the same sample exhibits larger pore diameters of about 9 nm.
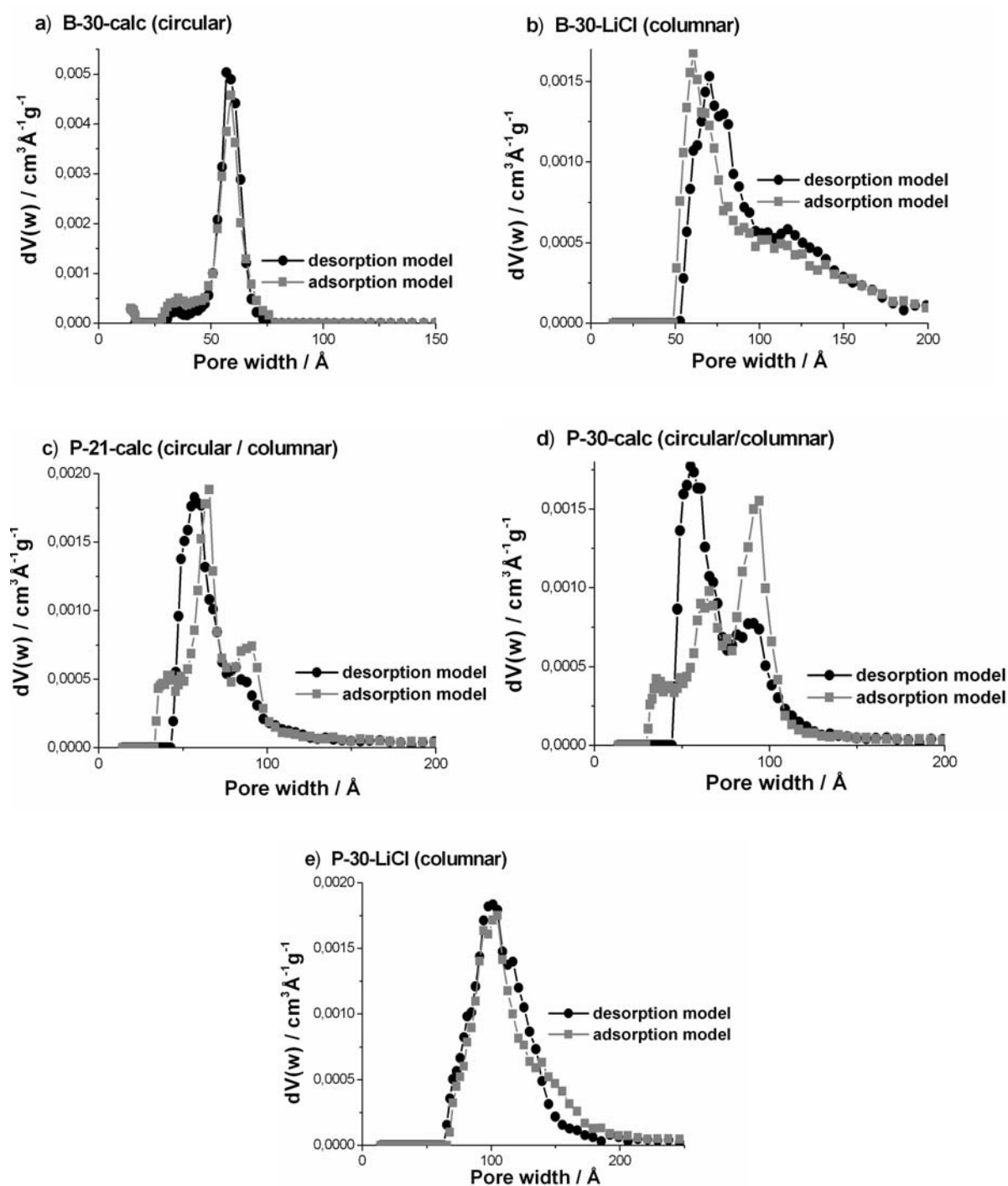
Figure 7.4: Pore size distributions calculated based on the DFT method from the adsorption branch in comparison to pore size distributions calculated from the desorption branch of the samples
  a) B-30-calc (circular),
  b) B-30-LiCl-calc (columnar),
  c) P-21-calc (circular),
  d) P-30-calc (mixture), and
  e) P-30-LiCl-calc (columnar).

The samples P-21-calc and P-30-calc both exhibit a mixture of the columnar and circular phase, P-30-calc showing a larger fraction of columnar structure as extracted from the

respective oop:ip ratios. This trend corresponds exactly to what is concluded from the sorption data of these samples. Furthermore, the sorption data show that both pore systems are interconnected. The pore size distribution curves calculated from the adsorption and desorption branch of the isotherms (Figure 7.4) are the same when calculated from the samples exhibiting a pure circular (B-30-calc) or pure columnar phases (B-30-LiCl-calc, P-30-LiCl-calc). However, when pore size distributions are calculated from the samples exhibiting a circular – columnar phase mixture (P-21-calc, P-30-calc), a significantly higher volume fraction of the smaller pore diameters is calculated from the desorption branch compared to the adsorption branch. This is typical for blocking of pores with the larger diameters by pores with a smaller diameter, thus the different phases appear to be interconnected.

A broader pore size distribution with a tail to larger diameters is observed in any case for the pure columnar phases obtained upon addition of salt. The tails between 8-18 nm in sample B-30-LiCl-calc and 13-18 nm in sample P-30-LiCl-calc are attributed to possible pore-merging. TEM images of other locations of the calcined samples reveal that there are some areas where the silica walls between the mesopores are ruptured and pores are merged (Figure 7.5). Larger pore diameters and the merging of pores support the earlier statement that the interactions of the mesophase with the alumina channel wall are increased due to addition of inorganic salt. Pore merging is also indicated by the lower specific surface area found in both samples synthesized with salt. In the circular phase, mechanical stress during template removal leads to detachment from the channel walls, while the columnar phase remains attached to the alumina showing larger pore diameters, and in some cases rupture of the silica walls (see examples depicted in Figure 7.5).
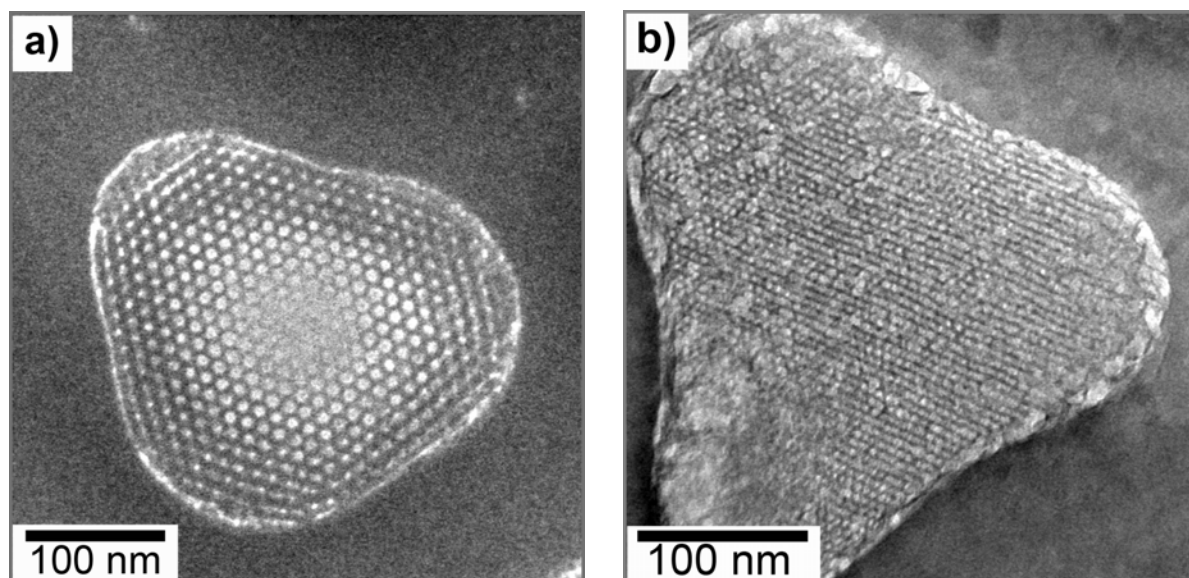
Figure 7.5: TEM images of the calcined samples P-30-LiCl [a)] and B-30-LiCl [b)] showing rupture of silica walls and merged mesopores.

7.3. Tubular lamellar phase

Calcination of the tubular lamellar phase is more difficult due to the lack of 3-dimensional connection of the pore system. In conventional lamellar mesostructured powders, calcination is not possible without collapse of the structure. In contrast to that, the tubular lamellar structures synthesized in this work might be more stable upon template removal, because the silica sheets are rolled up into long cylindrical objects. The diffraction pattern and representative TEM images of a lamellar sample before and after calcination at 400 °C are shown in Figure 7.6. No distinct diffraction spots could be anymore observed after calcination (Figure 7.6 b). However, the TEM images of the as-synthesized and calcined samples look similar showing distorted large cylindrical objects (Figure 7.6 c, d). It has been demonstrated in the previous chapters that the circular lamellar phase collapses when irradiated with the electron beam. Thus, similar processes might happen during calcination. The material does not completely collapse upon radiation, and it does not condense into dense material as in conventional lamellar phases. However, the material has lost its periodicity and monomodal porosity upon calcination.
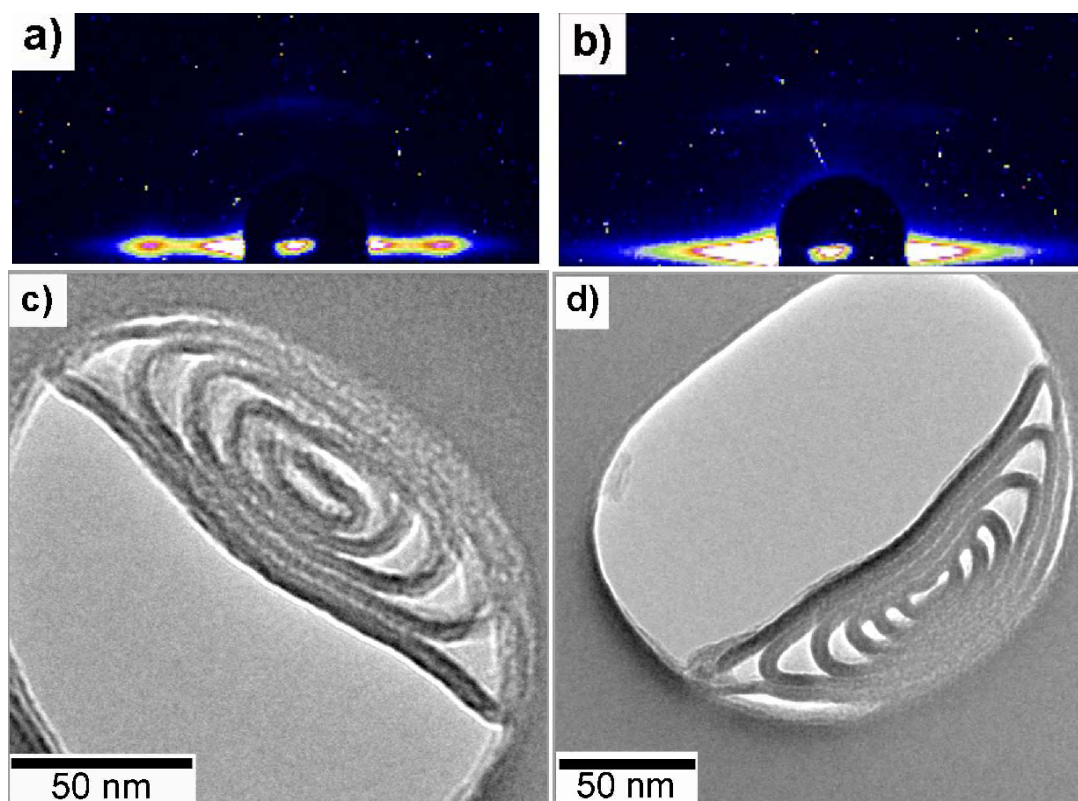
Figure 7.6: SAXS pattern of
a) as-synthesized sample exhibiting lamellar phase
b) lamellar sample after calcination at 400 °C showing no distinct reflections
Representative TEM images of
a) as-synthesized lamellar sample
b) calcined lamellar sample showing distortion of the structure.

7.4. Calcination procedure

The samples were calcined at ambient atmosphere with a heating rate of 2 min per °C and several annealing steps (10 h at 120 °C, 5 h at 220 °C, and 5 h at 400 °C).

8. Exploration of nanostructured channel systems with single molecule probes

In this section it is shown how single molecule fluorescence microscopy serves to track individual dye molecules inside the pores of periodic mesostructured silica. The extremely long trajectories with high statistical quality give, for the first time, a detailed picture of the structure and connectivity of different pore systems. An advantage of this technique is that contrary to the statistical averaging of X-ray scattering experiments, the fluorescent dyes ("molecular beacons") directly trace out in striking detail the 'landscape' of the inner pore system of the host. Much larger areas may be sampled than in TEM, without special sample preparation. Furthermore, a detailed view of the dynamics of the guest molecules inside the porous host is gained.

This work was established in cooperation with Johanna Kirstein and Christophe Jung from the research group of Prof. Bräuchle at LMU. The single molecule fluorescence microscopy was done by Johanna and Christophe; details about this part of the work may be found in their theses and in corresponding publications.[12,27-29] The present thesis is focused on the preparation of the samples and characterization with conventional methods (diffraction, electron microscopy). The results of the single molecule tracing work will be briefly discussed here; the corresponding figures will be marked with an asterisk.

Two approaches were simultaneously developed in our group to provide proof that single molecule fluorescence microscopy reflects the structural features of the mesostructured host. On the one hand, ultra-thin mesostructured silica films with 2D hexagonal phase were prepared and investigated with fluorescence microscopy followed by mapping of the structure with TEM at the same position and direct correlation of the structure pattern with the observed trajectories of fluorescent dye molecules.[29] On the other hand, an indirect

correlation of diffusion and structure was performed. Different diffusional and orientational dynamics of molecules were observed in different structures synthesized with various amounts of the same organic template. This was reflected in samples with pure phases (lamellar and 2D hexagonal) as well as for samples exhibiting phase mixtures.[12] The orientation of molecules could also be measured in silica material with columnar mesostructure (CTAB templated) embedded in AAM channels. The advantage of this approach is that the orientation of the cylindrical silica rods is known on a macroscopic scale for these composite materials.

Mesostructured silica fibers inside the channels of AAMs were produced according to the method described in Chapter II, Section 1. Flat films were prepared *via* spin-coating of similar precursor solutions on glass slides resulting in thin silica layers with a thickness of about 200 nm (Chapter II, Section 2). Strongly fluorescent terrylenediimide molecules[30] (TDI, Figure 8.1), acting as molecular beacons, were added at very low concentrations to the synthesis solutions (10^{-8} mol/l). The dimension of the TDI molecule is about 1 x 1 x 3.2 nm^3. During evaporation-induced self-assembly the dye molecules are located in the non polar environment of the surfactant micelle centers and thus are incorporated into the pores of the mesostructured silica. Single molecule fluorescence microscopy was carried out on the as-synthesized films without further sample preparation. Here the term "pore" that classically defines the empty space in porous materials after removal of the organic template is used to describe the template-filled space where the dye molecules are moving.
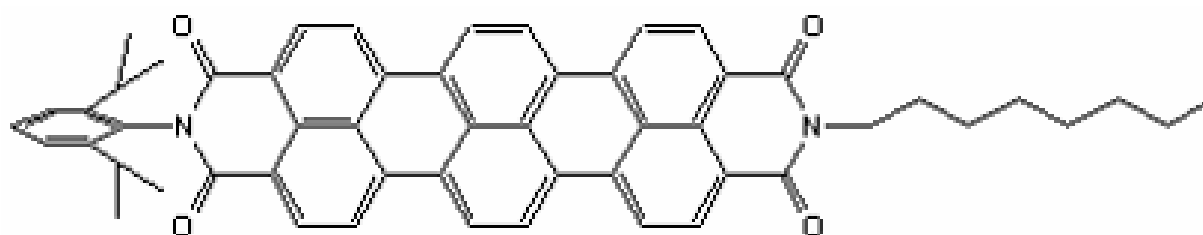
Figure 8.1*: TDI molecule, about 1 nm high and wide, and 3 nm long.

8.1. Brij 56 thin films

Films with various Brij 56 : silica ratios ranging from 0.033 to 0.715 were prepared. X-ray diffraction in Bragg-Brentano geometry revealed that different phases were formed depending on that ratio. The respective diffraction patterns are depicted in Figure 8.2 a-c. At low surfactant concentrations, only amorphous phase was obtained, exhibiting mainly a shoulder around 1.6 °2θ. With increasing amount of template in the precursor solution a peak evolves at the same 2θ value. Further increase of the Brij 56 : silica ratio leads to the formation of a more pronounced peak indicating increasing order (Figure 8.2 a). If the surfactant : silica ratio is higher than 0.1, a second phase starts to form, indicated by a shoulder at 1.45 2θ that successively gains intensity and forms a second peak when the concentration of template is further increased (Figure 8.2 b). At Brij 56 : silica ratios of 0.2 or higher the intensity of the peak at 1.6-1.7 2θ is decreasing until is becomes a shoulder of the peak at 1.45 2θ and finally vanishes completely (Figure 8.2 c). It is concluded that two different phases are present in the films, one formed at surfactant : silica ratios lower than 0.1 and a second phase formed at Brij 56 : silica ratios higher than 0.27. With intermediate ratios the formation of mixed phases was observed.
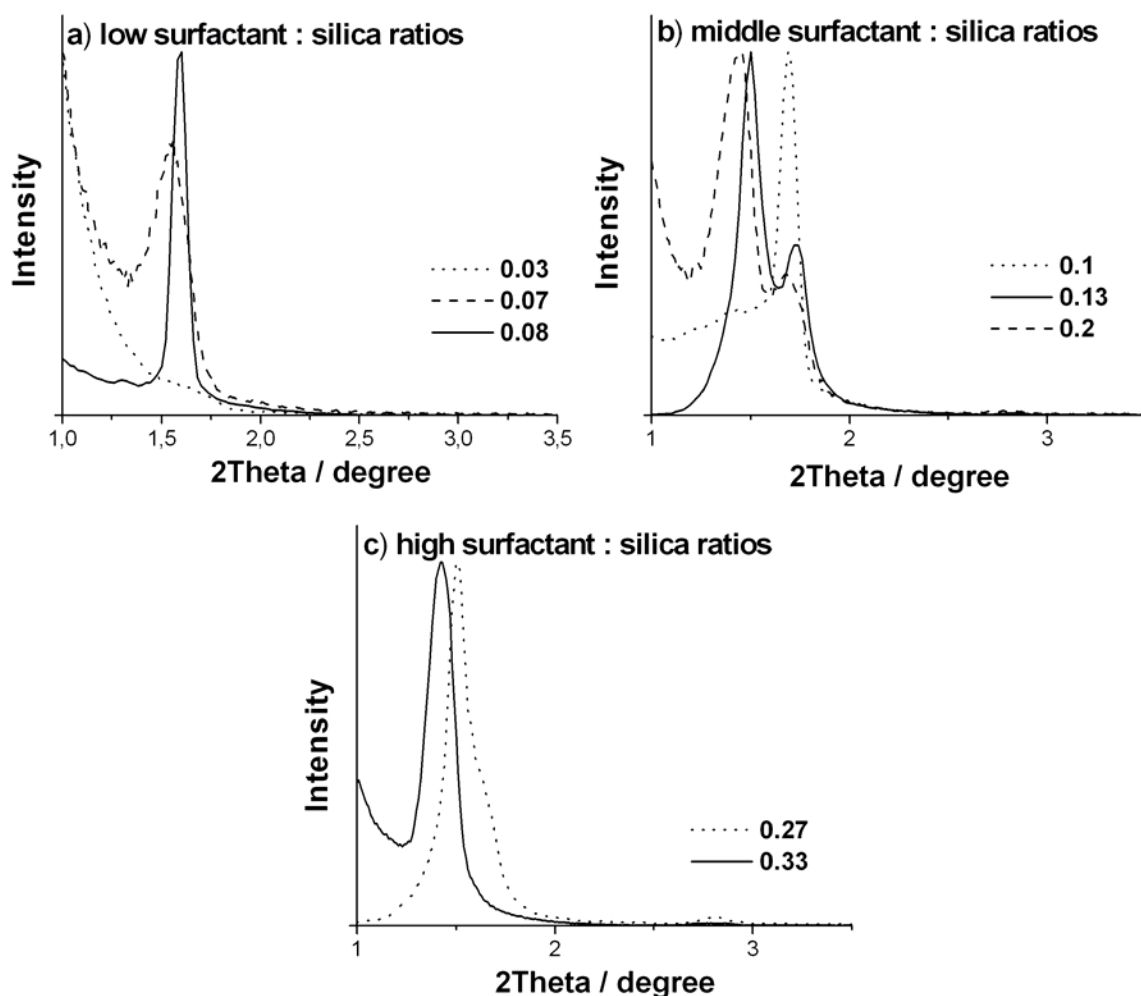
Figure 8.2: XRD patterns of samples prepared with different Brij 56 : silica ratios detected in a Bragg-Brentano geometry. At low surfactant : silica ratios a 2D hexagonal phase is formed, intermediate Brij 56 concentrations lead to the formation of a hexagonal / lamellar phase mixture, and at high surfactant : silica ratios a pure lamellar phase is formed.

An overview of the different surfactant : silica ratios, the peaks observed in the respective diffraction patterns, and the corresponding d-spacings calculated from the 2θ values is given in Table 8.1. The two d-values calculated for the different structures are around 5.5 nm and around 6.2 nm, respectively. The d-spacing of the phase formed at comparatively low surfactant concentrations is by a factor sin(120°) smaller than that of the other structure. This is indicative for the formation of a hexagonal and a lamellar phase, respectively (Chapter II, Section 3.1.) with both phases having roughly the same pore-to-pore distance (6.2 nm and 6.35 nm). It is known from the literature that the pore wall can amount up to 30 percent of the pore-pore distance in such mesoporous samples.[31] We can therefore give an estimate of

4 nm-5 nm for the distance between the silica walls. It is difficult to measure this value exactly in as-synthesized samples like the ones used in the measurements presented here.

Table 8.1: 2θ Positions of the observed first order peaks for the different surfactant : silica ratios and corresponding d-spacings. The bold-printed samples are investigated with fluorescence microscopy.

Brij 56 : silica ratio	Diffraction peaks detected /2θ	d-spacing /nm
0.03	Shoulder at 1.6	5.5
0.07	Weak peak at 1.54	5.7
0.08	**Peak at 1.6**	**5.5**
0.1	Peak at 1.69, shoulder at 1.45	5.2, 6.1
0.13	**Peaks at 1.7 and 1.5**	**5.2, 5.9**
0.2	Peaks at 1.69 and 1.45	5.2, 6.1
0.27	shoulder at 1.65, Peak at 1.5	5.3, 5.9
0.33	Peak at 1.42	6.2
0.4	**Peak at 1.4**	**6.3**
0.715	Peak at 1.41	6.3

TEM cross-section images were taken from samples with a Brij 56 : silica ratio of 0.08, 0.13, and 0.4, respectively. While the hexagonal pattern is observed in the representative micrograph in Figure 8.3 a, a line pattern coming from silica lamellae viewed from the side is observed in Figure 8.3 c. In Figure 8.3 b a mixture of line and hexagonal patterns is visible. Thus, the structures formed in the films are characterized as hexagonal, lamellar, or phase mixtures of both.
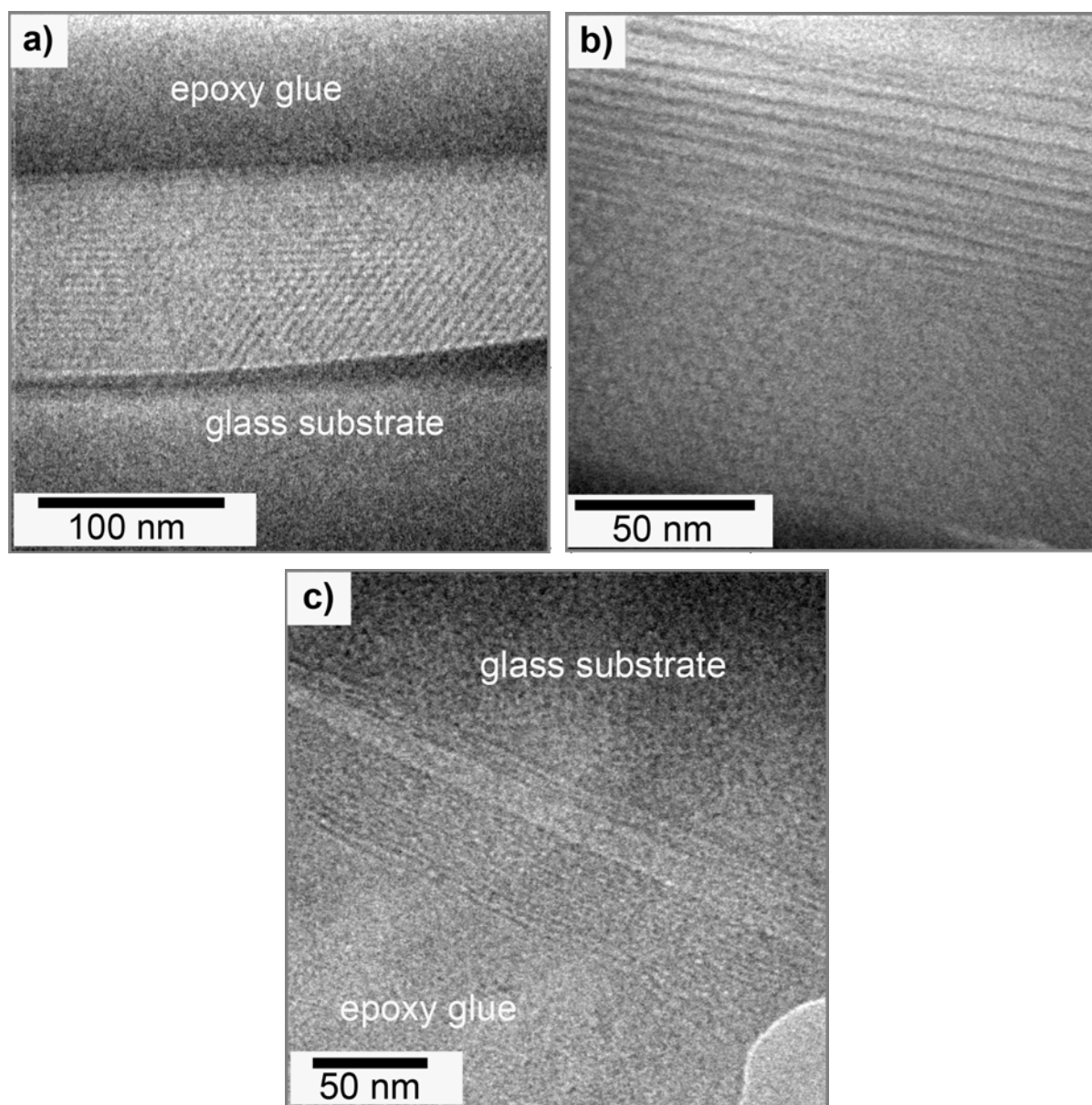
Figure 8.3: The cross-section TEM of the pure phases show the hexagonal arrangement of the silica rods [a), Brij 56 : silica = 0.08] and stacking of the lamellae [c), Brij 56 : silica = 0.4]. The image of the phase mixture [b), Brij 56 : silica = 0.13] displays hexagonal rods and lamellae stacked on top of each other. Different stacking orders can be observed in other areas of this sample.

While a combination of diffraction measurements and TEM is often sufficient to characterize the structure types, it is difficult to judge the size of domains with one phase and/or orientation, because they are bigger than the areas imaged in the TEM cross sections. Furthermore, the TEM images give no information about the real connectivity of the pores for molecules diffusing inside. Single molecule fluorescence microscopy overcomes these limitations and provides a detailed picture of the local structure of the host, its domains and the accessibility as well as the connectivity of the channel system.

The fluorescence of the single molecules in as-synthesized films was collected in an Eclipse TE200 (Nikon) epifluorescence microscope and detected with a highly sensitive CCD camera in a widefield imaging setup. No further sample preparation was needed. Since the films were much thinner than the focal depth of the microscope objective used (> 1 μm), the images contain data from molecules at all heights inside and on the surface of the sample. Series of 1000 images were acquired. In each image the single molecules show up as bright spots on a dark background. Their positions were obtained by fitting theoretical diffraction patterns to the spots with a positioning accuracy of up to 10 nm. Single molecule trajectories were then built up by tracking spots from frame to frame.

In the following is demonstrated that the different pore topologies of the hexagonal or lamellar phases strongly influence the diffusion of the molecules. Fluorescence images of samples exhibiting the pure hexagonal phase, the pure lamellar phase, and a mixture of both are shown in Figure 8.4 a, b, and c, respectively. In the widefield images of the hexagonal phase only Gaussian-shaped diffraction patterns are observed, whereas the fluorescence from single molecules in the lamellar phase appears as doughnut-shaped patterns. The molecules with doughnut shaped patterns show diffusion on a much longer timescale than the Gaussian-shaped patterns observed in the hexagonal phase. During the same time interval (500 ms) doughnut patterns diffuse in areas smaller than 1 μm, while the Gaussian patterns explore areas over distances of several microns.
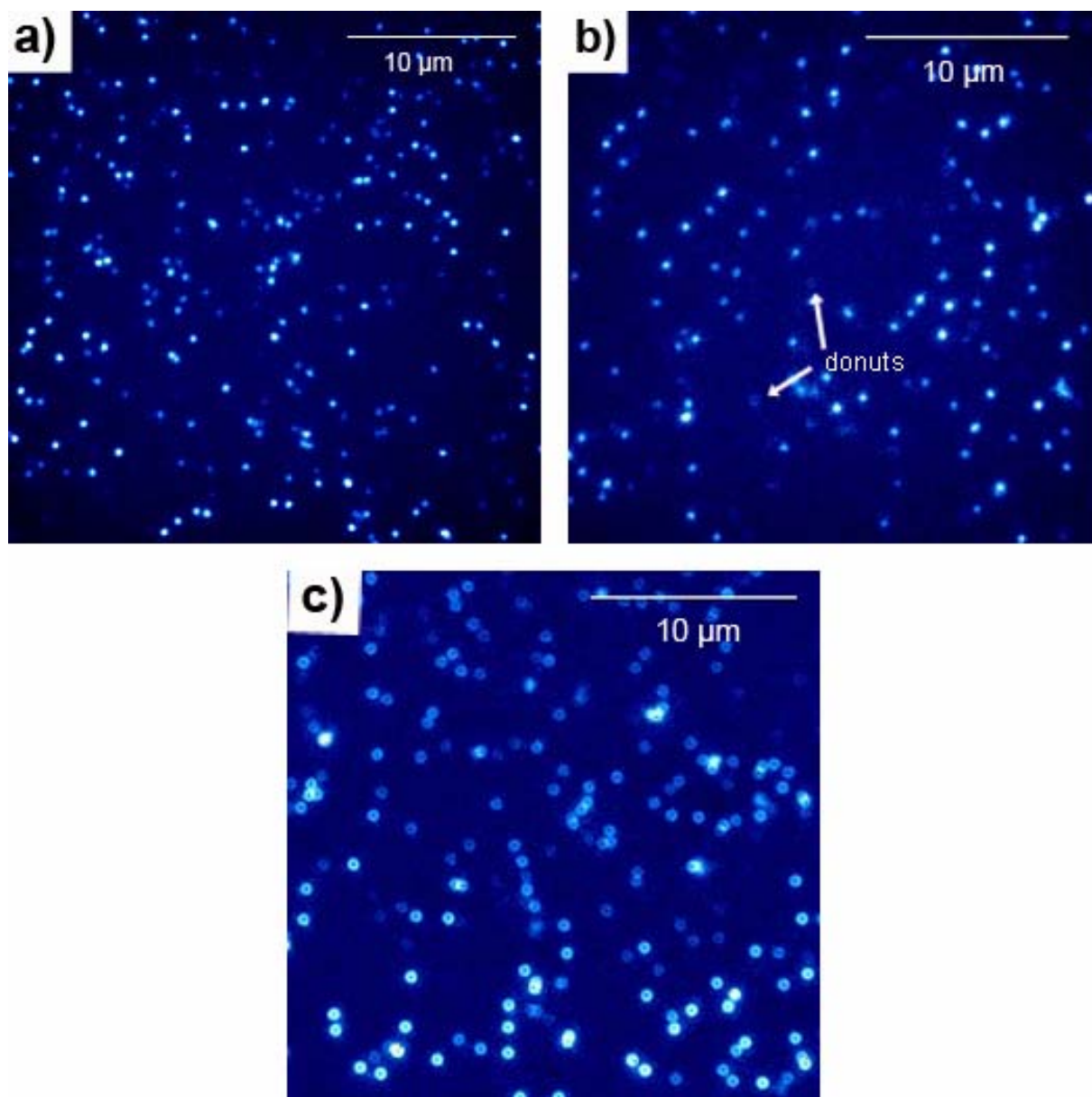
Figure 8.4*: Single molecule images and trajectories of the pure hexagonal and lamellar phases of the mesoporous hosts obtained by widefield imaging. The temporal resolution for the film of the pure hexagonal phase [a)] and the phase mixture [b)] was 500 ms / frame and for the lamellar phase [c)] 8 s / frame. The single molecule images in the hexagonal phase show only Gaussian-shaped diffraction patterns [a)] wheras in the lamellar phase only doughnut shaped patterns [c)] are observed. The phase mixture shows both Gaussian- and doughnut-shaped diffraction patterns [b)].

Doughnut diffraction patterns have been previously assigned to single molecules with their transition dipoles (here the long molecular axis of TDI) aligned along the optical axis of the microscope.[32] In the present case this implies that molecules in the lamellar phase are oriented perpendicular to the glass substrate and thus normal to the silica planes of the lamellar phase.

In addition to the translational diffusion, polarization dependent confocal microscopy can provide information about the orientational dynamics of the TDI molecules inside the surfactant filled pore systems (see Chapter III, Section 8.2). Such measurements show that the molecules in the lamellar phase maintain a constant orientation during diffusion in agreement with the observed doughnut patterns, whereas the molecules in the hexagonal phase constantly reorient on a timescale below 300 ms.

The ordered state of the molecules in the lamellar phase and the slow diffusion observed for these oriented molecules indicate a strong interaction between hydrophobic dye and amphiphilic template. Continuous reorientation and comparatively fast diffusion of the dye indicate much weaker interactions with the template in the hexagonal phase. Since the chemical composition of silica and template is identical in both structures and pore diameters are very similar, the differences in the interaction strength seem to be primarily correlated with the geometry of the template in the different phases. Assuming that the TDI molecules are preferentially aligned with their long axis along the hydrophobic tails of the surfactant molecules and assuming a rather straight geometry of these tails, the observed orientational dynamics can be understood according to the schemes depicted in Figure 8.5. According to these assumptions, the TDI molecules constantly rotate while diffusing in hexagonal channels (Figure 8.5 c). In contrast, there is no rotational motion when TDI is accommodated in the template phase between flat silica sheets. Alignment along the hydrophobic tails of the surfactant molecules in this case implies a fixed orientation perpendicular to the lamellae (Figure 8.5 d). This model might also explain the different diffusion rates in both phases. Molecules that constantly reorient might diffuse more easily than those that are forced into a fixed orientation.

The doughnut shaped pattern diffuse randomly in two dimensions, as would be expected for molecules trapped in the surfactant layer between the silica planes (see trajectory in Figure 8.5 b). In contrast, molecules in the hexagonal phase travel in a highly structured manner. A detailed picture of an individual trajectory in the hexagonal phase is shown in Figure 8.5 a. It is obvious that the molecule enters several domains with different orientations illustrating the connectivity of the pore system at the domain-domain interfaces. The molecule travels first along the C-shaped structure on the right (1). It bounces back from the domain boundaries several times moving back and forth in that single domain. After 65 s it discovers a side-arm (2) and diffuses back and forth the C-shaped structure and side-arm. 100 s later, it finds its way to the linear structure at the bottom (3), diffusing back and forth including the horizontal streak from the C-shaped domain. After another 144 s it enters another domain (4) where it is trapped moving from one end to the other for 69 s until it comes back to the linear region at the bottom. From there it enters region 5 where it moves back and forth for 109 s until the end of the film. Thus, some domains are connected in a way that the domain boundaries are easily overcome by the dye molecules (regions 1-3), while other domains are harder to access and harder to leave; possibly they are only accessible through defects (regions 4, 5).
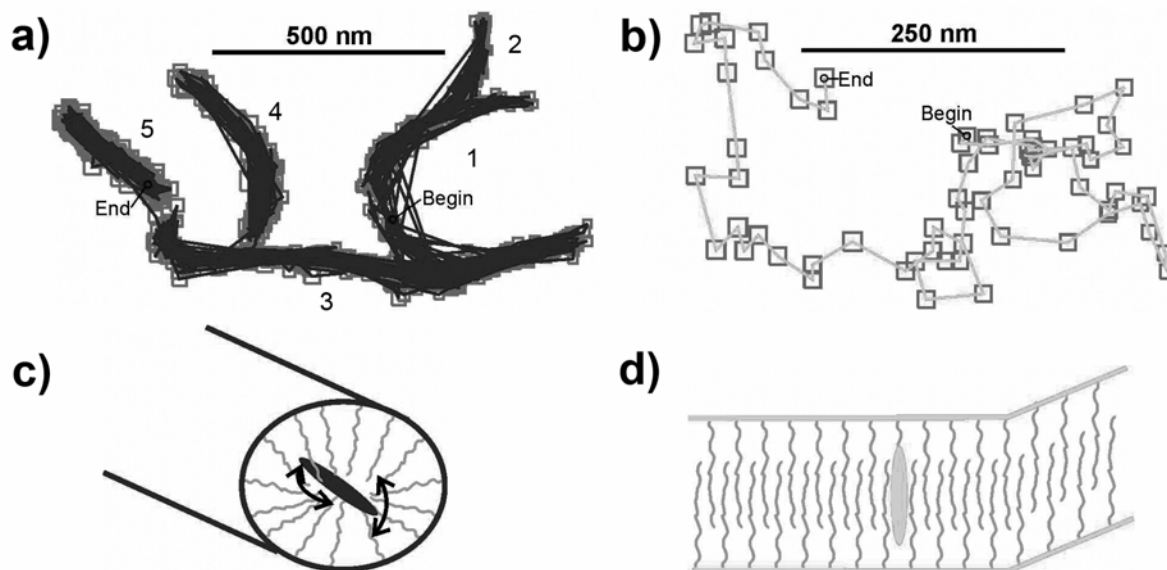
Figure 8.5*: Trajectories of two molecules diffusing in the pure hexagonal [a)] and pure lamellar [b)] phase, respectively. The trajectory of the fast diffusing molecule in the hexagonal phase shows a pronounced structure which reflects the structure of the hexagonal channels, whereas the trajectory of a doughnut shaped pattern in the pure lamellar phase shows random walk behaviour. A schematic view of the arrangement of the guest molecules inside the hexagonal and lamellar topologies is depicted in [c)] and [d)].

This is one of the many examples which show how a single molecule explores the structure of the host. The trajectory of the molecule directly maps the alignment of the channels and the domain structure. In addition, the real time observation of the molecule allows us to visualize the accessibility of the channels and the connectivity of the domains in an unprecedented way.

In the fluorescence microscopy image of a sample exhibiting a mixture of hexagonal and lamellar structure (surfactant : silica ratio of 0.13, Figure 8.4 c), Gaussian-shaped and doughnut patterns coexist within the same region. Single particle tracking results in the 117 trajectories depicted in Figure 8.6. The doughnut shaped pattern of dye molecules diffusing inside the lamellar structure are visible in Figure 8.4 c, but are not tracked in Figure 8.6, since they exhibit too little intensity during the respective measurement time for each single image. On a timescale of minutes to hours, however, these molecules show unstructured diffusion in two dimensions. Besides the doughnut shaped patterns, three different populations of Gaussian patterns can be distinguished. The first type comprises diffusion along distinct

structures over a large range of one to five microns typical for molecules diffusing in the hexagonal phase (109 blue tracks shown in Figure 8.6). Another, much smaller population consists of molecules that diffuse much faster, without showing a particular structure in their trajectories (five examples shown in red in Figure 8.6). These fast moving molecules with unstructured trajectories could be removed by washing the surface of the sample with water, clearly indicating that the molecules were on the surface of the film. Finally, very few molecules were observed that are immobile within the positioning accuracy (two examples marked in square boxes in Figure 8.6). They may be either captured in very small cavities inside the material or strongly adsorbed on the surface of the pore walls.
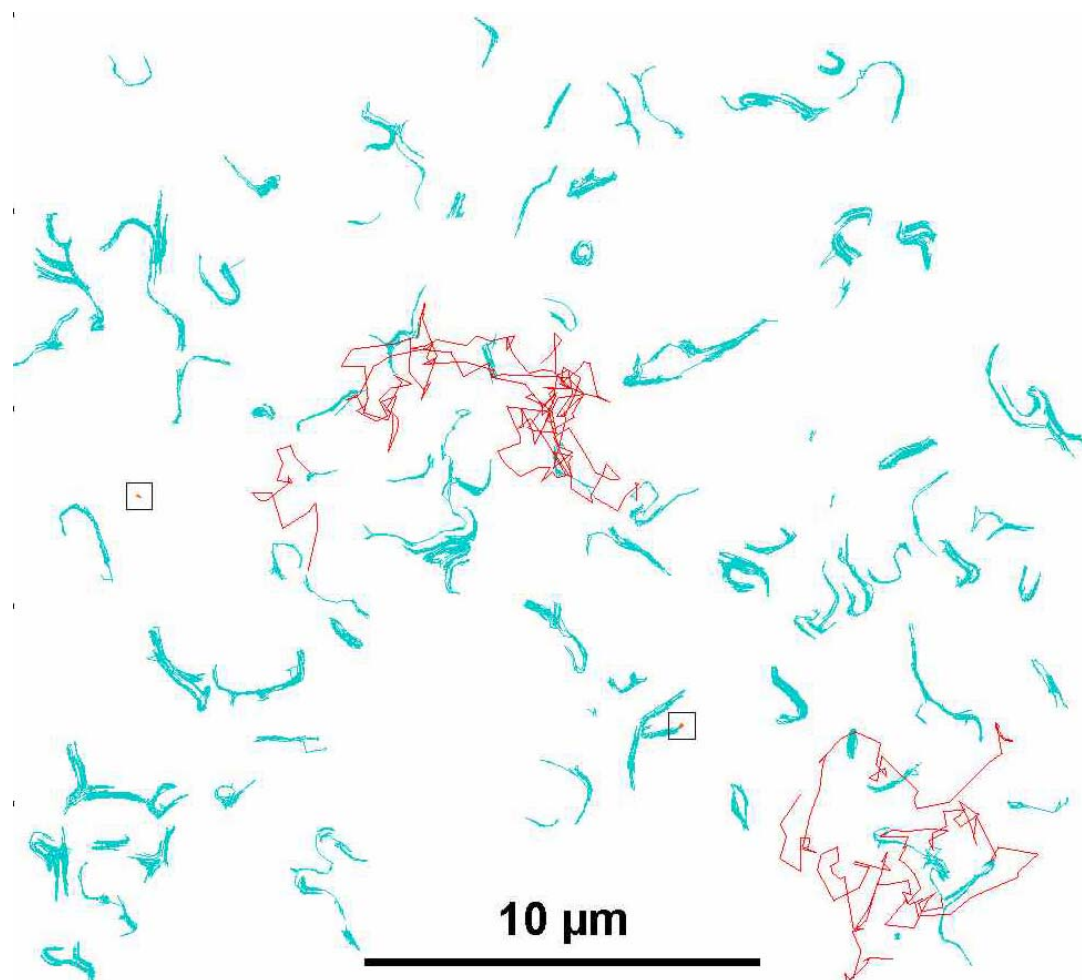
Figure 8.6*: Trajectories of the diffusion obtained by single particle tracking of dye molecules in a sample synthesized with surfactant **:** silica ratio of 0.13 (hexagonal / lamellar phase mixture). Molecules with doughnut shaped patterns corresponding to molecules diffusing within the lamellar phase are not tracked since the intensity of their pattern was too low on the chosen time scale. Molecules showing structured diffusion in the hexagonal phase are plotted in blue; molecules showing fast and unstructured diffusion on the sample surface are plotted in red. Immobile molecules are marked in squared boxes.

In some cases multiple changes between doughnut shaped and mobile Gaussian-shaped patterns (red and blue tracks) were observed. These observations clearly demonstrate that the two different phases are actually interconnected, probably via structural defects at the phase boundaries. Interestingly, we also observed other cases where the molecule switches several times from a Gaussian to a doughnut pattern at exactly the same position, showing that molecules sometimes find their way back through the same defect region. Moreover, the molecules can enter the surface and find their way back to the pore system of the silica film. Thus, it is possible to correlate the different diffusion behavior with the structural information. A schematic general picture of the different phases present in the film and the migration within as well as between the phases is shown in Figure 8.7.
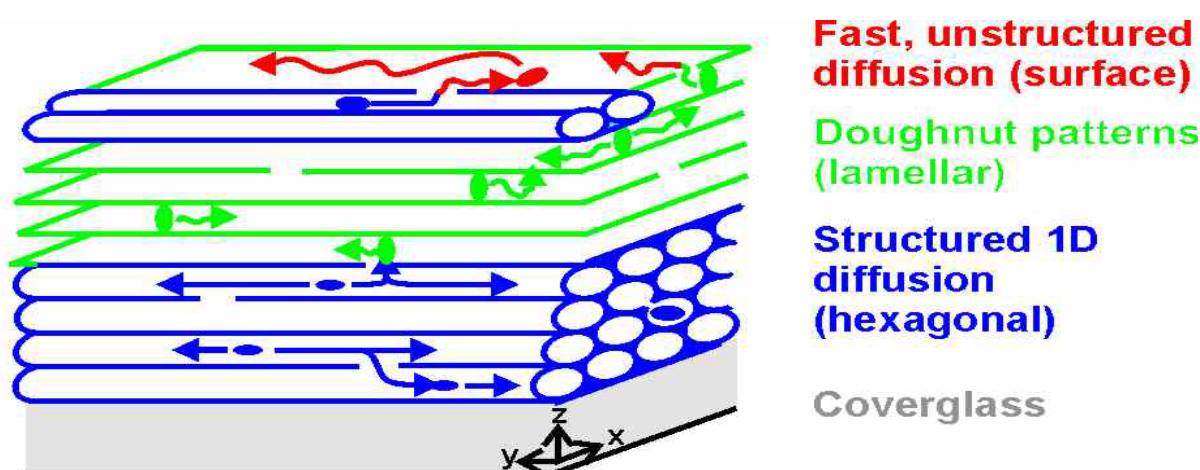
Figure 8.7*: Sketch of the diverse diffusion modes. Molecules diffusing randomly in the lamellar phase are oriented perpendicular to the surface (green). Structured diffusion over long distances and constant reorientation of the molecules takes place in the hexagonal phase (blue). Molecules on the surface show fast, unstructured diffusion. Transitions between the different diffusion modes are explained by connections between the pore topologies.

It was found that the diffusion coefficients do not only vary between the different phases, but can also change within the same trajectory of an individual molecule. A detailed analysis of these data can elucidate possible differences in the diffusion behavior being spatially correlated with differences of the environment from domain to domain. Evaluation of the diffusion data was carried out for molecules diffusing exclusively in the hexagonal phase by plotting the cumulative probability of the squared displacements for different time

intervals.[12,33] Diffusion coefficients between 2×10^{-4} and 1×10^{-1} μm^2 s^{-1} were calculated for structured diffusion within hexagonally ordered mesopores. It was found that diffusion regimes with different diffusion coefficients can sometimes be spatially correlated to different domains. However, there are also cases where changes in the diffusivity cannot be correlated with spatial areas in the trajectory.

In one special case, a sample prepared with a surfactant : silica ratio of 0.08 (pure hexagonal phase) showed little diffusion but many immobile molecules in fluorescence microscopy. Another sample prepared with the same recipe showed the usually observed small amount of immobile molecules and mainly structured diffusion. The X-ray diffraction patterns of both samples look similar. Corresponding TEM images of the respective samples are shown in Figure 8.8 a and 8.8 b. The mesostructured film was scratched off the substrate using a razor blade; the resulting mesophase powder was transferred onto a copper grid for TE microscopy.
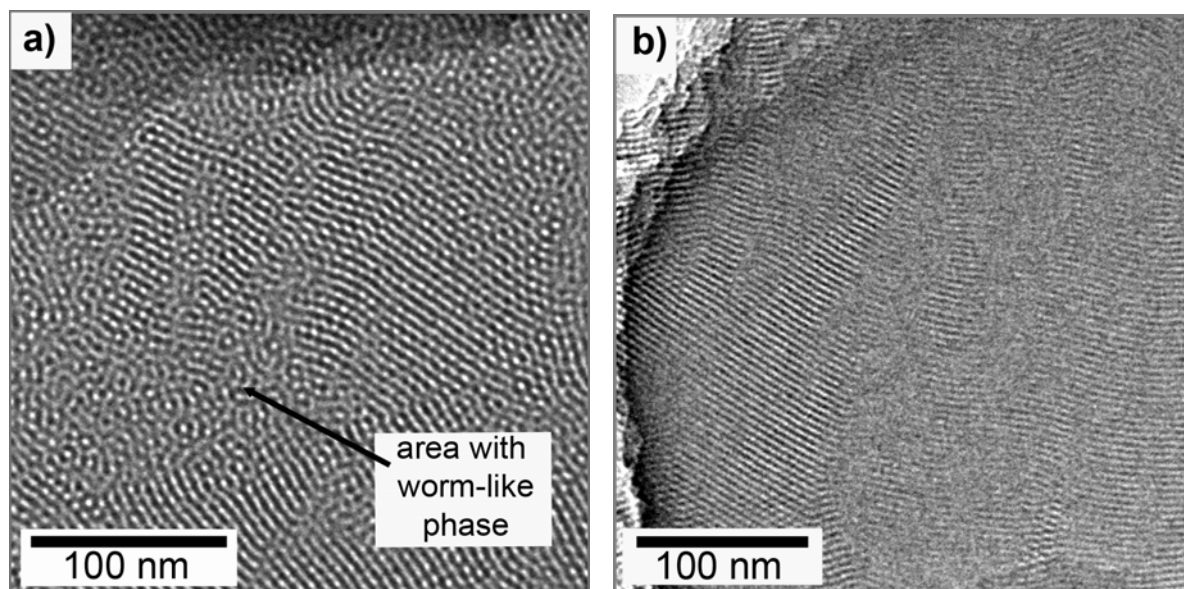
Figure 8.8: TEM images of samples prepared with a surfactant : silica ratio of 0.08, showing many immobile molecules [corresponding TEM image in a)] or regular diffusion [corresponding TEM image in b)]. The TEM images reveal many areas with retarded hexagonal or worm-like structure in the sample showing unusual high fraction of immobile molecules.

The film with a large number of immobile molecules shows many areas with a worm-like structure (Figure 8.8 a).[34] This phase can be understood as having regular d-spacing but rods

too short to arrange in a hexagonal way and show random orientation in all directions. Thus, the structure results in an intensity distribution of spherical symmetry in reciprocal space and cannot be distinguished from a hexagonal phase by 1D diffraction. Obviously, the pores are not highly interconnected in the worm-like structure, as indicated by the many immobile molecules observed in this sample. The TEM image of the other film showing typical diffusion in a structured manner (Figure 8.8 b) reveals the hexagonal arrangement of pores that is usually observed for samples with a surfactant : silica ratio of 0.08.

8.2. CTAB thin films

Thin silica films with 2D hexagonal structure containing CTAB as structure directing agent have been prepared in the same manner as the films synthesized with Brij 56 discussed above. The 2D hexagonal phase is verified by X-ray diffraction in a Bragg-Brentano geometry and TE microscopy (Figure 8.9 a, b). The representative TEM image in Figure 8.9 b shows two pieces of the mesostructured film that were scratched off the silica substrate. One piece shows the hexagonal stacking of the silica tubes; the other shows the typical line pattern of the tubes imaged in plan-view. TDI molecules were incorporated into the pores during the spin-coating process as described in the above Section 8.1 (dye concentration: 10^{-9} mol/l). The d-spacing of the CTAB films is about 3.8 nm in a sample four days old as well as in the same sample aged for several weeks in high humidity, according to the X-ray patterns depicted in Figure 8.9 a. This shows that both the structure and d-spacing is maintained during time. The first order peak is even sharper in the aged sample. Assuming a silica wall thickness of about 1 nm, the pore diameter is estimated to be about 3 nm. Therefore the 1 x 1 x 2.5 nm^3 sized dye molecules are already limited in their freedom to move and show much slower diffusion and reorientation than in structures synthesized with Brij 56.
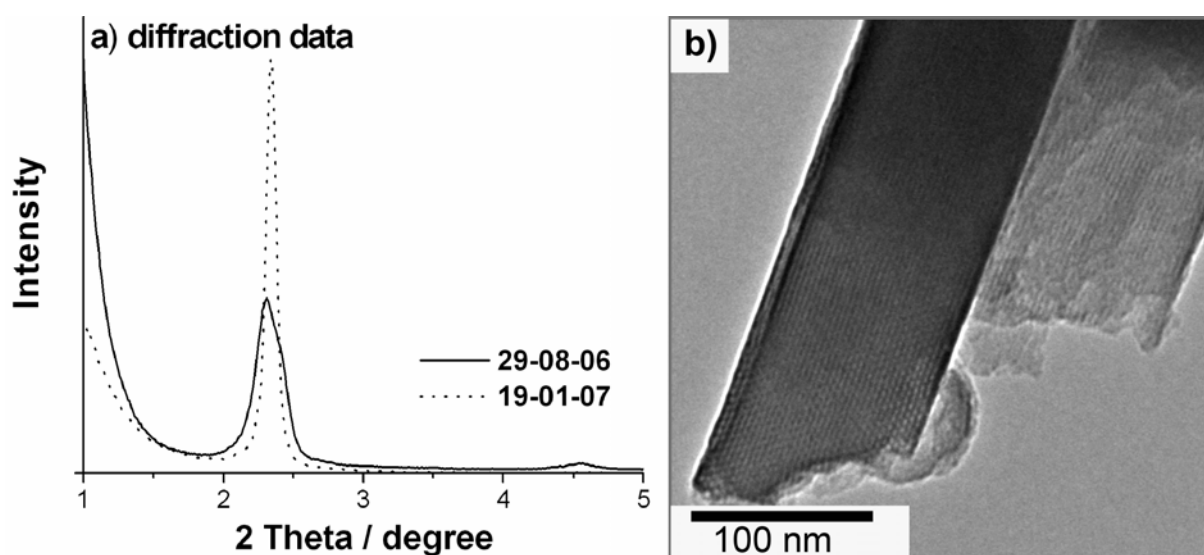
Figure 8.9: Diffraction patterns of a CTAB-templated silica sample exhibiting hexagonal structure, recorded 4 days and 131 days after synthesis, respectively [a)]. A corresponding TEM picture of two pieces of the mesophase film [b)] shows the hexagonal arrangement of the pore system (left piece) as well as the line-pattern of pores imaged in plan-view (right piece).

TDI molecules in CTAB-templated pores with hexagonal arrangement move with diffusion constants in the range of 2×10^{-10} μm^2 s^{-1}. In comparison, the 1D diffusion constants of molecules moving inside hexagonally ordered pores templated with Brij 56 are much higher, between 2×10^{-4} and 1×10^{-1} μm^2 s^{-1}. Furthermore, the diffusion rate in the CTAB system strongly depends on the atmosphere present during the diffusion measurements.[28] While the molecules do not diffuse at all when measured at low relative humidity, they successively diffuse faster when the humidity during the experiments increases (work is in progress).

TDI molecules trapped in the Brij 56 templated films constantly reorient on a timescale below 300 ms (see above, Section 8.1). In contrast, TDI molecules inside films synthesized with CTAB typically stay oriented for a couple of seconds up to hours, depending on the humidity during the measurements.[27,28] Dye molecules located in the same region and oriented with similar angles indicate mono-oriented mesopores building up one domain. The dye is assumed to align with the long axis along the pores of the mesostructured host. Thus, the orientation of the TDI reflects the orientation of the hexagonally stacked mesoporous silica providing

143

information about the domain orientation, shape and size that cannot be easily obtained by other methods.[28]

The experimental set-up for measuring the dye molecule orientation is based on a confocal laser scanning microscope. The dye molecules are exited by laser light which polarization is modulated using a rotating $\lambda/2$ retardation plate. The polarization is monitored in transmission. The fluorescent light coming from the dyes is separated from the excitation light and routed to another detector. The fluorescence intensity is modulated according to the polarization of the excitation light. The in-plane orientation angle can be evaluated from the phase shift of the modulated fluorescence intensity versus the modulated intensity of the excitation light.
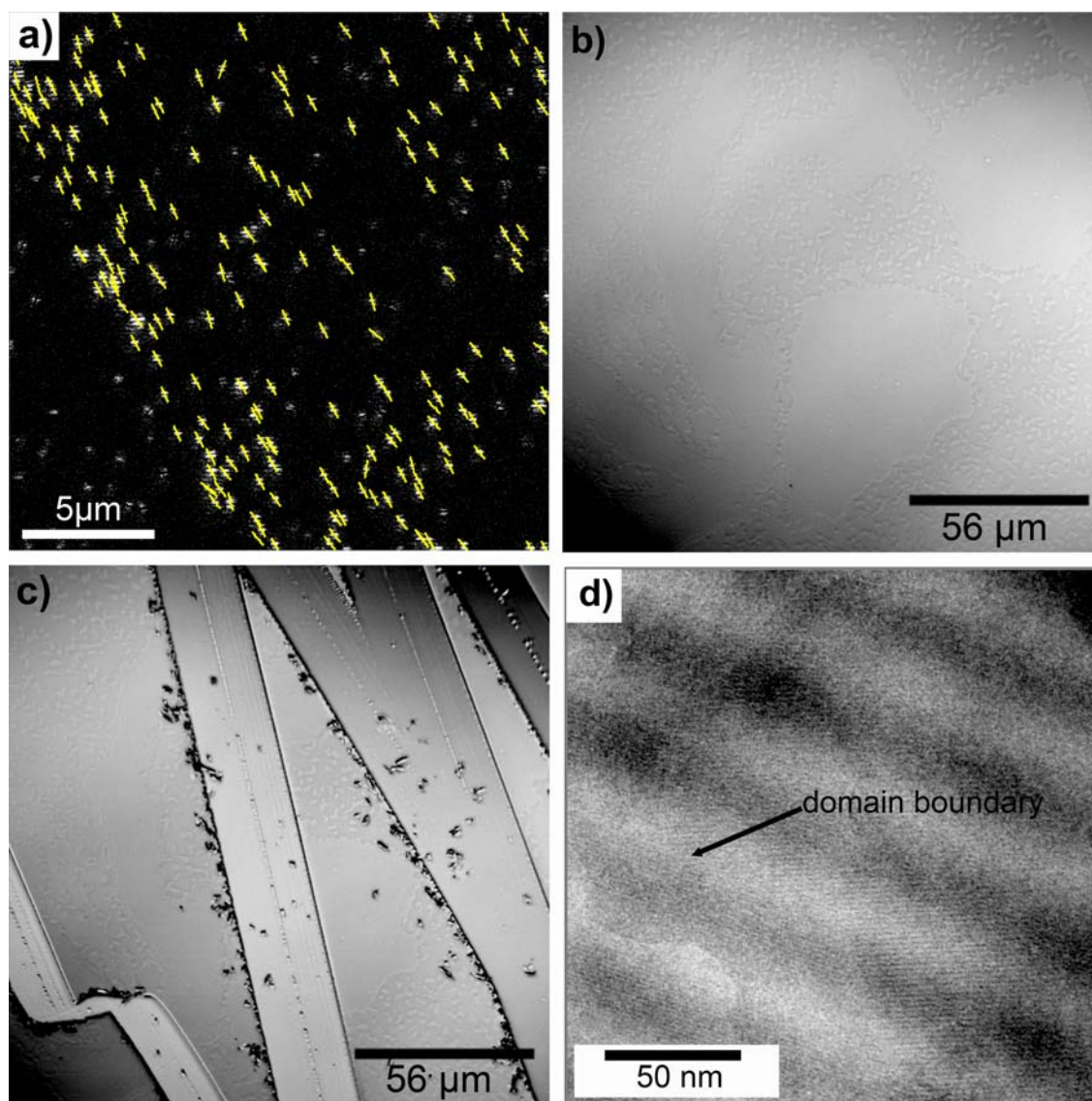
Figure 8.10 a-c*, d: Fluorescence microscopy image of oriented single dye molecules [a)]. The direction of the inserted lines corresponds to the orientation of the long molecule axis of TDI. Large domains appear as bright areas in confocal light microscopy image [b)]. The mesostructured film was scratched off the glass surface at the position of large domains [c)] and transferred to a TEM grid. Areas with highly ordered mesophase were imaged with TEM [d)].

Typical domains in as-prepared samples were found to be 1-2 μm long. When the samples were aged at high humidity for several weeks, large domains with linear orientation were observed to have formed. A fluorescence image from dye molecules oriented in the same direction is depicted in Figure 8.10 a. The Gaussian-shaped patterns of the fluorescent dye molecules are striped because of the polarized excitation light. The direction of orientation (long molecular axis) is indicated by the direction of the inserted lines. It is observed that all molecules are oriented in the same direction over an area of at least 15 x 15 μm. The linearly

oriented, large domains are correlated with the brighter areas visible when the samples are imaged with the conventional confocal light microscope set-up (Figure 8.10 b). It is assumed that this effect is due to different refractive indices of areas with comparatively small domains having different orientations and areas with linear mono-orientation of the silica mesophase over several microns. Domains 10-100 μm long were found to be evenly distributed and cover about 1/10 of the entire film surface (4 cm^2).

TEM imaging was performed on mesostructured powder scratched off a sample exhibiting large domains. The scratching was monitored by simultaneous imaging of the sample with a confocal light microscope in order to increase the amount of mesostructured material on the TEM grid derived from highly ordered, large domains. An image of the film after scratching is shown in Figure 8.10 c depicting the same area as imaged in Figure 8.10 b. A TEM picture of the sample is shown in Figure 8.10 d depicting high order and linear orientation of the mesopores. However, the areas recovered from scratching and appropriate for TEM imaging typically extend over less than one μm. Sample preparation by scratching is very invasive to the film (Figure 8.10c) and breaks it into TEM-transparent pieces too small to image the large domains. Big pieces that are not transparent in the electron beam were observed and might possibly be thoroughly ordered.

The Debye-Scherrer equation may be used in crystalline samples to calculate the size of the crystallites (corresponding to the domain size in film systems). However, mesophases cannot be compared with fully crystalline phases; the peaks may be as well broadened due to fluctuations of the d-spacing or due to superposition with the primary beam at small angles. Assuming that the broadness of the peaks originates solely from the domain size and applying the Debye-Scherrer equation on the X-ray pattern taken from the sample discussed above, the calculated minimum domain size is 200 nm for the comparatively sharp peak after ageing.

The microscopic observation of of a significant fraction of large domains suggests that the peaks are additionally broadened by other mechanisms and that the Debye-Scherrer equation is not applicable for this system.

The results from confocal fluorescence and light microscopy are striking, clearly demonstrating that as-prepared films show structural re-orientation and substantial growth of highly linear and large domains during several weeks after synthesis. This is a direct observation of the liquid-crystalline characteristics of EISA films.[11,35,36] Single molecule microscopy is a powerful method for imaging these processes in real time and *in situ*. Defining optimum conditions needed for domain growth is subject of further investigations.

8.3. Composite membranes

Initial diffusion measurements were also performed on mesostructured silica fibers prepared inside the channels of anodic alumina membranes. The advantage of these materials is that the orientation of the mesopores with respect to the membrane surface is known from conventional characterization methods. Therefore the composite membranes can be used as model system for the investigation of the orientational dynamics and diffusion of molecules *via* fluorescence microscopy. The following approach is derived from the measuring principle of thin films, transferring the silica fibers onto a previously cleaned glass slide. The high aspect ratio of the fibers enables us to determine the orientation of the silica rods making up the mesostructure even when they are extracted from the alumina matrix.

Dissolution of the alumina matrix and spin-coating of the silica fibers on a substrate works in principle but may extract a fraction of the dye molecules.[37] Hence, a dry preparation method was developed. First, the composite membrane was broken into pieces and a razor blade was moved along their edges causing the silica fibers to fall down onto a glass substrate. The

corresponding SEM image is depicted in Figure 8.11 a showing that pieces of the alumina/silica composite have been scratched off the membrane edges instead of exclusively the silica fibers. In a second approach, the edges of the broken composite membrane were tapped on a sticky surface. The pressure-sensitive adhesive Acronal® A220 was kindly donated from BASF and spin-coated onto conventionally cleaned glass cover slips. A corresponding SEM image depicted in Figure 8.11 b shows that silica mesostructures are successfully extracted from the AAM matrix and possible coiling of the fibers was prevented.

Fluorescence microscopy images were taken from such prepared samples using on the one hand high dye molecule concentrations and a confocal set-up, and on the other hand using single molecule concentrations of TDI and a wide-field microscope. A representative image from the ensemble measurement is shown in Figure 8.11c. The fluorescent stripe derives from the imprint of a membrane edge after it was tapped onto the adhesive surface. The stripe is about 30 μm thick and obviously contains many fluorescent dye-loaded single mesostructured fibers. The composite membrane was synthesized using ionic CTAB as surfactant thus giving silica fibers with columnar hexagonal pore-orientation (see Chapter III, Section 2.1). Similar to what is observed in thin films, the TDI molecules are oriented within the mesopore-channels and give a line-pattern during scanning of the image when exited with light of periodically modulated polarization. The line-pattern of the dye-loaded silica fiber ensembles indicates that the orientation of the fibers is predominantly maintained even in the imprint of the membrane edge.

Single molecule fluorescence spectroscopy with sufficient signal-to-noise ratio at the wide-field microscope is more difficult, presumably due to the presence of fluorescent impurities in the composite membrane sample and index-matching issues in the region of the membrane

imprint. A representative image in Figure 8.11 d shows single TDI molecules as bright spots at the position of a membrane imprint.
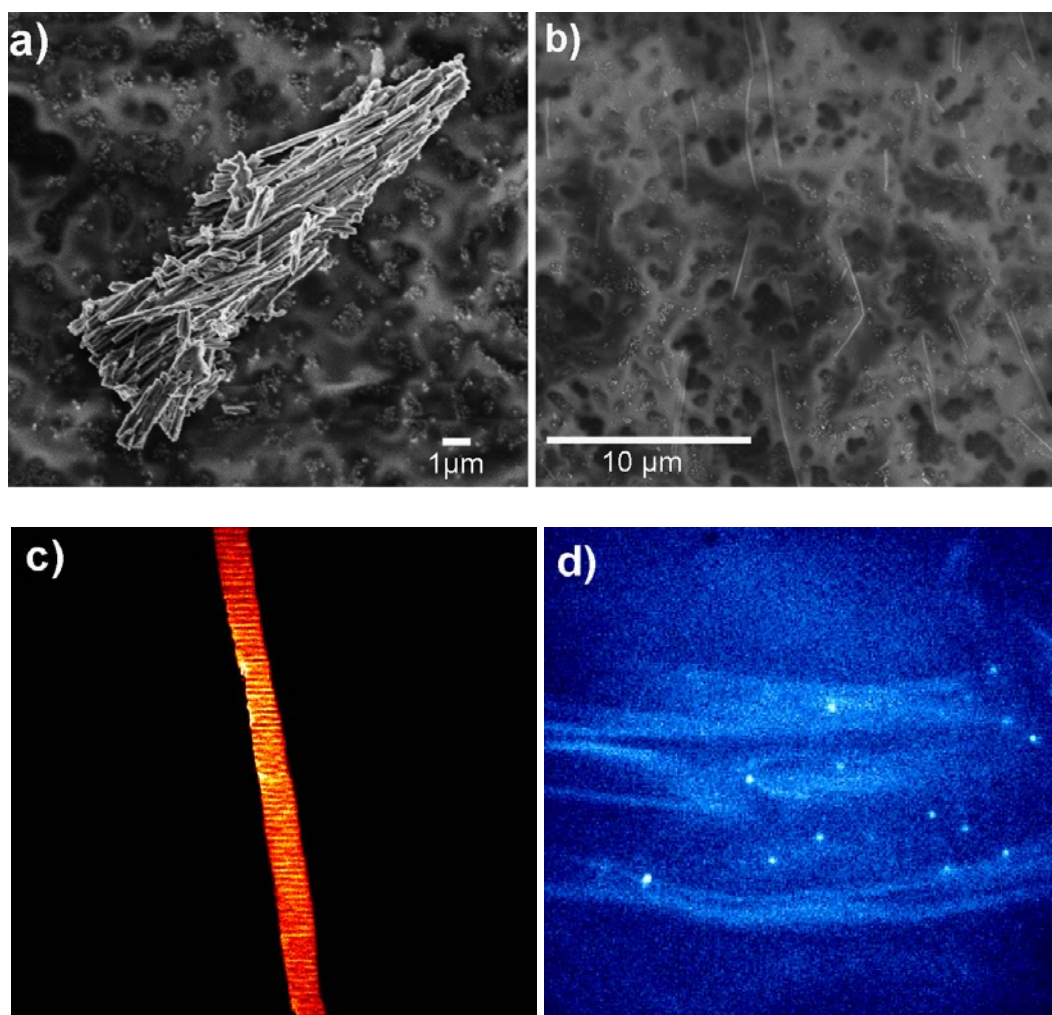
Figure 8.11a, b, c*: SEM image of a piece of a composite membrane scratched off with a razor blade [a)]. Single mesophase silica fibers are extracted when the composite membrane edge is tapped onto a sticky surface [b)].
c) A fluorescence microscope image of one imprint of the edge of a composite membrane (ensemble concentration of dye).The line-pattern derives from oriented TDI-molecules.
d) Wide-Field fluorescence microscopy image of another imprint from a composite membrane doped with dye in single-molecule concentration. The bright spots are single TDI molecules.

8.4. Sample preparation

The deposition mixtures were prepared applying a two step procedure: First, 2.08 g (0.01 mol) tetraethyl orthosilicate (TEOS, Aldrich) was mixed with 3 g 0.2 M HCl, 1.8 g H$_2$O and 7.9 g ethanol and heated at 60 $^{\circ}$C for 1h to accomplish acid-catalyzed hydrolysis-condensation of the silica precursor. For preparation of the Brij 56 templated films this solution was mixed with a second solution containing 225 mg (0.3 mmol), 435 mg (0.7 mmol), 566 mg (0.8

mmol), 680 mg (1.0 mmol), 906 mg (1.3 mmol), 1360 mg (2.0 mmol), 1810 mg (2,7 mmol), 2245 mg (3.3 mmol), 2716 mg (4.0 mmol), or 4980 mg (7.15 mmol) Brij 56 dissolved in 3.12 g, 6.25 g, 7.8 g, 9.38 g, 12.5 g, 18.75 g, 25.0 g, 31.25 g, 37.5 g, or 68.75 g ethanol, respectively. For preparation of the CTAB templated films 730 mg (2 mmol) CTAB dissolved in 15.8 g ethanol were added to the TEOS containing solution. Finally, 6 µl of 10^{-8} molar solution of TDI in ethanol was added to 1 ml of the synthetic mixtures. The samples were prepared by spin-coating the precursor solutions on previously cleaned glass slides (see section 2.1.).

For preparation of the AAM composite material, 2.08 g (0.01 mol) tetraethyl orthosilicate (TEOS, Aldrich) was mixed with 3 g 0.2 M HCl, 1.8 g H_2O and 3.98 g EtOH and heated at 60 $^{\circ}$C for 1h and cooled to room temperature. A second solution containing 0.947 g (2.6 mmol) CTAB in 7.9 g ethanol was subsequently added. 1 ml of the precursor solution was mixed with 20 µl of 10^{-6} molar or 20 µl of 10^{-8} molar solutions of TDI in ethanol, respectively, and evenly spread on an AAM and left to dry. After reaching complete dryness, the membranes were broken into pieces. Acronal$^{\circledR}$ A 220 was spin-coated on previously cleaned cover slips for 15 seconds at 4000 rounds per minute. The composite pieces were tapped onto the sticky cover slip surface to leave imprints containing the extracted mesostructured silica fibers.

References

[1]   G. E. Thompson, *Thin Solid Films* **1997**, *297*, 192-201.

[2]   T. Iijima, S. Kato, R. Ikeda, S. Ohki, G. Kido, M. Tansho, T. Shimizu, *Chem. Lett.* **2005**, *34(9)*, 1286.

[3]   G. E. Thompson, G. C. Wood, *Nature* **1981**, *209*, 230.

[4]   S. Soled, *J. Cat.* **1983**, *81*, 252.

[5]   H. Shiraki, Y. Kimura, H. Ishii, S. Ono, K. Itaya, M. Niwano, *Appl. Surf. Sci.* **2004**, *237*, 369.

[6]   K. Ha, H.-J. Ahn, *Liquid Crystals* **2004**, *31(11)*, 1525.

[7]   S. Rana, S. Ram, *J. Solid State Chem.* **2001**, *157*, 40.

[8]   A. Monnier et al., *Science* **1993**, *261*, 1299.

[9]   A. Yamaguchi, F. Uejo, T. Yoda, T. Uchida, Y. Tanamura, T. Yamashita, N. Teramae, *Nature Mater.* **2004**, *3*, 337.

[10]   D. Grosso, F. Cagnol, G. J. de A. A. Soler-Illia, E. L. Crepaldi, H. Amenitsch, A. Brunet-Bruneau, A. Bourgeois, C. Sanchez, *Adv. Funct. Mater.* **2004**, *14*, 309.

[11]   F. Cagnol, D. Grosso, G. J. de A. A. Soler-Illia, E. L. Crepaldi, F. Babonneau, H. Amenitsch, C. Sanchez, *J. Mater. Chem.* **2003**, *13*, 61.

[12]   J. Kirstein, B. Platschek, C. Jung, R. Brown, T. Bein, C. Bräuchle, *Nature Mater.* **2007**, *6*, 303.

[13]   B. Platschek, N. Petkov, T. Bein, *Angew. Chem Int. Ed.* **2006**, *45*, 1134-1138.

[14]   Y. Wu, G. Cheng, K. Katsov, S. W. Sides, J. Wang, J. Tang, G. H. Fredrickson, M. Moskovits, G. D. Stucky, *Nature Mater.* **2004**, *3*, 816.

[15]   C. Yu, B. Tian, J. Fan, G. D. Stucky, D. Zhao, *J. Am. Chem. Soc.* **2002**, *124*, 4556-4557.

[16]   J. L. Ruggels, S. A. Holt, P. A. Reynolds, J. W. White, *Langmuir* **2000**, *16*, 4613.

[17]   W. Tjandra, J. Yao, K. C. Tam, *Langmuir* **2006**, *22*, 1493.

[18]   C. Li, Y. Wang, Y. Guo, X. Li, Y. Guo, Z. Zhang, Y. Wang, G. Lu, *Chem. Mater.* **2007**, *19*, 173.

[19]   S. A. Bagshaw, *Chem. Commun.* **1999**, 1785.

[20]   C. Yu, J. Fan, B. Tian, D. Zhao, *Chem. Mater.* **2004**, *16*, 889.

[21]   Y. Wang, Y. Wang, C.-M. Yang, G. Lu, F. Schüth, *Langmuir* **2006**, *22*, 5491.

[22]   E. Leontidis, *Curr. Opin. Colloid Interface Sci.* **2002**, *7*, 81.

[23]   B. Smarsly, A. Gibaud, W. Ruland, D. Sturmayr, C. J. Brinker, *Langmuir* **2005**, *21*, 3858.

[24]   J.-h. Ma, C. Guo, Y.-l. Tang, J. Wang, L. Zheng, X.-f. Liang, S. Chen, H.-z. Liu, *Langmuir* **2007**.

[25]   R. C. Hayward, P. C. A. Alberius, E. J. Kramer, B. F. Chmelka, *Langmuir* **2004**, *20*, 5998-6004.

[26]   J. Y. Cheng, A. M. Mayes, C. A. Ross, *Nature Mat.* **2004**, *3*, 823.

[27]   C. Jung, C. Hellriegel, B. Platschek, T. Bein, C. Bräuchle, *J. Am. Chem. Soc.* **2007**, accepted.

[28]   C. Jung et al., in preparation.

[29]   A. Zürner et al., in preparation.

[30]   C. Jung et al., *J. Am. Chem. Soc.* **2006**, *128*, 5283.

[31]   D. Zhao, Q. Huo, J. Feng, B. F. Chmelka, G. D. Stucky, *J. Am. Chem. Soc.* **1998**, *120*, 6024.

[32]   R. M. Dickson, D. J. Norris, W. E. Moerner, *Phys. Rev. Lett.* **1998,** *81*, 5322.

[33]   M. J. Saxton, K. Jacobson, *Annu. Rev. Biophys. Biomol. Struct.* **1997**, *26*, 373.

[34]   Pinnavaia et al., *Science* **1995**, *267*, 865-867.

[35]   C. J. Brinker, Y. Lu, A. Sellinger, H. Fan, *Adv. Mater.* **1999**, *11(7)*, 579.

[36]   G. J. deA. A. Soler-Illia, E. L. Crepaldi, D. Grosso, C. Sanchez, *J. Mater. Chem.* **2004**, *14*, 1879.

[37]   N. K. Mal, M. Fujiwara, Y. Tanaka, *Nature* **2003**, *421*, 350.

[37]   N. K. Mal, M. Fujiwara, Y. Tanaka, *Nature* **2003**, *421*, 350.

IV. Conclusion

1. Synthesis of mesostructured silica inside anodic alumina channels

Mesostructured silica material was synthesized in the confined environment of the channels of porous anodic alumina membranes. The composite membranes were investigated by transmission electron microscopy and two-dimensional small angle X-ray scattering. A sample holder was developed for this purpose, thus enabling measurements parallel to the composite membrane surface. Through the combination of 2D SAXS and TEM, semi-quantitative information about the distribution between the phases could be obtained in phase mixtures. Thus, the influence of various changes in the synthesis conditions on the formation of the silica mesostructures within AAM channels could be studied. Additionally, *in situ* small angle X-ray scattering experiments were performed in grazing incidence geometry to gain insights into the mechanisms of structure formation under spatial confinement.

When ionic surfactant CTAB was used in the synthesis as structure directing agent, the hexagonally structured mesopores were solely oriented along the AAM-channels. In case of using the non-ionic surfactants P123 or Brij 56, the formation of hexagonal phases with two different pore-orientations (circular and/or columnar) and the formation of a circular lamellar phase were observed, depending on the synthesis conditions. Characterization of the lamellar phase from diffraction data alone is difficult since the reflections occur at the same position as the ones for the columnar hexagonal structure. The resolution in the SAXS set-up is not high enough to distinguish the two very close maxima. Therefore, transmission electron microscopy is additionally needed to identify the formation of the lamellar phase.

With non-ionic surfactants, the structure was directed towards the formation of higher fractions of the columnar orientation when the surfactant:Si ratio was subsequently increased. Before a pure columnar phase was produced, formation of the tubular lamellar structure was

observed. High humidity during the EISA-process was found to direct the structure towards the formation of higher fractions of columnar phase.

The *in situ* grazing incidence X-ray scattering study demonstrated that when ionic CTAB was used as surfactant, the columnar hexagonal structure was formed directly from the beginning of the synthesis. In samples synthesized with the non-ionic surfactants Brij 56 and P123, the circular hexagonal structure was found to form first and then to subsequently transform directly into the columnar hexagonal, or into a mixture of columnar hexagonal and the circular lamellar phase. The existence of the circular lamellar phase could be, for the first time, directly proven by GISAXS.

In a second part of the *in situ* GISAXS study, the influence of the humidity on the structure formation was investigated. The non-ionic structure directing agents Brij 56 and P123 were used with different surfactant **:** silica ratios and samples were prepared at various relative humidities. The formation of hexagonal phases with circular or columnar orientation was observed for lower surfactant concentrations. A tubular lamellar structure was additionally formed at higher surfactant **:** silica ratios. Phase formation takes place after almost complete solvent evaporation; subsequent phase transformations occur only after the completion of the EISA process. The circular hexagonal phase appears to represent the kinetically favored phase, always being observed to form first and occasionally transforming into more stable phases.

TEM images of the samples reveal the pronounced effect of spatial confinement on the growth and location of the different phases. The columnar phase in Brij 56-synthesized samples is preferably formed in the center of the mesoporous fibers. In contrast, the tubular lamellar structure is observed to form preferably at the AAM channel walls. Furthermore,

TEM cross-section experiments show various domain-domain interfaces occurring at random positions at different membrane heights. Thus, no indication was found for solvent gradient-induced structure formation and phase transformation. Based on these observations, a mechanism is proposed invoking random nucleation of a circular hexagonal mesophase followed by further phase transformations in the confined environment of the AAM channels. The insights gained in this study are anticipated to assist in the controlled design of nanoscale channel structures and host-guest systems.

In another study it was demonstrated that mesostructures with columnar instead of circular orientation can be formed with non-ionic surfactants as structure directing agents upon increasing the ionic strength of the respective precursor solutions by addition of inorganic salt ('Salt-induced phase transformation', SIPT). The formation of an amorphous silica layer at the alumina channel surface indicates that the strength of the chemical interactions at the interface to the AAM surface is increased upon the addition of inorganic salt. It is noted that no mesophase was formed anymore with either of the different precursor solutions inside the channels of an AAM that was hydrophobized by surface modification. We show that small cations lead to a more pronounced formation of the columnar phase and large anions can lead to phase distortion. The temperature during the EISA process plays a key role for SIPT. Synthesis of desired columnar mesostructures in confined space was achieved by salt addition and temperature control leading to salt-induced phase transformations.

The hexagonal structures were found to be stable upon calcination at 400 °C exhibiting mesoporosity with high specific surface area. Calcined samples showed a bimodal pore size distribution; smaller pore diameters correspond to the circular, bigger pore diameters reflect the presence of a columnar phase. In samples with phase mixtures, the quantitative

distribution between the phases shown by the sorption data is analogous to the trends derived from the diffraction patterns of the samples.

2. Exploration of mesostructured channel systems by fluorescent dye molecules

In a collaborative project single dye molecules were used as nanoscale probes to map out the structure of mesoporous silica channel systems that are prepared as thin films *via* cooperative self-assembly of surfactant molecules with polymerizable silicate species. The dye molecules act as beacons while they diffuse through different structural phases of the host. Based upon the structure of the trajectories, the diffusivities and the orientation of the molecules, it is possible to distinguish dyes travelling on the external surface from those travelling inside the pore system, dyes that diffuse along horizontal channels of the hexagonal phase, and those that move much more slowly in lamellar galleries of the mesoporous material. It is even possible to observe the same single molecule migrating between one type of surrounding, e.g., hexagonal channel system, and another such as the lamellar phase. In addition, the structural heterogeneity of the channels is reflected by the complex mode of motion observed for a single molecule within the hexagonal phase. The pore diameter of the respective host system directly influences the diffusion of dye molecules. In comparatively small channels systems the diffusion was found to strongly depend on the ambient conditions. At low relative humidity the molecules were immobile; diffusion could be switched on and off by controlling the atmosphere during the measurements. When samples were stored at high humidity, domain growth was observed resulting in mono-oriented domains up to 100 µm long. Thus, the data obtained by single molecule fluorescence microscopy provide direct information about the topology, the connectivity and accessibility of the channels and the structural domains making up the porous sample.

V. Appendix

List of Abbreviations

AAM	anodic alumina membranes
AlO(OH)	aluminum oxide / hydroxide
Brij56	decaethylene glycol hexadecyl ether
CCD	charge-coupled device
CMC	critical micelle concentration
CTAB	cetyltrimethylammonium bromide
CTAC	cetyltrimethylammonium chloride
DNA	deoxyribonucleic acid
DSC	differential scanning calorimetry
e.g.	exempli gratia
EISA	evaporation-induced self-assembly
GISAXS	grazing-incidence small-angle X-Ray scattering
ip-reflections	in-plane reflections: reflections in the horizontal plane of the primary beam (q_x-direction, see Chapter II, Figure 6), e.g. 01_r-reflections according to indexation in Chapter II, Figure 6
IUPAC	International Union of Pure and Applied Chemistry
LMU	Ludwig-Maximilians-Universität
MCM-41	Mobile Catalytic Material-41
MSS	modulable steady state
NMR	nuclear magnetic resonance
OH-group	hydroxyl-group
oop-reflections	out-of-plane reflections: reflections out of the horizontal plane of the primary beam, e.g. 10_r-reflection of the circular hexagonal phase according to indexation in Chapter II, Figure 6

Pluronic P123	poly(ethylene oxide)$_{100}$-b-poly(propylene oxide)$_{65}$-b-poly (ethylene oxide)$_{100}$
SAXS	small-angle X-Ray scattering
SBA-15	Santa Barbara Acidic-15
SDA	structure directing agent
SIPT	salt-induced phase transformation
SPT	single particle tracking
surfactant	surface active agent
TEM	transmission electron microscopy
TEOS	tetraethoxy-silane
TGA	thermogravimetric analysis
TMSCl	trimethylchlorosilane
XRD	X-Ray diffraction

Curriculum Vitae   **Dipl. chem. Barbara Platschek**

Zur Person

Name:	Platschek geb. Fieres
Vorname:	Barbara
Geburtstag:	01.06.1978
Geburtsort:	Fulda

Ausbildung

07.2007 / 11.2003	Promotion an der LMU, München im Arbeitskreis Professor Bein im Rahmen des Sonderforschungsbereichs 486 (Teilprojekte B1 und B8) Ordered Mesoporous Silica: Control of Morphology and Exploration with Single Molecules Kooperationen: Prof. J. D. Holmes, UCC, Cork, Ireland Prof. C. Bräuchle, LMU, München
03. 2003 / 11. 2003	Diplomarbeit an der LMU, München im Arbeitskreis Prof. Bein im Rahmen des Sonderforschungsbereichs 486 (Teilprojekt B8) Influence of an Electric Field to the Synthesis of Mesoporous Films
04. 2000 / 03. 2003	Chemiestudium an der LMU, München
04. 1998 / 04. 2000	Chemiestudium an der Philipps-Universität, Marburg
06. 1997 / 01. 1998	Auslandsaufenthalt in den USA im Rahmen einer Bildungsreise mit der gemeinnützigen Organisation „Up With People"
07. 1988 / 06. 1997	Engelsburggymnasium in Kassel

Barbara Platschek

München, 31.Mai 2007

Publications

G. Raschke et al. "Gold Nanaoshells improve Single Nanoparticle Molecular Sensors" *Nano Lett.* **2004**, *4(10)*, 1853-1857.

B. Platschek, N. Petkov, T. Bein, "Tuning the Structure and Orientation of Hexagonally Ordered Mesoporous Channels in Anodic Alumina Membrane Hosts: A 2D Small-Angle X-Ray Scattering Study" *Angew. Chem. Int. Ed.* **2006**, *45*, 1134-1138.

D. J. Cott, N. Petkov, M. A. Morris, B. Platschek, T. Bein, J. D. Holmes, "Preparation of Oriented Mesoporous Carbon Nano-Filaments within the Pores of Anodic Alumina Membranes" *J. Am. Chem. Soc.* **2006**, *128*, 3920-3921.

N. Petkov, B. Platschek, M. A. Morris J. D. Holmes, T. Bein, "Oriented Growth of Metal and Semiconductor Nanostructures within Aligned Mesoporous Channels" *Chem Mater.* **2007**, *19*, 1376-1381

J. Kirstein, B. Platschek, C. Jung, R. Brown, T. Bein, C. Bräuchle, "Exploration of Nanostructured Channel Systems with Single-Molecule Probes" *Nature Mater.* **2007**, *6*, 303.

C. Jung, C. Hellriegel, B. Platschek, D. Wöhrle, T. Bein, J. Michaelis, C. Bräuchle, "Simultaneous Measurement of Orientational and Spectral Dynamics of Single Molecules in Nanostructured Host-Guest Materials" *J. Am. Chem. Soc.* **2007**, *129*, 5570.

B. Platschek, R. Köhn, M. Döblinger, T. Bein, "In-situ GISAXS Study of the Formation of Mesostructured Phases within the Pores of Anodic Alumina Membranes", *Langmuir*, accepted.

B. Platschek, R. Köhn, M. Döblinger, T. Bein, "The Formation of Mesostructured Material in Confined Space – an In-situ GISAXS Study", in preparation.

B. Platschek, N. Petkov, D. Himsl, S. Zimdars, T. Bein, "Salt-Induced Phase-Transformation of Mesostructures Confined within Anodic Alumina Membrane Channels", in preparation.

Presentations

B. Platschek, N. Petkov, T. Bein, "Mesoporous Structures Within the Channels of Anodic Alumina Membranes", 18. Deutsche Zeolith-Tagung **2006**, Hannover, Deutschland

T. Bein, B. Platschek, N. Petkov, "Tuning Structure and Orientations of Hexagonally Ordered Mesoporous Channels in Anodic Alumina Membrane Hosts", American Chemical Society Spring Meeting and Exposition **2006**, Atlanta, USA

R. Köhn, B. Platschek, M. Döblinger, T. Bein, "Mesostructure Formation and Phase Transformation in Confined Space", 19. Deutsche Zeolith-Tagung **2007**, Leipzig, Deutschland